POLITECNICO DI TORINO

Master Degree in Mechanical Engineering

Master Degree Thesis

Design,Validation and Control of an Aeroelastic Two DOF System

Supervisor:
Prof. Elvio Bonisoli

Candidate:
Cristiano Martinelli

External Supervisor:
Prof. John Mottershead
Dr. Sebastiano Fichera

April 2019

The external supervisors are Prof. John Mottershead and Dr. Sebastiano Fichera from the Department of Mechanical, Materials and Aerospace Engineering of the University of Liverpool.

Summary

The thesis project was carried out entirely at the University of Liverpool having access to the wind tunnel to perform the experimental tests. The need of a new experimental model led to design a new one as first activity. Specifically, it has been re-designed a two-DOFs wing model with pitch and plunge motion and two active control surfaces: trailing- and leading-edge flap, respectively. The design has taken into account the need to adapt the wing model to the support structure and it has considered both the functional aspects of the wing and the static and dynamic technical specifications necessary for the correct functioning of the model. An analytical model with an unsteady definition of the aerodynamic loads was developed to obtain the prediction of the flutter velocity and to understand the internal dynamic behaviour of the model. In addition, a series of experimental tests were carried out to identify experimentally the aeroelastic system, such as: the study of the different flutter-speeds based on the configuration of the springs and masses of the support structure, the study of frequency response functions through the actuation of the shaker with and without wind and with the actuation of active control surfaces with wind. The updating of the analytical model was performed in order to validate the model both for the computation of the flutter-speed and for the identification of the system dynamics. The active controller was studied analytically and experimentally in a separate way. It consists of a proportional derivative integrative low-level controller and a proportional derivative high-level controller. From the analytical point of view, it has been developed a control with the quasi-steady definition of the aerodynamic loads while, from the experimental point of view the gains of the PID controller were chosen and the efficiency of the experimental control system was tested. Finally, pole placement was carried out through the numerical and experimental implementation of the receptance method.

Acknowledgements

First of all I would like to thank Prof. Bonisoli who allowed me to live this wonderful experience abroad and who supported me throughout the development of the thesis. A sincere thanks goes to the my team of the University of Liverpool who helped me in the development of the thesis, in particular I would like to thank my co-supervisors Prof. J. E. Mottershead for the continuous support and for all the suggestions given, as well as Dr. S. Fichera for the support and time dedicated despite the unexpected events. I dedicate a special thanks to the PhD students and my friends from the University of Liverpool who actively participated to the experimental development phase and to the meetings, giving me tips and useful suggestions. Finally, I would like to thank my partner who supported me despite the great distance and my family which always helped me, in particular I would like to thank my father for having supported me despite the difficulties.

Sommario

Il progetto di tesi è stato svolto interamente presso l' Università di Liverpool avendo accesso alla galleria del vento per eseguire i test sperimentali. La necessità di un nuovo modello sperimentale ha condotto alla progettazione dello stesso come prima attività. Nello specifico, è stato ri-progettato un modello di ala a due gradi di libertà con movimento torsionale e flessionale (pitch e plunge), dotato di due superfici di controllo attivo, rispettivamente, il flap anteriore e quello posteriore (trailing- e leading-edge flap). La progettazione ha tenuto conto della necessità di adattamento dell'ala alla struttura di supporto della galleria del vento e sono stati considerati sia gli aspetti funzionali dell'ala che le specifiche tecniche statiche e dinamiche necessarie al corretto funzionamento del modello. E' stato sviluppato un modello analitico con definizione instazionaria dei carichi aerodinamici per ottenere la predizione della velocità di flutter e per conoscere la dinamica interna del modello. Inoltre, sono stati eseguiti una serie di prove sperimentali volte ad individuare sperimentalmente la natura dinamica del modello quali: studio delle diverse velocità di flutter in base alla configurazione del sistema di molle e masse che sorregge il modello, studio delle risposte in frequenza con attuazione del sistema tramite shaker, con e senza vento, e tramite superfici di controllo attivo, con vento. E' stato eseguito l'aggiornamento del modello analitico al fine di validare tale modello sia dal punto di vista della predizione della velocità di flutter che dal punto di vista della dinamica interna. Infine, è stato studiato analiticamente e sperimentalmente il controllo attivo della struttura costituito da un controllore proporzionale derivativo integrale di basso livello ed un controllore proporzionale derivativo di alto livello. In particolare, dal punto di vista numerico, è stato sviluppato il controllo tramite una definizione quasi stazionaria dei carichi aerodinamici mentre, dal punto di vista sperimentale, sono stati scelti i guadagni del controllore di basso livello ed è stata testata l'efficacia del sistema di controllo. Infine, si è eseguito il piazzamento dei poli tramite l'implementazione numerica e sperimentale del receptance method.

Ringraziamenti

Per prima cosa desidero ringraziare il Prof. Bonisoli che mi ha permesso di vivere questa magnifica esperienza all'estero e che mi ha supportato lungo tutto il percorso di tesi. Un ringraziamento sincero và a tutto il team dell'Università di Liverpool che mi ha aiutato nello sviluppo della tesi, in particolar modo vorrei ringraziare i miei correlatori: il Prof. J. E. Mottershead per il supporto continuo e per tutti i suggerimenti datomi, nonchè il Dott. S. Fichera per il supporto e il tempo dedicatomi malgrado gli imprevisti che si sono sviluppati. Dedico uno speciale ringraziamento ai dottorandi e i miei amici dell'Università di Liverpool che hanno partecipato attivamente alla fase di sviluppo sperimentale ed agli incontri, dandomi consigli e suggerimenti utili. Infine, vorrei ringraziare la mia compagna che mi ha sostenuto durante tutto il periodo di svolgimento della tesi nonostante la grande distanza e la mia famiglia che mi ha sempre aiutato, di cui in particolar modo ringrazio mio papà per avermi supportato nonostante le difficoltà.

Contents

List of Tables

List of Figures

List of Notation and Acronyms

Symbol(s)	Meaning [Units]
h	plunge displacement [m]
α	pitch angle (or angle of attack of the aerofoil) [rad]
L	lift force [N]
D	drag force [N]
M	pitching or aerodynamic moment [Nm]
M_c	mid-chord
m_w	mass of the wing [kg]
m_s	mass of the external structure system [kg]
m_T	mass of the total system [kg]
I_c	moment of inertia of the aerofoil about the centre of mass [kgm^2]
k_h	plunge stiffness [N/m]
k_α	pitch stiffness [Nm/rad]
c_h	plunge damping [N/m]
c_α	pitch damping [Nm/rad]
ζ_h	plunge damping ratio [-]
ζ_α	pitch damping ratio [-]
V_c	velocity of centre of mass [m/s^2]
X_c	position of centre of mass [m/s]
I_α	moment of inertia of the aerofoil about the elastic axis [kgm^2]
S_α	static moment of inertia about elastic axis [kgm]
C_L	coeffiecient of lift [-]
C_D	coeffiecient of drag [-]
C_M	coeffiecient of pitching moment [-]
ρ	air density, density [kg/m^3]
U	air-speed [m/s], potential energy [J]
T	kinetic energy [J]
$\mathcal{F}$	Rayleigh dissipation function [J]
Q_i	generalised force [N]
q_i	generalised coordinates and state variable
s_p	span length [m]
a	non-dimensional distance between semi-chord and elastic axis, normalised by b [-]
b	semi-chord [m]
c	chord [m]
x_a	non-dimensional distance between centre of mass and elastic axis, normalised by b [-]

Symbol(s)	Meaning [Units]
ω_h	plunge frequency [rad/s]
ω_α	pitch frequency [rad/s]
ω_n	natural frequency [rad/s]
ω	frequency [rad/s]
σ	decay rate [1/s]
$\boldsymbol{A}$	structural inertia matrix
$\boldsymbol{D}$	structural damping matrix
$\boldsymbol{E}$	structural stiffness matrix
$\boldsymbol{A_a}$	aerodynamic inertia matrix
$\boldsymbol{B}$	aerodynamic damping matrix
$\boldsymbol{C}$	aerodynamic stiffness matrix
$\boldsymbol{N}$	aerodynamic states matrix
$\boldsymbol{A_{ss}}$	dynamic matrix of state space
$\boldsymbol{B_{ss}}$	input gain matrix of state space
$\boldsymbol{C_{ss}}$	output gain matrix of state space
$\boldsymbol{D_{ss}}$	direct link matrix of state space
$\boldsymbol{M_m}$	system inertia matrix
$\boldsymbol{C_m}$	system damping matrix
$\boldsymbol{K_m}$	system stiffness matrix
$\boldsymbol{z}$	general state space vector
$\boldsymbol{y}$	output vector
$\boldsymbol{u}$	input vector
$\boldsymbol{q}$	plunge displacement and pitch angle vector
$\boldsymbol{x}$	state vector for the unsteady loads definition
$\boldsymbol{B_c}$	control matrix of configuration space
$\boldsymbol{F}$	proportional gain matrix of the PD control
$\boldsymbol{G}$	derivative gain matrix of the PD control
k	reduced frequency of Theodorsen's model [1/s]
c_{L_0}	coefficient of lift due by the chamber shape of the aerofoil
c_{L_1}	coefficient of lift per pitch angle
c_{M_0}	coefficient of aerodynamic moment due by the chamber shape of aerofoil
γ	leading-edge flap angle [deg]
β	trailing-edge flap angle [deg]
C_{l_γ}	coefficient of lift for the leading-edge flap
C_{l_β}	coefficient of lift for the trailing-edge flap

Symbol(s)	Meaning [Units]
C_{m_γ}	coefficient of moment for leading-edge flap
C_{m_β}	coefficient of moment for trailing-edge flap
a_0	Jones' equation coefficient [-]
a_1	Jones' equation coefficient [-]
b_0	Jones' equation coefficient [-]
b_1	Jones' equation coefficient [-]
α_{μ_k}	arbitrary coefficient [-]
λ_k	open-loop eigenvalue
μ_k	closed-loop eigenvalue
$\boldsymbol{v_k}$	open-loop eigenvector
$\boldsymbol{w_k}$	closed-loop eigenvector
$\boldsymbol{Q_k}$	open-loop matrix for receptance method
$\boldsymbol{P_k}$	closed-loop matrix for receptance method
$\boldsymbol{R(s)}$	transfer function
PD	proportional derivative (control)
PID	proportional derivative integrative (control)
EVP	eigen-values problems
FRF	frequency response function
FDM	fuse deposition modelling
PMMA	polymethyl methacrylate
ABS	acrylonitrile butadiene styrene (polymer)
DOFs	degree of freedom
Cm	centre of mass
Ea	elastic axis
Ac	aerodynamic centre

Chapter 1

Introduction

1.1 Content

Since the first half of the twentieth century, aeroelasticity has had a central role in the design of new aircraft and in general in the aerospace engineering. Aeroelasticity links the inertial and elastic forces with the aerodynamic forces which are developed by a lifting surface dipped in a fluid flow. The aeroelastic problem are linked mainly to:

- *static problems*: these phenomena are time invariant and therefore they appear suddenly, such as the aeroelastic divergence or the reversal control surface;
- *dynamic problems*: these phenomena are strictly linked to the time and to inertial forces, such as the flutter.

For the first airplanes, the problems were related to the *divergence*, which leads the wings to deflect until the failure point. In fact a lot of first world war's airplanes crashed for torsional divergence. When the divergence appears, the lifting surface starts to deflect and this deflection causes an increase of the aerodynamic loads which worsens the situation; this phenomenon ends with the failure of the aerodynamic surface. The static divergence can be easily controlled by making the wing stiffer to avoid the initial deflection.

The divergence appears at higher wind speed respect to *flutter*. The flutter is one of the most dangerous and important aeroelastic phenomenon which can be defined as: *a dynamic instability of a flight vehicle associated with the interaction of aerodynamic, elastic, and inertial forces* [1]. The instability creates a self-excited aeroelastic vibration caused by the coupling of the natural system's modes. In this particular conditions, the fluid flow excites the structure and the amplitude of the oscillations increases. The flutter in linear systems appears as uncontrolled and unbounded oscillation which leads to the structural failure while in non-linear system, it appears as a limit cycle oscillations (LCO) in which the structure oscillates with large constant amplitude. In a linear model, the global effect is a decrease of net structure's damping which reaches to the zero net damping point at the flutter-speed. In fact the flutter-speed corresponds to the aerodynamic condition for which the negative aerodynamic damping is equal to the positive structural one; therefore a little increase of the flow speed would lead to the dynamic instability of the structure.

Numerous linear and non-linear models have been developed in order to study the main phenomena that occur in the structures subjected to action of wind. Basically, these phenomena can not be completely eliminated but just controlled or avoided, therefore the necessity of active and passive controls on the aerodynamic structures is became mandatory for the new designs of aircraft.

1.2 Literature review

Extensive studies have been conducted in the past years to find a way to control the onset of the flutter both in linear and non-linear structures.

Theodore Theodorsen [5] in 1935 validated the definition of the aeroelastic unsteady forcing functions for a three-DOFs rigid aerodynamic system in which the structure can be controlled by a trailing-edge flap that represents the third degree of freedom; the Theodorsen's model is still used today in the simplest analytical models to compute the flutter-speed or the system dynamics.

Mottershead et al. [10] described the theory of the MIMO version of the receptance method through which it is possible to perform the pole placement. This method can be applied on different types of structure and also on aerodynamic structure in order to control the flutter onset.

In the recent years the research focused on the control and suppression of flutter in linear and non-linear system.

Strganac et al. [7] investigated a non-linear control technique for the suppression of LCO in a two-DOFs aeroelastic system by using an analytical model based on the definition of the aerodynamic quasi-steady forcing function. An experimental model with two controlled surfaces, respectively leading-edge flap and trailing-edge flap, was used to validated the analytical model and the control law which applies the feedback linearisation technique.

Bhoir and Singh [6] studied a non-linear two-DOFs system by developing an analytical model with full unsteady forcing function. The model with just the trailing-edge control surface, has been used to compute the flutter-speed and to obtain the limit cycle oscillations of the system and the Theodorsen's function was treated as a second order transfer function to solve the equation of motion. The feedback linearisation technique was used to apply a control law on the non-linear system.

Jiffri, Fichera et al. [8] presented an experimental implementation of a non-linear pitch-plunge aeroelastic system. An analytical model was developed to describe the behaviour of the system and by using an experimental rig it was validated. A tuned embedded numerical model was used to control the structure and to apply the feedback linearisation technique through which the pole-placement of the system is applied .

Isnardi, Paoletti et al. [9] investigated numerically a feedback linearisation control technique for suppression of limit cycles oscillations in a non-linear two-DOFs aeroelastic model. The model was also experimentally validated by using an experimental rig in the wind tunnel and the mathematical model has been updated by using the frequency response function at zero wind speed. The gains for the LCO suppression have been tested below and above the flutter-speed in order to validate the control efficiency.

Mokrani, Palazzo et al. [11] developed a control system based on the receptance method for a flexible wing equipped with leading- and trailing-edge flaps. It has been demonstrated the efficiency of the receptance method in the pole placement of the system by using a FEM numerical model to compute the mode shapes of the wing and so it has been validated the ability of the control to suppress the flutter onset.

Mokrani et al. [14] developed a theory to minimize the control effort of system when the receptance method is applied. This technique can be applied on different structure, such as the aerodynamic structures, and it is possible to have the best control efficiency.

The researches of the last ten years are, therefore, focused on the control system for flutter suppression in different fields of the aerodynamics and so it is very important to have a better, simpler and more efficient way to control the system.

1.3 Aims and objects

The main aim of this project is to validate experimentally an analytical model of a linear pitch-plunge aeroelastic system by using an experimental rig. The mathematical model has to be able to predict the onset of the flutter and to deal with active controls, in particular it has to deal with two controlled surfaces: the leading-edge flap and the trailing-edge flap. These surfaces can suppress the occurring of the flutter by controlling the system. Through the implementation of the receptance method, the model has to be able to control the system's poles by making the classic pole placement. A new physical wing model has to be re-designed to simulate a two-DOFs system with pitch and plunge motions. The design is performed by using the CAD software CATIA through which all the parts of the wing can be modelled and adapted to the support structure. The new model is manufactured entirely in the University of Liverpool by using the workshop and the 3D printers.

Chapter 2

Analytical Model

An analytical model developed in MATLAB is used to describe the dynamic behaviour of the system. It is possible to resort to a simple mathematical description because the aeroelastic model can be idealised as a two-DOFs system. There are many advantages in the use of an analytical model: first of all, it is very simple and therefore computationally inexpensive and second, it can be built without using any other programs or subroutines. The analytical model has to be able to compute the dynamic behaviour of the system and to predict the flutter onset for a two-DOFs system. A schematic representation of the system is shown in Figure 2.1

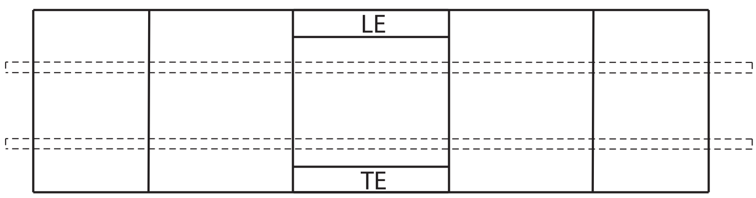

Figure 2.1: General scheme of the physical model, top view.

The dotted line represents the main spars used to support all the parts of the wing model. The model presents two control surfaces: the leading- and trailing-edge. They are able to control the system near to the flutter-speed by acting on the damping or the frequency of the controlled structure.

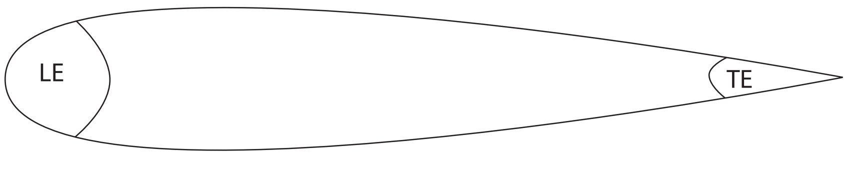

Figure 2.2: General scheme of the physical model, lateral section view.

2.1 Structural model

The analytical model starts from the simplest operative condition, i.e. when there is no air-flow and when the control surfaces are fixed and aligned with the wing profile. In this case only the structural behaviour of the wing is taken into account. The mid-chord is chosen as origin of the reference system in order to be aligned with the models described on the literature. Figure 2.3 shows the scheme of the analytical model. Generally, in aerodynamics, the reference system used to describe the dimensions of the wing is assumed to be positive upward and backward; therefore the dimensionless quantity a is negative. The plunge displacement h is assumed to be positive downward while the pitch angle α is assumed to be positive clock-wise. For the sake of simplicity, all the symbols are listed in *Acronyms and Abbreviations*.

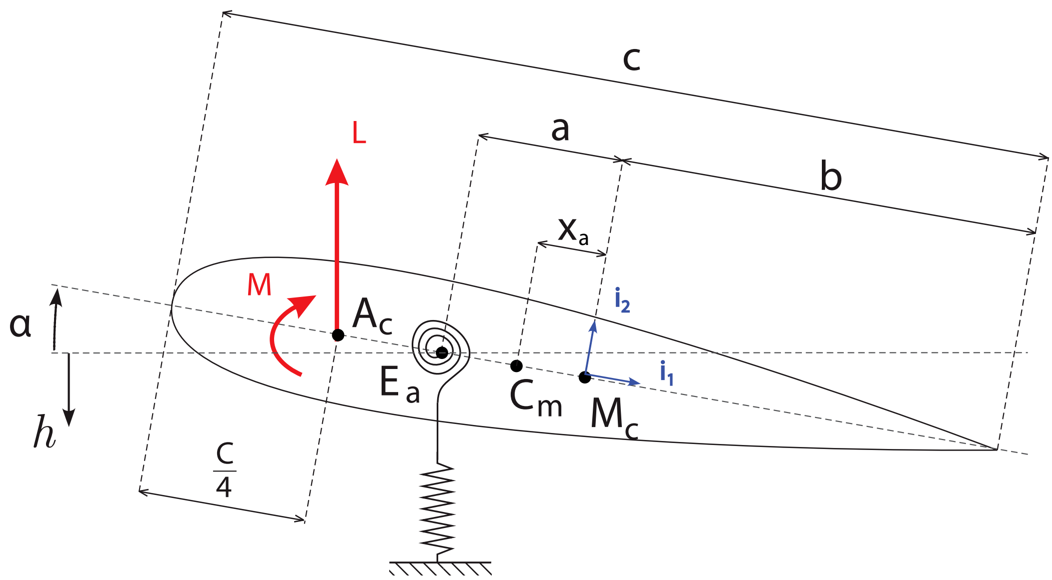

Figure 2.3: Mathematical model.

As shown in Figure 2.3, the lift L and the aerodynamic moment M are placed at the quarter of the chord from the leading-edge tip. A typical assumption in aerodynamic provides for placing the aerodynamic forces at that point: theoretically in an aerodynamic profile, the best point in which applying the lift is the center of pressure. This point is moving along the chord on the base of the change of lift, so it is better to apply the aerodynamic forces on the aerodynamic centre. The latter is the place in which the aerodynamic moment is not dependent on the lift and it is positioned near the quarter of chord for any subsonic aerofoil.

The equation of motion can be obtained by applying the Lagrange's method on the previously described model.

$$\frac{d}{dt}\left(\frac{\partial T}{\partial \dot{q}_i}\right) - \frac{d}{dt}\left(\frac{\partial U}{\partial \dot{q}_i}\right) + \frac{\partial U}{\partial q_i} - \frac{\partial T}{\partial q_i} + \frac{\partial \mathcal{F}}{\partial \dot{q}_i} = Q_i \tag{2.1}$$

In the case in point, the generalized coordinates q_i are represented by the two DOF of the system: h and α. Now, it is possible to obtain the kinetic and potential energy of the system by applying their definitions. The kinetic energy can be written as:

$$T = \frac{1}{2}m_w V_c^2 + \frac{1}{2}I_c\dot{\alpha}^2 \tag{2.2}$$

By considering the reference system and the sign convention of the pitch angle and plunge displacement, it is possible to write the position of the centre of mass with the approximation of small pitch angle (α«1).

$$X_c = -h + x_a b\alpha \tag{2.3}$$

By deriving in time the equation 2.3 of the centre of mass is possible to get the velocity of the centre of mass.

$$V_c = -\dot{h} + x_a b\dot{\alpha} \tag{2.4}$$

By replacing the Equation 2.4 in the Equation 2.2, is possible to obtain a simpler definition of the kinetic energy in terms of pitch angle and plunge displacement.

$$T = \frac{1}{2}m_w\dot{h}^2 + \frac{1}{2}I_\alpha\dot{\alpha}^2 + S_\alpha\dot{h}\dot{\alpha} \tag{2.5}$$

Where:

- $m_w = \int \rho dx$ represents the mass of the wing.
- S_α is the static moment of the structure.
- I_α is the moment of inertia about the elastic axis.

It is possible to compute the static moment and the moment of inertia as follows:

$$I_\alpha = I_c + m_w(x_a b)^2 \tag{2.6}$$

$$S_\alpha = \int \rho x dx = m_w x_a b \tag{2.7}$$

The potential energy and the Rayleigh's dissipation function can be expressed with the same formulation, by only applying the definition. In this case, it is adopted a dissipative function with the same form of the potential energy.

$$U = \frac{1}{2}k_h h^2 + \frac{1}{2}k_\alpha \alpha^2 \tag{2.8}$$

$$\mathcal{F} = \frac{1}{2}c_h \dot{h}^2 + \frac{1}{2}c_\alpha \dot{\alpha}^2 \tag{2.9}$$

Now, by replacing the Equations 2.5, 2.8 and 2.9 in the Lagrage's equation 2.1 it is possible to obtain the equation of motion of the system. In a reordered form, the equation of motion is:

$$\begin{bmatrix} m_T & S_\alpha \\ S_\alpha & I_\alpha \end{bmatrix} \begin{Bmatrix} \ddot{h} \\ \ddot{\alpha} \end{Bmatrix} + \begin{bmatrix} c_h & 0 \\ 0 & c_\alpha \end{bmatrix} \begin{Bmatrix} \dot{h} \\ \dot{\alpha} \end{Bmatrix} + \begin{bmatrix} k_h & 0 \\ 0 & k_\alpha \end{bmatrix} \begin{Bmatrix} h \\ \alpha \end{Bmatrix} = \begin{Bmatrix} -L \\ M \end{Bmatrix} \tag{2.10}$$

In this work, the wing is connected to an experimental rig that allows the pitch and plunge motion of structure, as explained in *Chapter 3*. The mass m_w represents only a portion of the total mass of the system. The mass of the structure is taken into account only in the first equation because it affects only the plunge motion of the model and it is the sum of the two masses: $m_T = m_w + m_s$. The equation of motion of the linear system is described by the Equation 2.10 and it is possible to notice that the stiffness matrix and the damping matrix are diagonal whereas the mass matrix is just symmetric because it contains the out of diagonal terms S_α. These terms couple the two DOF of the system from the inertia point of view. Mass, damping and stiffness matrices are generally renamed with the short notation shown in 2.11.

$$\mathbf{A}\ddot{\mathbf{q}} + \mathbf{D}\dot{\mathbf{q}} + \mathbf{E}\mathbf{q} = \mathbf{F} \tag{2.11}$$

It is necessary to use this notation because the aerodynamic loads will give a contribution in terms of aerodynamic inertia, damping and stiffness.
By focusing on the unforced, system the equation of motion becomes:

$$\mathbf{A}\ddot{\mathbf{q}} + \mathbf{D}\dot{\mathbf{q}} + \mathbf{E}\mathbf{q} = \mathbf{0} \tag{2.12}$$

The Equation 2.12 represents the dynamic of the system when there is no wind. It is possible to get the poles of the system by solving the eigenvalues problem with the mass and stiffness matrices, but it is also possible to compute the natural frequency of each mode in a approximate way by using the Equation 4.1.

$$\omega_h = \sqrt{\frac{k_h}{m_T}} \qquad \omega_\alpha = \sqrt{\frac{k_\alpha}{I_\alpha}} \tag{2.13}$$

These frequencies represent the natural frequencies of the system when the two DOFs are completely uncoupled and when the damping of the system is null. It is possible to compute the frequencies and decay rates of the system in a general case by using the state space approach and making a complex modal analysis. The system has to be re-written with the state space vector which is represented by the Equation 2.14.

$$\mathbf{z} = \begin{Bmatrix} \mathbf{q} \\ \dot{\mathbf{q}} \end{Bmatrix} \tag{2.14}$$

By rearranging the homogeneous equation of motion, it is possible to get the state space form of the system as shown in 2.15

$$\dot{\mathbf{z}} = \mathbf{A_{ss}} \mathbf{z} \tag{2.15}$$

Since there is no control applied on the structure, just the dynamic matrix is enough to describe the system . The dynamic matrix is represented by the Equation 2.16 and, on the base of the system DOFs, it belongs to $\mathcal{R}^{4\times4}$.

$$\begin{bmatrix} A_{ss} \end{bmatrix} = \begin{bmatrix} \mathbf{0_{2\times2}} & \mathbf{I_{2\times2}} \\ -\mathbf{A}^{-1}\mathbf{E} & -\mathbf{A}^{-1}\mathbf{D} \end{bmatrix} \tag{2.16}$$

Where $\mathbf{0_{2\times2}}$ is the null matrix and $\mathbf{I_{2\times2}}$ is the identical matrix. It is important to remember that the dynamic matrix belong to control representation of system expressed by the quadruple of the matrices: A_{ss}, B_{ss}, C_{ss}, and D_{ss} as shown in the Equation 2.17.

$$\begin{cases} \dot{\mathbf{z}} = \mathbf{A_{ss}}\mathbf{z} + \mathbf{B_{ss}}\mathbf{u} \\ \mathbf{y} = \mathbf{C_{ss}}\mathbf{z} + \mathbf{D_{ss}}\mathbf{u} \end{cases} \tag{2.18}$$

2.2 Aerodynamic model

The aerodynamic loads affect the inertia, damping and stiffness structural matrices of the system. Their effect increases as a function of the wind-speed, therefore the aerodynamic matrices have a direct proportional link with the wind-speed. There are different approximations to describe the influence of the aerodynamic on the system; generally it is possible to distinguish the following cases:

- Steady aerodynamic loads assumption;
- Quasi-steady aerodynamic loads assumption;
- Unsteady aerodynamic loads assumption.

The aerodynamic contributions change on the base of the adopted approximation. All the models provide for having the following basic hypotheses:

- Two dimensional flow;
- Inviscid flow;
- Incompressible flow ($M_a < 0.3$);
- Thin rigid section aerofoil;
- Small amplitudes.

The steady aerodynamic loads assumption is the simplest condition that is possible to assume. In this case the aerodynamic forcing function is dependent only on the pitch angle and plunge displacement:

$$F = F(h, \alpha) \tag{2.19}$$

This loads definition is not very accurate in the simplest aerodynamic models such as a two-DOFs model. In fact, it does not take into account the unsteady effect of the lift. Therefore, the use of more sophisticated definitions is necessary. The quasi-steady and unsteady aerodynamic loads assumptions allow to describe the phenomenon in a better way and therefore they give better results in terms of flutter prediction when the unsteadiness of the loads is large. In the first case the aerodynamic forcing can be written as:

$$F = F(h, \alpha, \dot{h}, \dot{\alpha}) \tag{2.20}$$

In the second case the aerodynamic loads are dependent also on the plunge acceleration and on the angular pitch acceleration , therefore is possible to write:

$$F = F(h, \alpha, \dot{h}, \dot{\alpha}, \ddot{h}, \ddot{\alpha}) \tag{2.21}$$

The quasi-steady loads assumption takes into account partially the unsteadiness of the aerodynamic loads while the total unsteady assumption considers all the unsteady phenomenon. With the complete unsteady approach, the flutter prediction is much more accurate but the model is more complex from the mathematical point of view. The unsteadiness of the aerodynamic loads is mainly due by two factors:

- the presence of wake with vortexes;
- the transitory effect;

The air vortexes in the wake is the main cause of aerodynamic loads unsteadiness: the wake arises when the air-flow passes along the aerofoil and initially it is smooth and straight but after few moments some vortexes occur behind the tail of the aerofoil. The vortexes make the aerodynamic loads unsteady and so the dependence of the loads is not only linked to the air-speed and to the pitch angle but also to the past motion history of the aerofoil; in other words, the wake affects the lift. The unsteady loads effect are proportional to the amplitude and the frequency of the wake oscillations, i.e. the unsteadiness is small if the system does not oscillates while it is large if the system oscillates. Also the transitory effect in the lift, when there is a changing in pitch angle, creates an effect of unsteady condition because the lift does not change suddenly but gradually. The unsteadiness is strictly related to the frequency content of the forcing function which is represented by a dimensionless variable k: the reduced frequency.

$$k = \frac{\omega b}{U} \tag{2.22}$$

The physical relationship between the reduced frequency and its parameters is expressed by the following states :

- as much the semi-chord b is small as the unsteadiness of the aerodynamic forces is reduced, i.e. a wing with a short chord is not long enough to develop a large vorticity in the wake;
- if the frequency ω is small the unsteadiness of the aerodynamic forces is small as well, i.e. low frequency oscillations do not create too much vorticity in the wake behind the tail;
- as much the wind-speed U is large as the effect of unsteadiness in the aerodynamic forces is small, in fact, the vorticity of the wake steps away quickly from the airfoil.

It is possible to imagine the effect of a large reduced frequency by making the inverse reasoning. Therefore the k is an indicator of the unsteadiness of the aerodynamic loads. It is possible to distinguish which approach is better for the studied system:

- Steady approach if k=0;
- Quasi-steady approach if $k \leq 0.1$;
- Unsteady approach if $k > 0.1$.

2.2.1 Steady aerodynamic loads assumption

The steady aerodynamic loads assumption is very simple and is a good representation of the dynamic behaviour of an aeroelastic system when the reduced frequency is very small. In this case, it is possible to write the equation of lift and pitching moment in the following way:

$$L = \frac{1}{2} C_L \rho U^2 s_p c = \frac{1}{2}(c_{L0} + c_{L1}\alpha)\rho U^2 s_p c \tag{2.23}$$

$$M = \frac{1}{2} C_M \rho U^2 s_p c^2 \tag{2.24}$$

Where c_{L_1} represents the coefficient per pitch angle for the lift and while c_{L_0} represents the value of lift coefficient for $\alpha = 0$. In a general representation the coefficient C_M depends on the lift position along the chord, but by using the aerodynamic centre as application point for the aerodynamic forces there is not this dependence anymore. It is possible to state the following correspondence:

$$C_M = c_{M_0} \tag{2.25}$$

In the case in point, c_{M_0} represents the coefficient of aerodynamic moment due by the chambered shape of the airfoil. The NACA 0018 is a symmetric profile and so both the coefficient c_{M_0} and c_{L_0} are equal to zero while c_{L_1} is equal to 2π .

Now it is possible to re-write the forcing function vector as appears in the Equations 2.26 :

$$\begin{Bmatrix} -L \\ M \end{Bmatrix} = \rho U^2 \begin{bmatrix} 0 & -\frac{1}{2} c_{L_1} c s_p \\ 0 & \frac{1}{2} c_{M_0} c s_p \end{bmatrix} \begin{Bmatrix} h \\ \alpha \end{Bmatrix} = \rho U^2 \begin{bmatrix} C \end{bmatrix} \begin{Bmatrix} q \end{Bmatrix} \tag{2.26}$$

It is possible to get the complete equation of motion with the aerodynamic effect by bringing on the other side the aerodynamic stiffness matrix $\mathbf{C}$ of equation 2.26.

$$\mathbf{A}\ddot{\mathbf{q}} + \mathbf{D}\dot{\mathbf{q}} + (\mathbf{E} - \rho U^2 \mathbf{C})\mathbf{q} = \mathbf{0} \tag{2.27}$$

For the sake of simplicity, it is convenient to pass to the compact notation expressed in the 2.28 in order to obtain the state space representation again.

$$\mathbf{M_m}\ddot{\mathbf{q}} + \mathbf{C_m}\dot{\mathbf{q}} + \mathbf{K_m}\mathbf{q} = \mathbf{0} \tag{2.28}$$

$$\begin{bmatrix} \mathbf{A_{ss}} \end{bmatrix} = \begin{bmatrix} \mathbf{0_{2\times 2}} & \mathbf{I_{2\times 2}} \\ -\mathbf{M_m}^{-1}\mathbf{K_m} & -\mathbf{M_m}^{-1}\mathbf{C_m} \end{bmatrix} \tag{2.29}$$

By computing the state space matrix of Equation 2.29 at each wind-speed and by solving the correlated eigenvalues problem (EVP) with the MATLAB function *eig*, it is possible to get the poles of the system for every value of the wind-speed U. From this results is possible to calculate when the damping becomes null and so it is possible to predict the flutter-speed. In fact the poles are composed by a real part and an imaginary part as described in Equation 2.30.

$$s = \sigma \pm i\omega \tag{2.30}$$

The real part and the imaginary part of the poles can be expressed as follows:

$$\begin{aligned} \sigma &= -\omega_n \zeta \\ \omega &= \omega_n \sqrt{1-\zeta^2} \end{aligned} \tag{2.31}$$

As explained before, this approach is not suitable for the flutter-speed computation of a two-DOFs system because the reduced frequency k is too high. Anyway, it is useful to understand the trends of the decay rates and of the frequencies in an aeroelastic model and to know the nature of the aerodynamic stiffness, damping and inertia matrices. From the mathematical point of view, we get only an aerodynamic stiffness matrix **C** from the definitions of the aerodynamic loads.

2.2.2 Theodorsen's unsteady model

The Theodorsen's model is commonly used for the flutter speed prediction and it adopts a complete unsteady approach to describe the aerodynamic forcing functions. Theodorsen has determined [5] the relationships which describe the aerodynamic forces of an oscillating three DOFs airfoil. The theory is based on potential flow and on the Kutta aerodynamic condition and it uses the Bessel function of the first and second kind to reach the solution. The problem has been investigated with the assumptions of small oscillation and with the approximation of infinite wing span. The Theodorsen's model provides for having the distinction between *circulatory terms* and *non-circulatory terms* of the aerodynamic loads. The first ones are related to the reduced frequency and so to the complete unsteadiness effect, whereas the second ones are apparent inertia forces that arise from the application of the aerodynamic loads. In order to apply the Thedorsen's aerodynamic loads on the two DOFs model, the influence of the flap is neglected. It is possible to get the representation of the forces in the following way:

$$L = \rho\pi b^2 s_p [\,\ddot{h} + U\dot{\alpha} - ba\ddot{\alpha}] + 2\pi\rho U b s_p C(k)\{\dot{h} + U\alpha + b(\tfrac{1}{2} - a)\dot{\alpha}\} \tag{2.32}$$

$$\begin{aligned} M =& \rho\pi b^2 s_p [\,ba\ddot{h} - Ub(\tfrac{1}{2} - a)\dot{\alpha} - b^2(\tfrac{1}{8} + a^2)\ddot{\alpha}] + 2\pi\rho U b^2 (a + \tfrac{1}{2}) s_p C(k) \\ & \{\dot{h} + U\alpha + b(\tfrac{1}{2} - a)\dot{\alpha}\} \end{aligned} \tag{2.33}$$

The Equations 2.32 and 2.33 represent the unsteady lift force and the unsteady aerodynamic moment for an aerofoil with two DOFs. The circulatory term is identified by the presence of the Theodorsen's function $C(k)$ while the remaining part of the equation represents the non-circulatory term. In order to obtain a solution similar to previous case, it is necessary to find a representation of the equation of motion of the kind:

$$(\mathbf{A} - \rho \mathbf{A_a})\ddot{\mathbf{q}} + (\mathbf{D} - \rho U \mathbf{B})\dot{\mathbf{q}} + (\mathbf{E} - \rho U^2 \mathbf{C})\mathbf{q} = \mathbf{0} \tag{2.34}$$

The function $C(k)$ is a frequency dependent term and it does not allow to get the solution of the flutter-speed prediction in straightforward way as in the previous steady case, therefore the Equation 2.34 can not be obtained by simply dividing the forcing term into three matrices. The Theodorsen's function $C(k)$ expresses the difference in term of lift between the different approaches for the definition of the aerodynamic loads, in particular between the quasi-steady and the unsteady definition of the loads. The function depends on the reduced frequency and it behaves as a filter: it receives an input and it gives an output. Therefore, the Theodorsen's function is a complex function represented by Equation 2.35:

$$C(k) = F(k) + iG(k) = \frac{H_1^{(2)}(k)}{H_1^{(2)}(k) + iH_0^{(2)}(k)} = \frac{K_1(ik)}{K_1(ik) + K_0(ik)} \tag{2.35}$$

where:

- $H_j^{(2)}(k)$ are the Hankel's function of the second type;
- $K_j(ik)$ are the Bessel's function of the second type.

The $C(k)$ function has to take into account both the real and the imaginary part. Since the Bessel's and Hankel's function are very complex and difficult functions, many approximation were developed in literature. One of the most used is the Jones' approximation that is represented on Equation 2.36

$$C(k) = 1 - \frac{0.165}{1 - \dfrac{0.0455}{k}i} - \frac{0.335}{1 - \dfrac{0.3}{k}i} \tag{2.36}$$

In the steady aerodynamics case the frequency ω is equal to zero, therefore the reduced frequency $k = 0$ and the real and imaginary part are respectively: $F = 1$ and $G = 0$. In this case the computation of the lift should be approximately the same for the steady, quasi-steady and the unsteady aerodynamic definition of the loads and so also the predicted flutter-speed should be the same.

2.2.3 Mathematical application of the Theodorsen's model

In order to have a simple mathematical solution, the Theodorsen's function can be treated as a filter and therefore it will be modelled as a transfer function. It is necessary a change of domain because it is difficult to handle the Jones' approximation with the variable k. The new variable will be the Laplace variable s that allows to find easily a simple representation of the transfer function. The Equation 2.37 represents the Jones' approximation of Theodorsen's function in Laplace domain.

$$C(k) = 0.5 + \frac{a_1 s + a_0}{s^2 + b_1 s + b_0} \tag{2.37}$$

Where the coefficients of Equation 2.37 are:

- $a_1 = 0.1080075 \, \frac{U}{b}$;
- $a_0 = 0.006825 \, \frac{U^2}{b^2}$;
- $b_1 = 0.3455 \, \frac{U}{b}$;
- $b_0 = 0.01365 \, \frac{U^2}{b^2}$.

The Equation 2.37 comes from the definition of reduced frequency:

$$k = \frac{sb}{iU} \tag{2.38}$$

The Theodorsen's function is now represented in Laplace domain, $C(s)$, as shown in Equation 2.37. For the sake of simplicity, it can be treated as a second order transfer function and Bhoir et al. in [6] explain how to write the correspondent filter by considering the input $v_f(s)$ and the output $y_f(s)$ as shown in Figure 2.4.

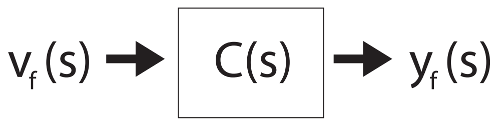

Figure 2.4: Filter description.

The representation in mathematical form is:

$$y_f(s) = C(s) v_f(s) \tag{2.39}$$

The input of the filter is a linear combination of the pitch angle and plunge displacement in time domain and it corresponds to the multiplying term of $C(s)$ in the circulatory part of the Theodorsen's loads. The input term in time domain is represented by the Equation 2.40:

$$v_f(t) = \alpha U + \dot{h} + b(0.5 - a)\dot{\alpha} \tag{2.40}$$

The vector $\mathbf{x_p}$ represents the state space variables used to solve the EVP in the state space form; i.e. they are the states used in the previous solution with the steady loads assumption. It is represented as follows:

$$x_p = \{h, \alpha, \dot{h}, \dot{\alpha}\}^T \tag{2.41}$$

The vector $\mathbf{a_v}$ has to be represented by Equation 2.42 in order to allow the definition of v_f with the vector multiplication.

$$a_v = \{0, U, 1, b(0.5 - a)\}^T \tag{2.42}$$

Although the transfer function $C(s)$ can be represented with a variety of filter representations with different numbers of states, it is better to define the filter with the minimal realization of states. Therefore the filter adds just two additional aerodynamic states, η_0 and η_1, which correspond the minimal realization of states.

$$\begin{cases} \dot{\eta_1} = \eta_1 \\ \dot{\eta_2} = -b_0\eta_1 - b_1\eta_2 + v_f(t) \end{cases} \tag{2.44}$$

Therefore it is possible to get the output $y_f(t)$ Equation 2.45 by applying the filter.

$$y_f(t) = 0.5\mathbf{a_v}^T\mathbf{x_p} + a_0\eta_1 + a_1\eta_0 \tag{2.45}$$

Now the output $y_f(t)$ is known and it is possible to replace the Equation 2.39 in the Equations 2.32 and 2.33 in order to get the solution. The system is now composed by six states because the filter introduces two new variables: η_1 and η_2. These new variable are the aerodynamic states. With this new configuration of the aerodynamic loads, it is possible to obtain the aerodynamic inertia, damping and stiffness matrix in similar way as in the case of loads steady approach. The result is expressed by the Equation 2.46 with the matrices belonging to $\mathcal{R}^{2\times2}$.

$$\mathbf{F} = \mathbf{A_a}\ddot{\mathbf{q}} + \mathbf{B}\dot{\mathbf{q}} + \mathbf{C}\mathbf{q} + \mathbf{N}\boldsymbol{\eta} \tag{2.46}$$

The matrices $\mathbf{A_a}$, $\mathbf{B}$, $\mathbf{C}$ and $\mathbf{N}$ can be found in the *Appendix*. By applying the new forcing function on Equation 2.11 and by bringing on the other side all the aerodynamic matrices it possible to get a representation similar to the Equations 2.34:

$$(\mathbf{A} - \rho \mathbf{A_a})\ddot{\mathbf{q}} + (\mathbf{D} - \rho U \mathbf{B})\dot{\mathbf{q}} + (\mathbf{E} - \rho U^2 \mathbf{C})\mathbf{q} = \mathbf{N}\boldsymbol{\eta} \tag{2.47}$$

As in the previous example, it is possible to get a more familiar expression of the equation of motion:

$$(\mathbf{M_m})\ddot{\mathbf{q}} + (\mathbf{C_m})\dot{\mathbf{q}} + (\mathbf{K_m})\mathbf{q} = \mathbf{N}\boldsymbol{\eta} \tag{2.48}$$

Finally, in order to get the state space representation the same passages as before can be done. The final result will be a dynamic system with just the matrix $\mathbf{A_{ss}}$. In important to remember that the number of states is increased as a consequence of the application of the filter. The equation 2.49 represents the new state variables:

$$\{x\} = \{h, \alpha, \dot{h}, \dot{\alpha}, \eta_1, \eta_2\}^T \tag{2.49}$$

By arranging all the equation with respect the new state variables, it is possible to get the matrix $\mathbf{A_{ss}}$ represented in Equation 2.50 with the state space representation. This new matrix will belong to $\mathcal{R}^{6\times 6}$.

$$\{\dot{x}\} = \begin{bmatrix} 0 & 0 & 1 & 0 & 0 & 0 \\ 0 & 0 & 0 & 1 & 0 & 0 \\ [& & & A_1 & &] \\ 0 & 0 & 0 & 0 & 0 & 1 \\ [& & a_v &]^T & -b_0 & -b_1 \end{bmatrix} \{x\} \tag{2.50}$$

where the matrix A_1 comes from the inversion of Equation 2.48 and it belongs to $\mathcal{R}^{2\times 6}$.

$$A_1 = [-\mathbf{M_m}^{-1}\mathbf{K_m}, -\mathbf{M_m}^{-1}\mathbf{C_m}, \mathbf{M_m}^{-1}\mathbf{N}] \tag{2.51}$$

As before, now it is possible to solve EVP by using the MATLAB function *eig* from which is possible to compute the poles of the system.

2.3 Numerical results

Previous experiments were conducted by Isnardi et al. [9] on the same test rig with a two DOFs wing, therefore some starting data are taken directly from [9] in order to test the model. The inertia properties and the dimensions of the wing can be evaluated with good approximation directly from the CAD model of the wing. The acquired data are listed in the Table 2.1 while the inertia properties and the dimensions are shown in Table 2.2 and 2.3.

The meaning of each symbol is described in the section *List of Notation and Acronyms*. The dimensionless parameters a and x_a can be evaluated from the CAD

Data	Acquired parameters
$\zeta_h[-]$	0.0183
$\zeta_\alpha[-]$	0.0082
$k_h[N/m]$	3514.8
$k_\alpha[Nm/rad]$	33.7

Table 2.1: Acquired parameters from [9].

Data	CAD inertia data
$m_T[kg]$	12.4518
$m_w[kg]$	4.913
$I_c[kgm^2]$	0.029

Table 2.2: Inertia data obtained from the CAD model.

wing model by using the reference system provided in the Figure 2.3 and the Equations 2.52 and 2.53.

$$a = \frac{E_a - M}{b} \tag{2.52}$$

Data	CAD dimension data
c [m]	0.3
b [m]	0.15
$s_p[m]$	1.2
a [-]	-0.32
$x_a[-]$	0.258

Table 2.3: Dimensions data acquired from the CAD model.

$$x_a = \left|\frac{C_m - E_a}{b}\right| \tag{2.53}$$

The parameter a is the dimensionless distance between the elastic axis and the mid-chord while x_a is the dimensionless distance between the elastic axis and the centre of mass. Since the centre of mass is positioned at 140.7 mm from the leading-edge tip and the elastic axis is positioned at 102 mm from the leading-edge tip, it is possible to compute a and x_a. It is possible to get the inertia moment and the static moment about the elastic axis by using the Equation 2.6 and 2.7, which are respectively: I_α=0.0364 Kgm^2 and S_α=0.1901 Kgm. By using these data, it is possible to get the natural frequencies of the plunge and the pitch motion at zero air-speed:

$$\omega_{plunge} = 16.5rad/s \quad \omega_{pitch} = 32.3rad/s \tag{2.54}$$

By using the estimated data, the reduced frequency is equal about to 0.26 for a wind-speed about $20m/s$, therefore it is necessary to use a complete unsteady approach to describe the aeroelastic dynamic behaviour of the system. Even if the parameters used to compute k are not the updated ones, the reduced frequency can not change a lot since only ω can change. Obviously, if the reduced frequency is very close to the limit value, it is possible to image very similar results between the quasi-steady and the unsteady approach. The unsteady approach is however the better approximation for the flutter speed prediction.

Some numerical tests are now performed and analyzed by using the models previously described with the steady and unsteady definition of the aerodynamic loads. The data of Tables 2.1, 2.2 and 2.3 are used to compute the numerical tests. The Figure 2.5 shows the trend of the real parts of the poles for each velocity when the steady model is adopted whereas the Figure 2.6 plots the trends of the imaginary part of the same model.

The Figure 2.5 shows when the system becomes unstable: until the real part of the poles is negative the system is stable because the total damping of the structure is positive but when the real part becomes positive the system becomes unstable because the total structure damping is negative. A system with a negative damping is unstable because the amplitude of oscillations, caused by initial disturbance, tends to diverge. The flutter speed is the velocity at which the system becomes unstable and with this model the flutter is predicted at 19.1 m/s. This first definition of aerodynamic loads tends to overestimate the flutter-speed. It is however possible to see that the flutter occurs when the frequencies of the two modes coalesce.

The same date are used with the unsteady model to compute the flutter-speed. Also in this case, by using the graph of Figure 2.7, it is possible to see when the structure becomes unstable.

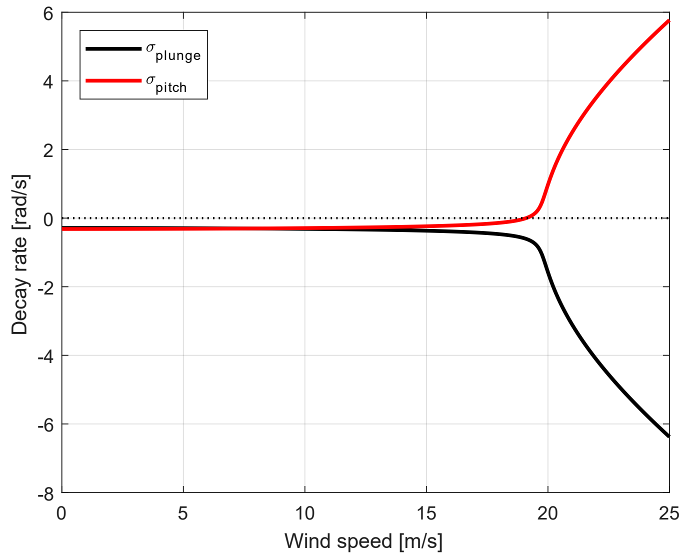

Figure 2.5: Decay rate trend for pitch and plunge mode with the steady loads assumption, the flutter appears when the real part of one poles becomes positive.

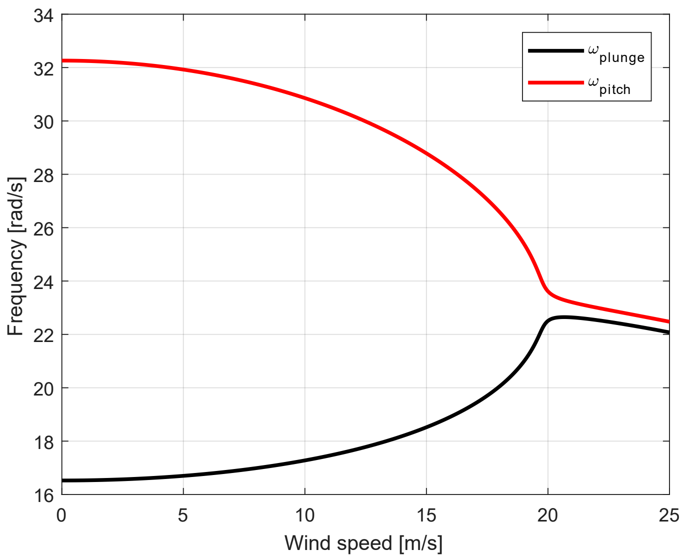

Figure 2.6: Frequency trend with the steady loads assumption, the flutter appears near to the cross of the two frequencies.

It is important to notice that with the unsteady model the flutter-speed is decreased a lot; in fact the new flutter-speed is 16.8 m/s. The reduction of flutter-speed is due by the unsteadiness of the aerodynamic loads which lead the wing to

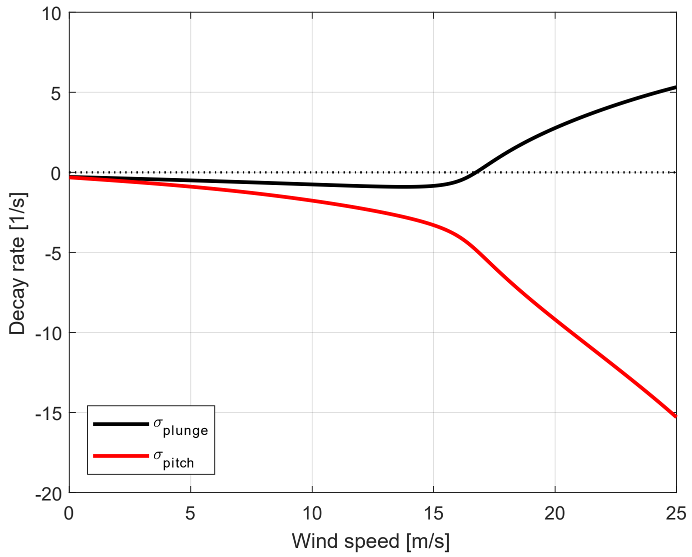

Figure 2.7: Real part of the poles vs wind-speed with unsteady loads assumption.

be unstable a lower speed.

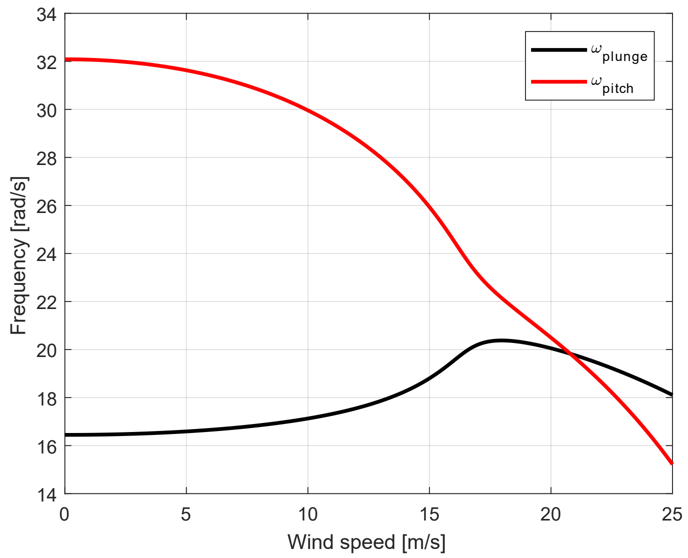

Figure 2.8: Imaginary part of the poles vs wind-speed with unsteady loads assumption.

The trend of the frequencies changes for the same reason. In a unsteady model the flutter appears near to the coalescence of the two structural modes but not exactly at that intersection because the damping becomes negative before.

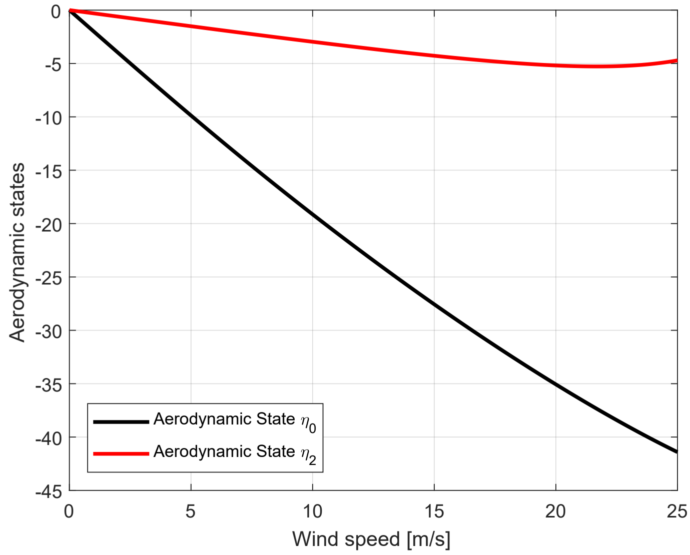

Figure 2.9: Aerodynamic states vs wind-speed obtained from the filter.

Finally, the Figure 2.9 shows the trend of the aerodynamic states in relation with the increase of wind-speed. These two additional variables come from the definition of the filter used in the model. These states have to be negative always to guarantee the stability of the structure.

2.4 Quasi-steady control system

The analytical model previously described represents just the internal dynamic of the aerofoil without any control surfaces, therefore the flaps action has to be added into the mathematical model in order to apply numerically and experimentally the controls. Theodorsen [5] showed the mathematical definition of the aerodynamic loads created by a trailing-edge flap with the loads unsteady definition but in the model in point there are two different control surfaces. Since an unsteady definition of the aerodynamic loads for both the control surfaces would make the model very difficult and complex, the aerodynamic loads related to flaps action are described through the quasi-steady definition. By using the definition of quasi-steady loads for the control surfaces and the definition of unsteady loads for the general dynamic of the wing, the final system is an hybrid system which takes into account both the definitions.

2.4.1 Numerical implementation and results

In order to apply numerically the method, it is necessary to create a control matrix $\mathbf{B_c}$ which represents the action of the flaps. The positive verse of the flaps angle and the control model are represented in Figure 2.10.

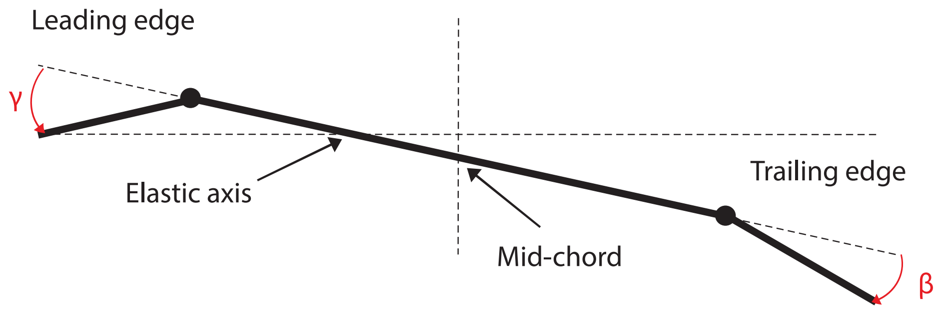

Figure 2.10: Representation of the model for the control.

The unsteady definitions of lift and aerodynamic moment described previously with the Equations 2.32 and 2.33 are now modified. In fact, the two flaps are able to modify the aerodynamic loads of the aerofoil by changing their angles, therefore it is necessary to add two additional terms on both the equations. Strganac et al. [7] used this approach on a symmetric wing profile with the flaps along all the wing's span. The same definition is now used and the additional terms appears as:

$$L_{add} = 0.25\rho U^2 b s_p (C_{l_\beta}\beta + C_{l_\gamma}\gamma) \tag{2.55}$$

$$M_{add} = 0.25\rho U^2 b^2 s_p (C_{m,eff_\beta}\beta + C_{m,eff_\gamma}\gamma) \tag{2.56}$$

The factor 0.25 takes into account the length of control surfaces which is 300 mm therefore the 25% of the total wing span of 1200 mm. The definition of the coefficient C_{m,eff_β} and C_{m,eff_γ} requires an additional step:

$$C_{m,eff} = (0.5 + a)C_l + 2C_m \tag{2.57}$$

The Equation 2.57 is used for both the control surfaces. The aerodynamic coefficients are listed in the Table 2.4. These coefficients comes from aerodynamic tests and so they are considered to be very robust, therefore there is no need to update the parameters for the new model.

The final lift and aerodynamic moment are respectively the sum of the Equations: 2.32 and 2.55, for the lift, and 2.33 and 2.56, for the aerodynamic moment. The following Equations represent the final aerodynamic loads with all the contributions:

Parameter	Leading-edge	Trailing-edge
C_l	-0.1566	3.774
C_m	-0.1005	-0.6719

Table 2.4: Aerodynamic parameters for quasi-steady definition of the loads for the two control surfaces obtained from [7].

$$
\begin{aligned}
L =& \rho\pi b^2 s_p[\,\ddot{h} + U\dot{\alpha} - ba\ddot{\alpha}] \,+ 2\pi\rho U b s_p C(k)\{\dot{h} + U\alpha + b(\frac{1}{2} - a)\dot{\alpha}\} \\
&+ 0.25\rho U^2 b s_p(C_{l_\beta}\beta + C_{l_\gamma}\gamma)
\end{aligned}
\tag{2.58}
$$

$$
\begin{aligned}
M =& \rho\pi b^2 s_p[\,ba\ddot{h} - Ub(\frac{1}{2} - a)\dot{\alpha} - b^2(\frac{1}{8} + a^2)\ddot{\alpha}] \,+ 2\pi\rho U b^2(a + \frac{1}{2})s_p C(k) \\
&\{\dot{h} + U\alpha + b(\frac{1}{2} - a)\dot{\alpha}\} + 0.25\rho U^2 b^2 s_p(C_{m,eff_\beta}\beta + C_{m,eff_\gamma}\gamma)
\end{aligned}
\tag{2.59}
$$

By re-applying the filter and the same passages as before, it is possible to obtain the matrix equation with an additional matrix $\mathbf{B_c}$ which represents control matrix.

$$
(\mathbf{A} - \rho\mathbf{A_a})\ddot{\mathbf{q}} + (\mathbf{D} - \rho U\mathbf{B})\dot{\mathbf{q}} + (\mathbf{E} - \rho U^2\mathbf{C})\mathbf{q} = \mathbf{N}\boldsymbol{\eta} + \mathbf{B_c}\mathbf{u} \tag{2.60}
$$

The Equation 2.60 represents the equation of motion and the vector $\mathbf{u} = [\gamma, \beta]^T$ is the input vector while the control matrix $\mathbf{B_c}$ can be obtained from the definition of the added aerodynamic forces of 2.58 and 2.59 and it appears as:

$$
B_c = \rho U^2 bsp0.25 \begin{bmatrix} -C_{l_\gamma} & -C_{l_\beta} \\ bC_{m_{eff,\gamma}} & bC_{m_{eff,\beta}} \end{bmatrix} \tag{2.61}
$$

Again, it is possible to write the system in a state space form by using the same state vector $\mathbf{x}$ as before but now the presence of the control matrix $\mathbf{B_c}$ leads to have the state space system with two matrices: the dynamic matrix $\mathbf{A_{ss}}$ and the input gain matrix $\mathbf{B_{ss}}$. By rearranging the all the equations as before, it is possible to obtain the state space representation in this form:

$$
\dot{\mathbf{x}} = \mathbf{A_{ss}}\mathbf{x} + \mathbf{B_{ss}}\mathbf{u} \tag{2.62}
$$

Where the input gain matrix is defined by:

$$
B_{ss} = \begin{bmatrix} \mathbf{0}_{2\times 2} \\ \mathbf{M_m}^{-1}\mathbf{B_c} \\ \mathbf{0}_{2\times 2} \end{bmatrix} \tag{2.63}
$$

Since $\mathbf{B_c} \in \mathrm{R}^{2\times2}$ the matrix $\mathbf{B_{ss}} \in \mathrm{R}^{6\times2}$. At this stage it is possible to write the complete state space system by adding the output gain matrix $\mathbf{C_{ss}}$ and direct link matrix $\mathbf{D_{ss}}$ which are represented by the following equations:

$$C_{ss} = \begin{bmatrix} 1 & 0 & 0 & 0 & 0 & 0 \\ 0 & 1 & 0 & 0 & 0 & 0 \end{bmatrix} \tag{2.64}$$

$$D_{ss} = \begin{bmatrix} 0 & 0 \\ 0 & 0 \end{bmatrix} \tag{2.65}$$

The matrix $\mathbf{D_{ss}}$ is set to zero because there are not feedback-through while $\mathbf{C_{ss}}$ represents the connection between the outputs $\mathbf{y}$ and state space variable $\mathbf{x}$. In this case the pitch angle and plunge displacement are chosen as outputs; in fact the in a numerical MIMO system it is possible to choose the required outputs by defining the matrix $\mathbf{C_{ss}}$. The uncontrolled system is completely described by the matrix $\mathbf{A_{ss}}$ while the controlled system requires an additional step to get the solution and therefore to obtain the poles. The gains matrices allow to create a link between the outputs and input that is described in the following equation:

$$\mathbf{u} = \mathbf{F}^T\dot{\mathbf{y}} + \mathbf{G}^T\mathbf{y} \tag{2.66}$$

In this case the $\mathbf{F}^T$ and $\mathbf{G}^T \in \mathrm{R}^{2\times2}$, the first one represents the matrices of the derivative gains whereas the second represents the matrices of the proportional gains. In the numerical model the outputs coincide with the pitch angle and plunge displacement, therefore there is no distinction between the outputs and the states since $\mathbf{y} = \mathbf{q}$. By replacing the Equation 2.66 in the state space definition of 2.62 and by rearranging, it is possible to get a new dynamic matrix which describes the closed-loop system:

$$\dot{\mathbf{x}} = [\mathbf{A_{ss}} + \mathbf{B_{ss}}[\mathbf{G}, \mathbf{F}, \mathbf{O_{2\times2}}]^T]\mathbf{x} \tag{2.67}$$

The new dynamic matrix with the control gains allows to get the poles of the controlled system by solving the correspondent EVP. The presence of two additional state leads to get an additional null matrix in the controlled system representation, in fact the aerodynamic states have not to be controlled. There are many ways to get the gains and to apply the pole placement but in this chapter the gains are chosen arbitrarily just to show numerically the effect of the control. In *Chapter 6* the receptance method will be used to find such gains and to place the pole. By choosing properly the gains, it is possible to control the system making it more stable or less stable. The same data as before are used to make some numerical tests.

Figure 2.11 shows the increase of predicted flutter-speed when some stable arbitrary gains are applied. The analytical model shows an increase of flutter-speed

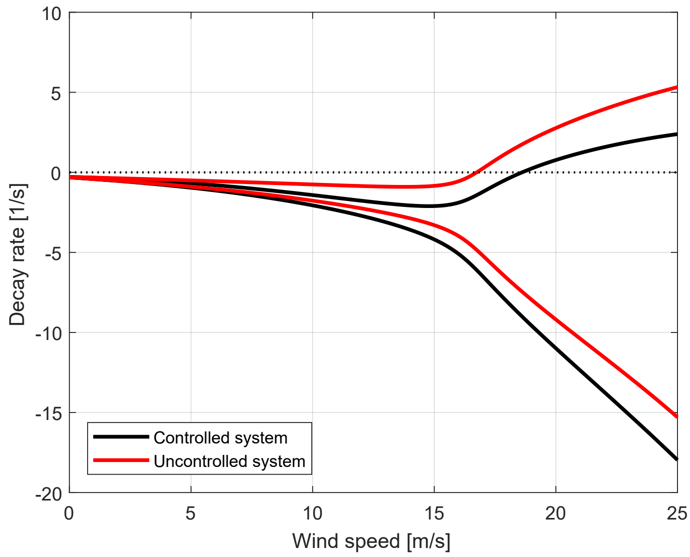

Figure 2.11: Numerical results, increase of flutter-speed by choosing the proper gains.

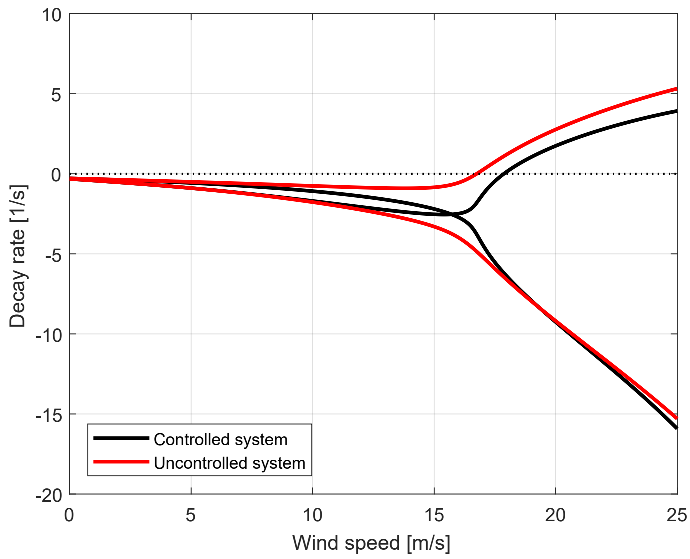

Figure 2.12: Numerical results, change of flutter mode.

from the natural one about 16.8 m/s to the controlled one of 18.6 m/s. In this case the flutter appears always with the plunge motion but it is possible to control the system so that the flutter instability appears in the pitch motion, as shown in Figure

2.12 where the flutter appears at 17.9 m/s. Therefore it is possible to control the system in the required way and it is also possible to choose the gains so that the flutter does not appears in the analyzed range as shown in Figure 2.13.

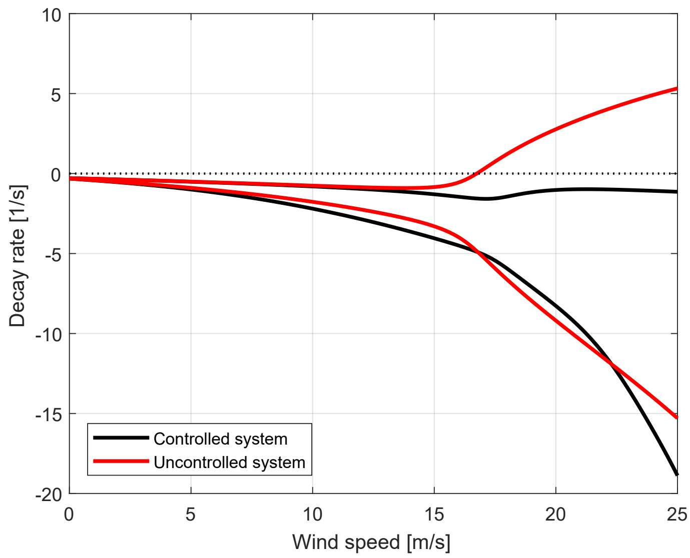

Figure 2.13: Numerical results, no flutter onset.

Chapter 3

Wing Design

To validate the mathematical model, a new physical wing model has been re-designed by starting from the design of similar structures [11]. The new model is used in the wind tunnel of the University of Liverpool and it has to simulate a two-DOFs pitch and plunge aeroelastic system. The new wing needs to fit exactly with the support structure of the wind tunnel in order to perform the experimental tests. The design has been performed by using the FEM program LUPOS and the CAD software CATIA through which all the parts have been calculated and modelled.

3.1 Wing model description

The idea is to create the new wing model by using two main spars as internal metallic structure and a modular design for all the additional plastic parts. The modular design makes easier the assembling process. The wing has to be very stiff in order to avoid elastic deformation and to allow just the pitch and the plunge motions when it is assembled with the support structure. All the sectors and plastic parts are printed with the Stratasys 3D printer which uses the FDM technique, a common material extrusion process in additive manufacturing field, while the metallic parts are manufactured in the University workshop. The material used by the 3D printer is the ABS, a thermoplastic polymer, that is chosen for its good properties like impact resistance and toughness. The standard NACA (National Advisory Committee for Aeronautics) is adopted to define the aerodynamic shape of each sector. The NACA aerofoils are often used to develop aerodynamic physical models because the profile section can be obtain by knowing just the dimension of the chord. The model has to be equipped with control surfaces in order to control the stability of the structure. The best way to control similar structure is to apply two control surfaces: a trailing- and a leading-edge flap as shown in the 3.1.

The application of two active surfaces is enough to have the complete control of

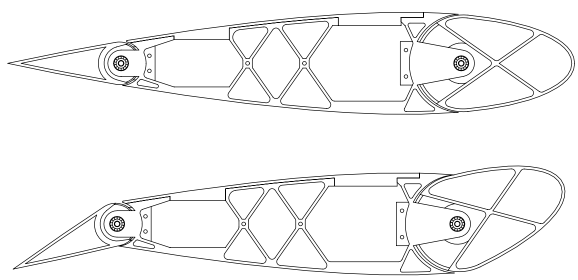

Figure 3.1: Active sectors, view 1.

the structure; in particular, the position of the flaps, rather than the number, allows to add damping and to change the natural frequencies as much as it is requested from the controller. In the previous experiments some different types of actuators were investigated , like the piezoelectric controls [9] or the electric motors [11], and the application of brush-less electrical motors led to better results. Therefore, two Maxon brush-less motors with a power of 60 W are chosen to control the leading- and trailing-edge flap. The motors are equipped with a planetary gears and encoder sensors: the first one allows to overtake the friction problems of the flaps by increasing the applied torque while the second one allows to know the angular position of the controlled surfaces. The support structure and the wing model are represented in the Figures 3.2 and 3.3. The structure is mainly composed by:

- aerofoil vertical support (1)
- plunge linear spring (2)
- aerofoil (3)
- pitch linear spring (4)
- external masses (5)

The plunge springs connect the wing to one extremity of the support structure and they consist into two steel plates placed in parallel. The pitch springs are realized by using a stinger and a smaller steel plate. All the steel plates are made in spring steel and they allow the regulations of the stiffness by changing the attaching position on the structure. The external structure allows to control the moment of inertia and the static moment of the wing by changing the position of two external masses as shown in Figure 3.3. The support structure allows to control the position of the centre of mass, the plunge stiffness and the pitch stiffness, therefore the onset of the flutter can be completely controlled and placed at the desired wind-speed.

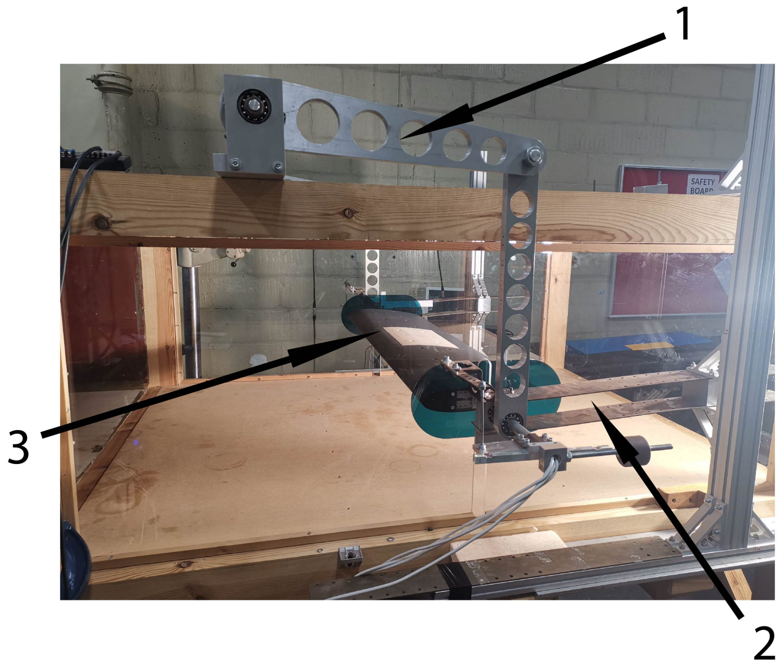

Figure 3.2: Support structure, view 1.

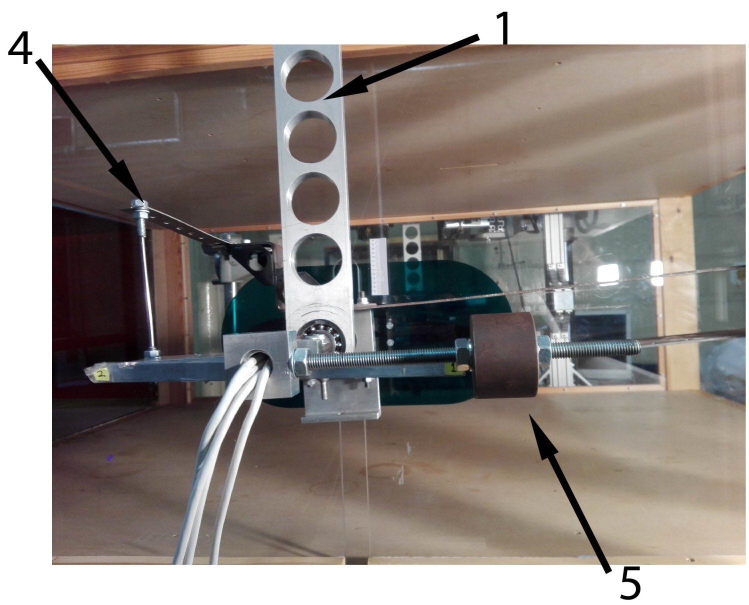

Figure 3.3: Support structure, view 2.

3.2 Design of the wing model

The design of the new wing is obtained through an iterative procedure that links the dynamic and static conditions with the shape of the model, therefore the FEM and the CAD models are use together to reach the final solution. The design constrains come from:

1. stiffness and dynamic conditions of the wing;
2. manufacturing constrains;
3. internal desing, motors allocation and assembling problems.

The manufacturing constrains are mainly imposed by the support structure and by the 3D-printer, in fact the new wing has to fit exactly with the external structure and each sector has to be lower than the maxima dimensions supported by the printer.

Constrain	**Value or type**
maximum span	1200 mm
maximum chord	300 mm
NACA $profile$	NACA 0018

Table 3.1: Design constraints imposed by machinery and support structure.

The stiffness and dynamic conditions of the model can be studied with the help of the FEM model. The wing is clamped at both ends as shown in Figure 3.2 and Figure 3.3 and so a modal analysis is necessary to understand the general dynamic behaviour of the wing model. The wing is studied by considering it clamped at both the extremities but actually, when it is assembled with the support structure, it acquires the possibility to move in rotation (pitch) and vertical direction (plunge); the support structure and the wing assembly represent the complete system that was studied in *Chapter 2*. The most important dynamic and static limitations are:

1. First natural frequency larger than $30 - 40\ Hz$.
2. Rotational deformation and deflection in the centre of the wing as lower as possible, with a maximum angle value about 0.5°.

These conditions are important to have a correct onset of the flutter phenomenon. When the aerofoil flies at increasing speed, the frequencies of the natural modes of the complete system coalesce to create one single mode at the flutter condition. This is the flutter resonance. The first imposed condition avoids dynamic interferences between the structural mode-shapes of the only wing model and the flutter resonance of the complete system; in fact if the first natural frequency of the wing is very closed to the frequency of pitch or plunge of the complete model, it could appear an interference between the modes. This fact could prevent the correct onset of the flutter. In *Chapter 2* an approximate pitch frequency were computed and, to be conservative, 30 Hz is chosen as minimum limit frequency. The second condition guarantees a very high stiffness. In order to satisfy these conditions a FEM model of the wing is developed in LUPOS, an open source FEM code that works in MATLAB environment, and it is performed a static and a modal analysis of the wing model. The assembling problems and internal allocation of the motor wires, and nevertheless the possibility to find on the market the required components, are the most difficult part of the design and they must be taken into account.

3.2.1 FEM model

Firstly, a very simple model is taken into account. After some preliminary tests, the first FEM model is obtained from the iterative procedure and this model is basically composed only by the internal metallic structure. To guarantee the correct stiffness of the structure, two rectangular hollow section bars are used to create a support structure for the wing and for all the sectors. The bars are made in aluminium to guarantee a lightweight structure. The Figure 3.4 shows the preliminary model developed in LUPOS.

In LUPOS the two main spars are modelled with beam elements, therefore they are able to withstand to bending and axial loads and the inertia properties are taken into account by applying the density of the material. As first approximation, the polymeric sectors are modelled with lumped masses and beams: the masses are distributed along the main spars and they represent the inertia properties of the sectors whereas some beams are used to connect the two spars to simulate the stiffness of the polymeric sectors.

The FEM model is composed by the element shown in Figure 3.4

- Front spar (1)
- Back spar (2)
- ABS element (3)
- Lumped mass (4)

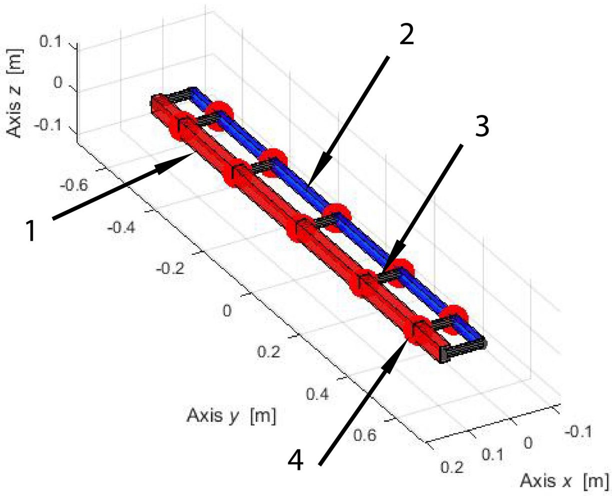

Figure 3.4: FEM model, the arrows indicate the used elements type.

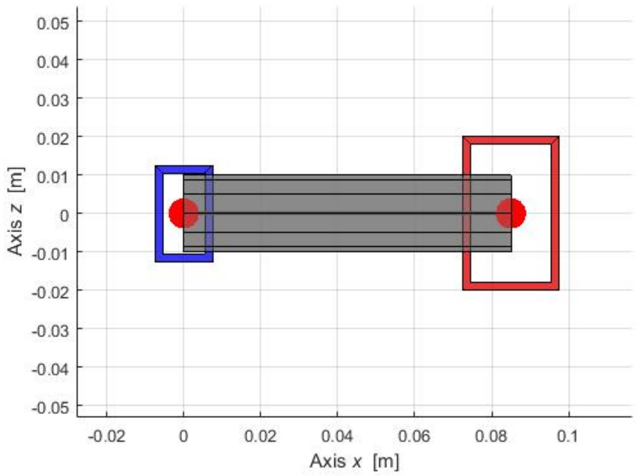

Figure 3.5: FEM model, lateral view.

3.2.2 Modal analysis

The dimensions of the two aluminium profiles are chosen on the base of the previous limit conditions. First of all, a modal analysis is carried out with the FEM program. The first modes are represented in Figures 3.6 and 3.9. Different sections are tested and the results of Table 3.2 are found. The ABS sectors are prudently modelled with a simple round equivalent beam and therefore in Table 3.2 ABS indicates equivalent diameter.

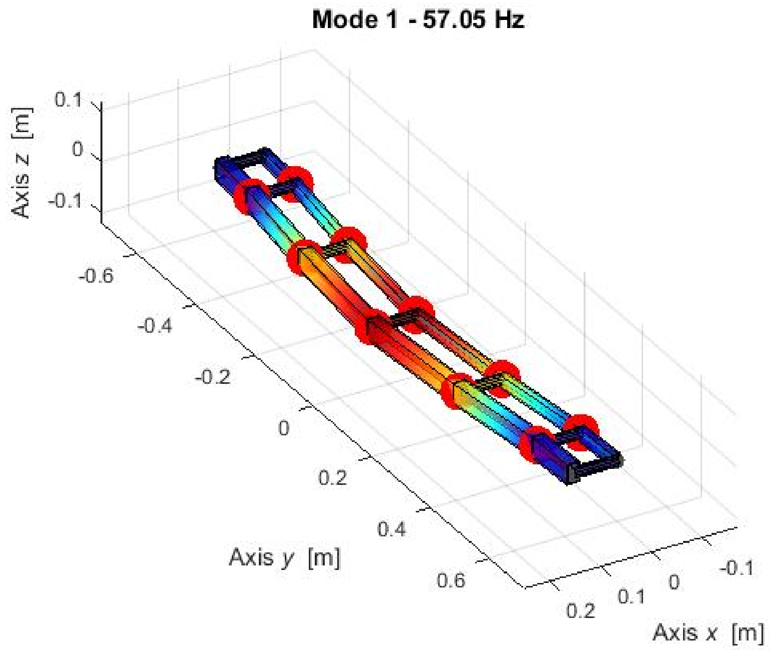

Figure 3.6: Modeshape 1.

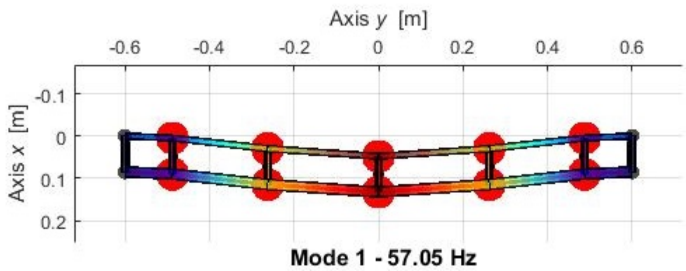

Figure 3.7: Top view, modeshape 1.

The results show that the moment of area changes on the base of the profile dimensions and this affects the first natural frequency of the system. All the natural frequencies of the wing model are larger than the frequencies of the pitch and of plunge of the complete model, therefore no modes coupling problems are present. In the first cases, the aluminium profiles have been chosen square and equal for the sake of simplicity. After few tests, the iterative procedure has led to get two spars different in size. This is important to allow the internal positioning of the two spars.

	Front spar	**Back spar**	**ABS**	$1^{st}\ f_n$	$2^{nd}\ f_n$
$Case$ 1	$20 \times 20 \times 1\ mm$	$20 \times 20 \times 1\ mm$	$10\ mm$	$32.8\ Hz$	$33.4\ Hz$
$Case$ 2	$30 \times 30 \times 1\ mm$	$30 \times 30 \times 1\ mm$	$10\ mm$	$59.8\ Hz$	$60.0\ Hz$
$Case$ 3	$30 \times 20 \times 1\ mm$	$30 \times 20 \times 1\ mm$	$10\ mm$	$38.7\ Hz$	$52.4\ Hz$
$Case$ 4	$30 \times 20 \times 2\ mm$	$30 \times 20 \times 2\ mm$	$10\ mm$	$47.9\ Hz$	$66.0\ Hz$
$Case$ 5	$40 \times 25 \times 2\ mm$	$25 \times 15 \times 2\ mm$	$10\ mm$	$54.0\ Hz$	$56.0\ Hz$
$Case$ 6	$40 \times 25 \times 2\ mm$	$25 \times 15 \times 2\ mm$	$20\ mm$	$57.0\ Hz$	$71.5\ Hz$

Table 3.2: First mode natural frequencies.

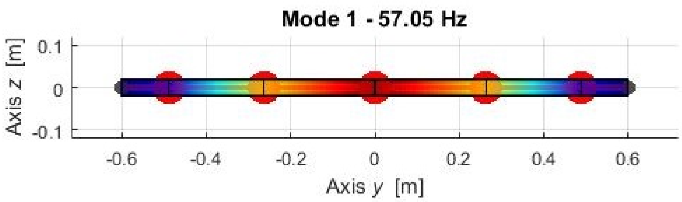

Figure 3.8: Front view, modeshape 1.

3.2.3 Static analysis

The static analysis and the modal analysis are performed simultaneously to get more accurate results. The static analysis consists in the checking of the maximum rotational angle in the centre of the wing when the lift and the aerodynamic moment are applied. In the bi-dimensional case the result aerodynamic force can be divided into two components: the lift and the drag.

$$L = \frac{1}{2} C_L \rho U^2 c s_p \tag{3.1}$$

$$D = \frac{1}{2} C_D \rho U^2 c s_p \tag{3.2}$$

The lift is the vertical component of the result force whereas the drag force is the horizontal one with respect the flight direction. The result force is applied on the centre of pressure of the aerofoil but this point is inconvenient to make a correct analysis of the model because the centre of pressure changes continuously its position

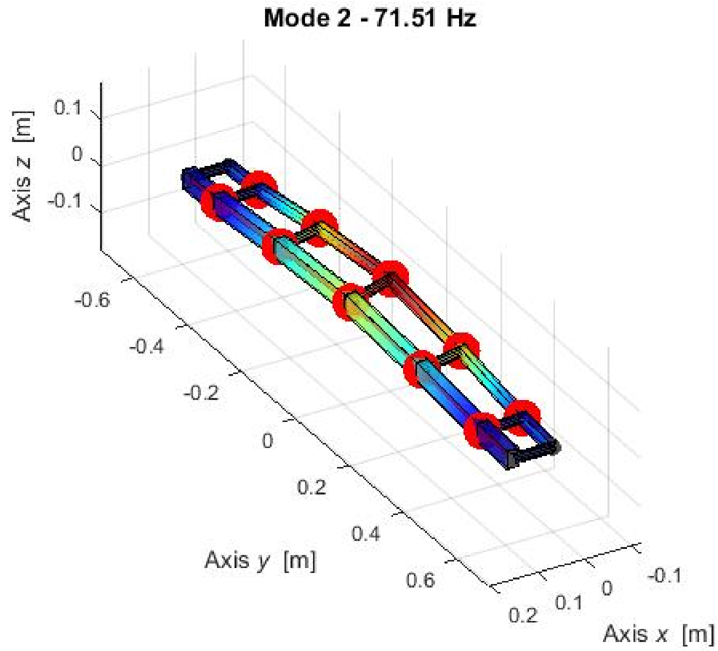

Figure 3.9: Modeshape 2.

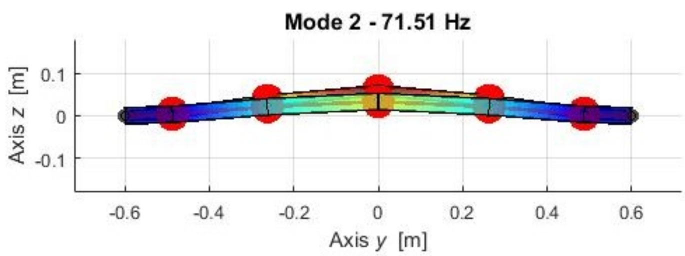

Figure 3.10: Front view, modeshape 2.

along the chord. By applying the drag and the lift in a different point from the centre of pressure, an aerodynamic moment arises and depends on the lift. Generally, is convenient to resort to the aerodynamic centre because the aerodynamic moment in this point does not change on the base of the lift. Therefore, the following forces are taken into account in the bi-dimensional model:

1. Lift force (L)
2. Pitching moment (M)
3. Drag force (D)

The formula of aerodynamic moment is represented by:

$$M = \frac{1}{2} C_M \rho U^2 s_p c^2 \tag{3.3}$$

In the case in point, the very low air speed allows to assume negligible the drag force. In fact the drag force becomes important only for large air-speed. In this static analysis only the pitching moment and the lift have been taken into account and theirs values have been computed by considering the Tables 3.3

Data	**Value**	**Units**
α	15°	$[-]$
C_L	1.3	$[-]$
C_M	0.05	$[-]$
ρ	1.225	$[kg/m^3]$
U	30	$[m/s]$
c	300	$[mm]$
s_p	1200	$[mm]$

Table 3.3: Values adopted to compute the lift and aerodynamic moment.

The coefficient of moment and the coefficient of lift can be obtained from experimental tables or graphs that are available on the websites. Generally to be conservative, an angle of 15° is taken into account and the maximum velocity of the air flow is considered about 30 m/s.

In aerodynamic it is possible to consider the following approximation: the air flow is incompressible if the Mach number is lower than 0.3. In this case the maximum air speed of the wind tunnel is about 20 m/s - 25 m/s and therefore this approximation is suitable for the study case. In a theoretical condition, for a flat plate in inviscid, subsonic and incompressible flow the aerodynamic centre is located at one quarter of the chord behind the leading edge of the plate. Even if the case in point presents a real airfoil with a certain thickness, the aerodynamic centre is considered at one quarter of the chord and it is fixed at that point. By using the formulae 3.1 and 3.3 and the data of the Tables 3.3 it is possible to compute the aerodynamic moment and the lift force.

Data	Value
L	$258.0\ [N]$
M	$3.0\ [Nm]$

Table 3.4: Values adopted to compute the lift and aerodynamic moment.

The previous computation led to get a single value of force and moment but, to have a quite good representation, the loads are divided along the wing span on the various nodes. By computing the reaction forces, the distributed loads are applied as shown in 3.11.

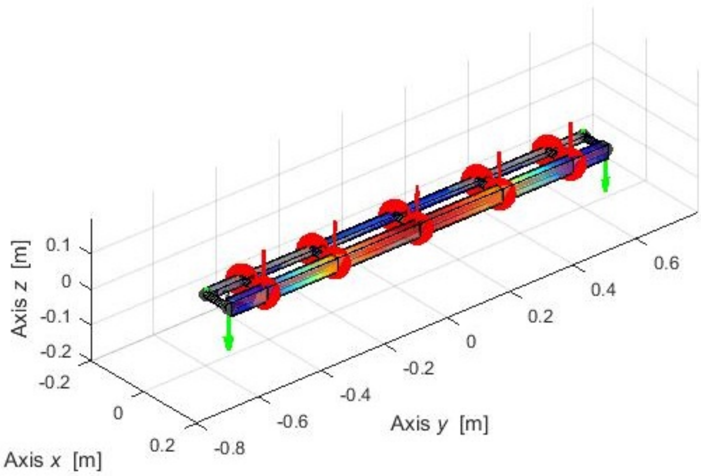

Figure 3.11: Static FEM model with applied loads.

Several tests are performed in order to find the correct dimensions of the two spars.

The Table 3.5 shows the different torsion angles and deflections of the central sector of the wing. The static analysis turned out to be the most restrictive part of the design; in fact in the modal analysis there have been no limitations. The results suggest to choose the sections of *case* 5 because the deflection and the torsion angle are both lower than the design limitations. This model is very simple and it has been used as very quick and rough design tool in order to find a suitable dimension of the profile sections. Since in the first model it has been very difficult to assume a correct value of the equivalent diameter of the ABS sector, a more accurate model is developed to verify the previous results. This model provides for having the ABS sector represented as a series of beams and it is shown in the Figures 3.12 and 3.13.

	Front spar	**Back spar**	**ABS**	**Angle**	**Deflection**
Case 1	$20 \times 20 \times 1\ mm$	$20 \times 20 \times 1\ mm$	$10\ mm$	$1.9°$	$3.1\ mm$
Case 2	$30 \times 30 \times 1\ mm$	$30 \times 30 \times 1\ mm$	$10\ mm$	$0.9°$	$1.2\ mm$
Case 3	$30 \times 20 \times 1\ mm$	$30 \times 20 \times 1\ mm$	$10\ mm$	$1.2°$	$1.5\ mm$
Case 4	$30 \times 20 \times 2\ mm$	$30 \times 20 \times 2\ mm$	$10\ mm$	$0.8°$	$1.0\ mm$
Case 5	$40 \times 25 \times 2\ mm$	$25 \times 15 \times 2\ mm$	$10\ mm$	$0.6°$	$0.5\ mm$
Case 6	$40 \times 25 \times 2\ mm$	$25 \times 15 \times 2\ mm$	$20\ mm$	$0.2°$	$0.3\ mm$

Table 3.5: Static torsion angles and deflections.

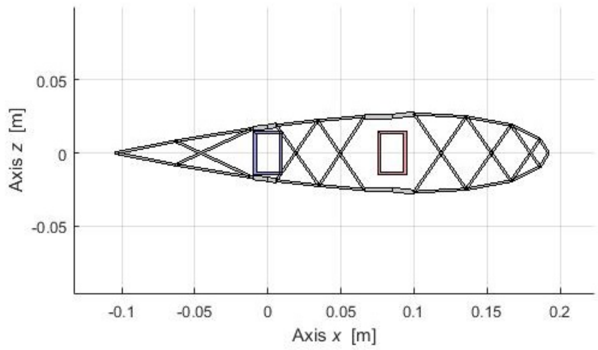

Figure 3.12: Accurate FEM model, lateral view.

The first mode and the second mode are represented by Figures 3.14(a) and 3.14(b). The modes are very similar to the modes of the simpler model but they are not exactly the same because the presence of the ABS sectors changes the dynamic behaviour of the system.

The previous static and dynamic results are checked now with the new FEM model and the most important results are provided in Table 3.6.

The new FEM model shows that the ABS sectors create a very strong connection between the two spars and the consequence is that the angle of torsion and the deflection in the centre of the wing is very small. The *case* 5 is verified and the wing can be considered stiff enough to avoid static deformation. Although a little

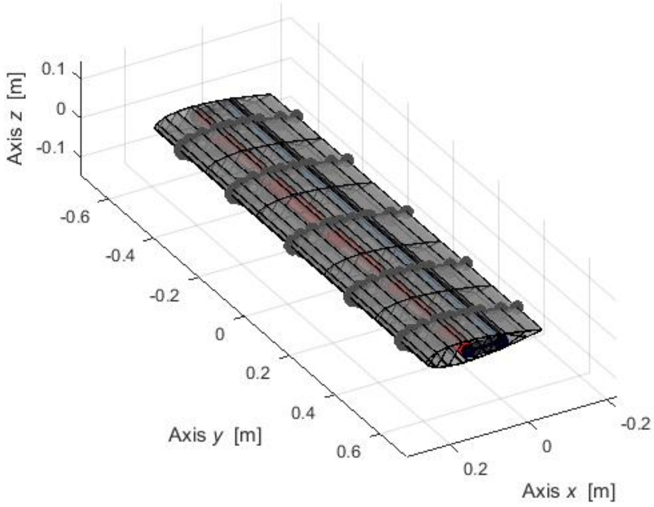

Figure 3.13: Accurate FEM model.

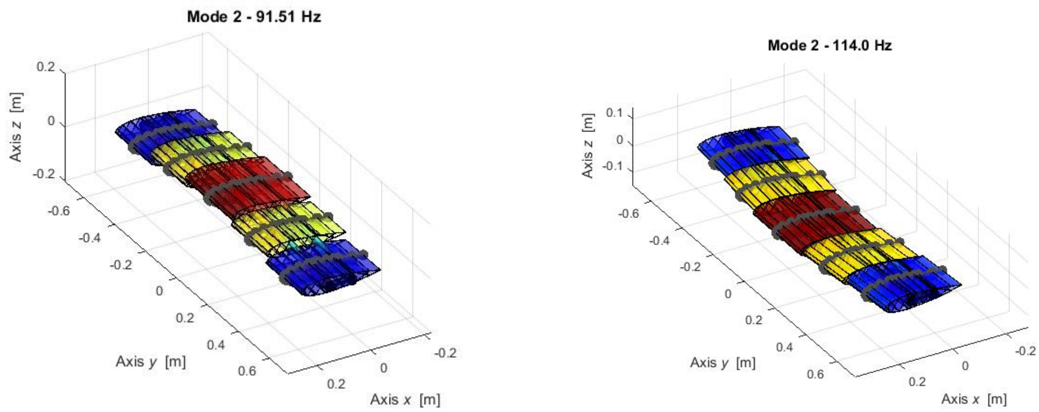

(a) First mode.

(b) Second mode.

Figure 3.14: Modeshapes of the accurate FEM model.

over-design is committed, there are many reasons that led to choose the dimension of *case* 5: firstly, all the design limitations are satisfied, secondly a little over-design helps to have the wing as stiff as possible, moreover the shape of the aerofoil forces to have two different sections of the spars because in the back of the aerofoil there is less space to allocate the motors and the wires, and finally the dimensions of *case* 5 are very common and easy to find in the web-market.

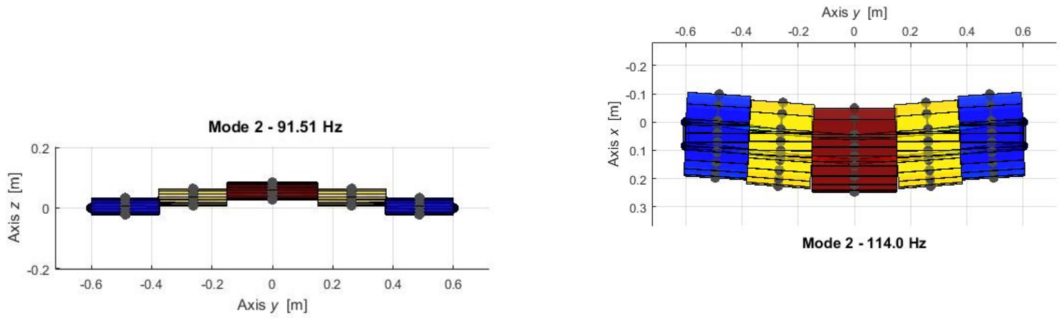

(a) Front view mode 1. (b) Top view mode 2.

Figure 3.15: Particular view of the modeshapes.

	1^{st} f_n	2^{nd} f_n	**Torsion angle**	**Deflection**
$Case$ 3	63.5 Hz	98.3 Hz	0.22°	0.9 mm
$Case$ 4	77.8 Hz	109.2 Hz	0.15°	0.5 mm
$Case$ 5	91.5 Hz	114.0 Hz	0.10°	0.3 mm

Table 3.6: Static torsion angles and deflections of accurate FEM model

3.2.4 CAD model

The FEM model allows to get the right dimension of the spars but it is also important an accurate CAD design in order to have the correct assembling and the correct definition of all the details, especially from the internal design. The most critical aspects from the practical point of view are:

- Frictions problems;
- Central sector assembling;
- Motors positioning;
- Wires passing;
- Extremities attaches.

First of all, the internal structure of each sector is re-designed with a particular frame represented in Figure 3.16. This particular design allows to have a lightweight and stiff sector. Moreover, it is easy to print this particular shape with the 3D printer because it is not requested a lot of support material.

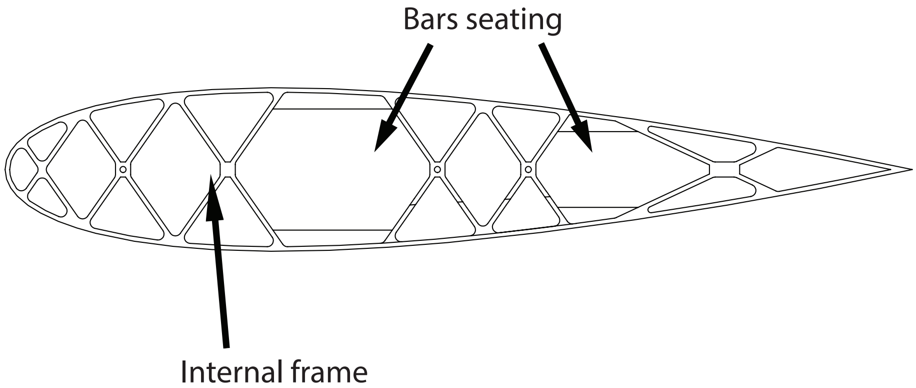

Figure 3.16: Internal frame representation.

The trailing- and leading-edge flaps are assembled in the active sector. In order to avoid the friction between the moving parts some material has been removed from the trailing-edge and from the leading-edge flap; this allows a much more simple assembling and post-treatment of the parts. The friction could cause the locking of the motors or the wrong zeroing of the flaps. The accurate sizing of the parts is required because the 3D printer tends to produces components with a large tolerance, therefore the actual dimensions could be different respect the CAD ones.

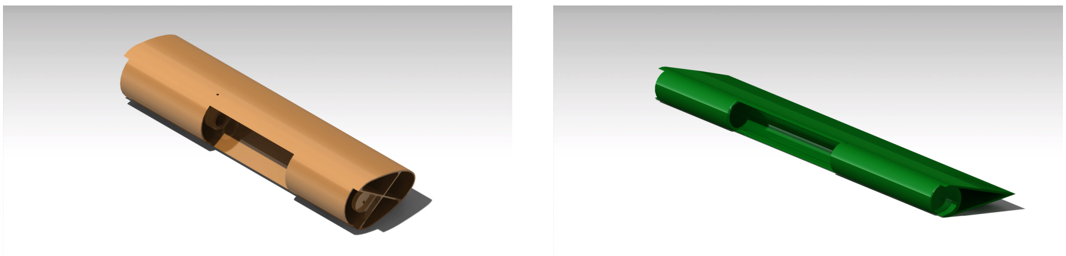

(a) Leading edge flap. (b) Trailing edge flap.

Figure 3.17: Trailing- and leading- edge flaps.

Two electrical motors control the moving of trailing- and leading-edge and they are fixed on the central sector by using the appropriate seating. Figure 3.19 represents how the motors are fixed on the sector and Figure 3.18 represents how the motors are connected to the flaps. The seating of the motors are reinforced by adding some material and modified to guarantee more space.

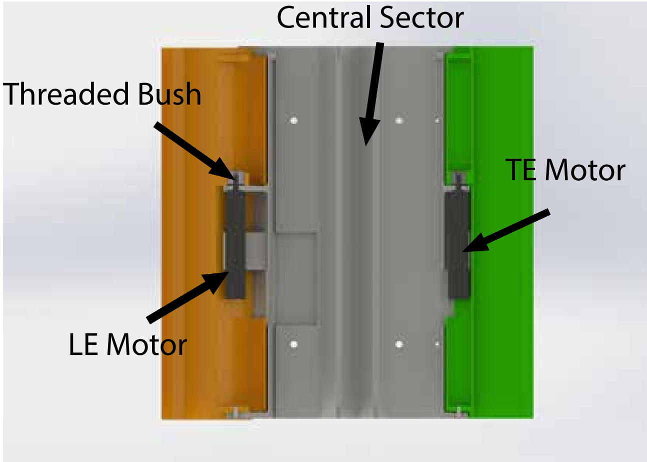

Figure 3.18: Description of the motors attaching.

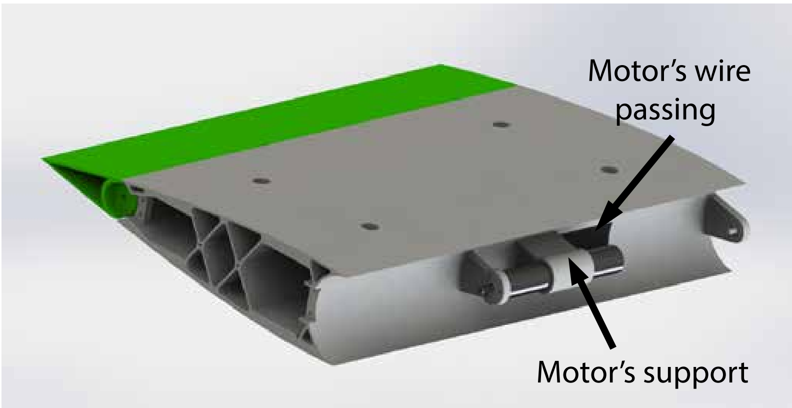

Figure 3.19: Leading edge motor's seating.

To guarantee a better assembling, the central sector is divided into two parts. This allows to change the motors or the moving edges very easily without dismounting all the wing from the support structure. This design aspect is very important because malfunctioning or detachment of the motor's wires happen very often during the assembling and the working phase.

The internal sectors are equipped with an indentation that allows the passing of the power wires from the external power source into the wing. Two connecting plates are designed in order to guarantee the correct linkage between the external structure and the wing. The plates provide for having a central hole for the passing of the wires and different threaded holes to allows the connection with the axis of the external structure. This axis represents the elastic axis of the aerofoil and therefore it plays a very important role in the system's aerodynamic. The plate has a lot of

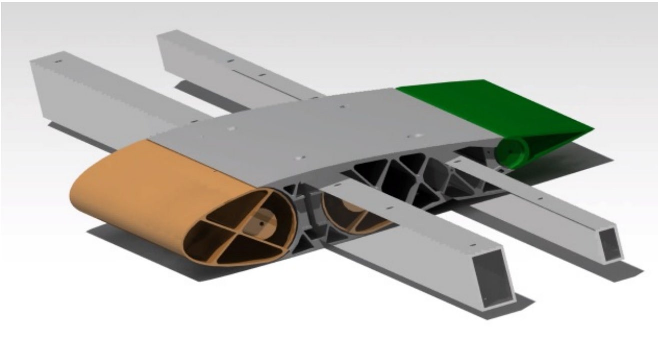

(a) Central sector.

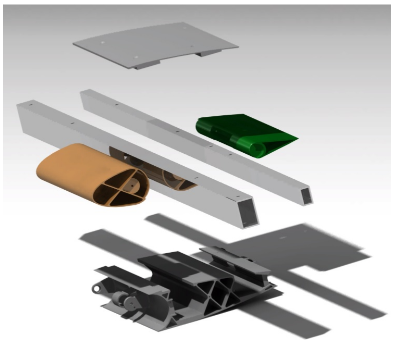

(b) Central sector exploded.

Figure 3.20: Central sector parts.

holes to have the possibility to change the position of elastic axis as shown in 3.21.

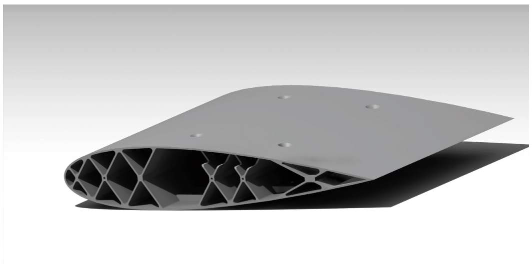

(a) External sector with indentation.

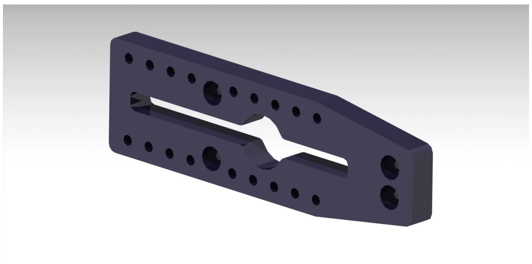

(b) Plate for wing attaching.

Figure 3.21: Plate and internal passive sector.

All the sectors are assembled and linked by using the two main spars and they are locked on the latter by using some screws. The cables of the encorders are located in their seating internally on the wing and they are plugged in the external computer in order to monitor the position of the flaps. The wing can be assembled by starting from the external sectors and the central sector can be located as last part. The final assembly of the wing is represented in the Figure 3.22. Two panels in PMMA are added on the extremities of the wing, as shown in Figure 3.23, in order to simulate an infinitely long wing; they reduce the boundary effects of the wing and they satisfy the hypotheses of the analytical model.

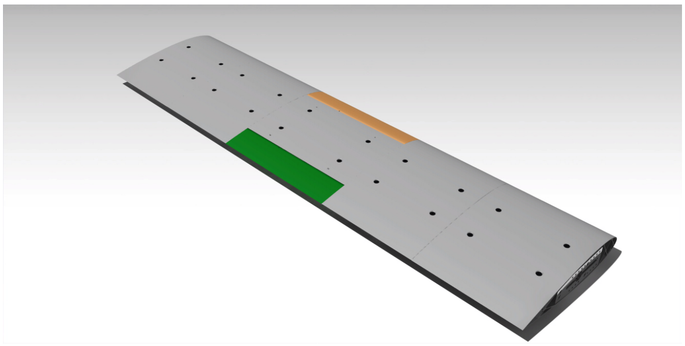

Figure 3.22: Total wing assembly.

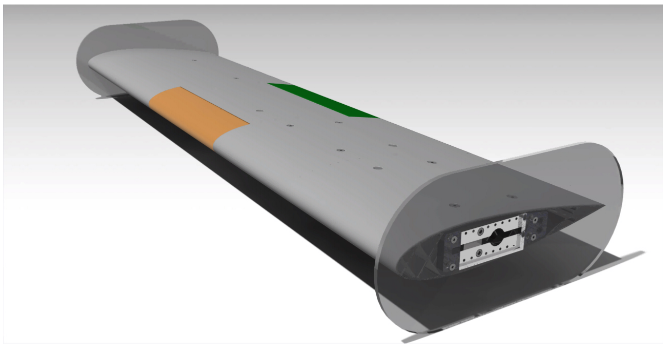

Figure 3.23: Complete wing assembly.

3.2.5 Real model

In this section the real structure and the assembling process are described. All the parts, described previously in the CAD model, are now assembled and the internal metallic structure appears as depicted in Figure 3.24(a). The first step provides for assembling the passive sectors with the internal structure as shown in Figure 3.24(b). It is not necessary to add before the central sector because the design allows to mount it as last part but the wires have to be passed in the sectors before the assembling of this part. It is possible to add the lower part of the central sector with the flaps by inserting it from the bottom of the model as shown in Figure 3.25 and the top cover will be applied in a second time to close the active sector. To have all the wires in the same position, the cables of the leading-edge flap have to pass over the front bar as shown in Figure 3.26 and they will come out from the model to be plugged in the external computer. Once the model is completely assembled, it can be mounted on the support structure to complete the assembling process.

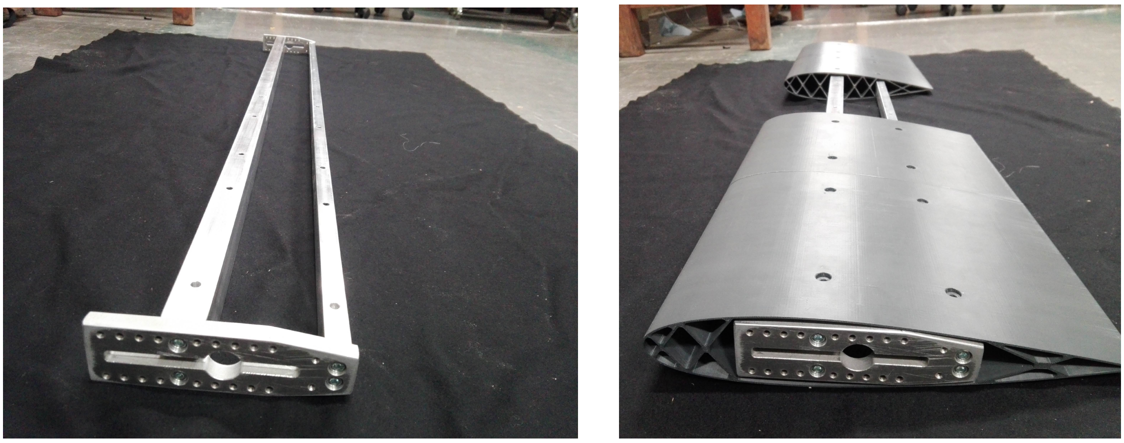

(a) Internal aluminium structure. (b) Internal structure and passive sectors.

Figure 3.24: Model assembling.

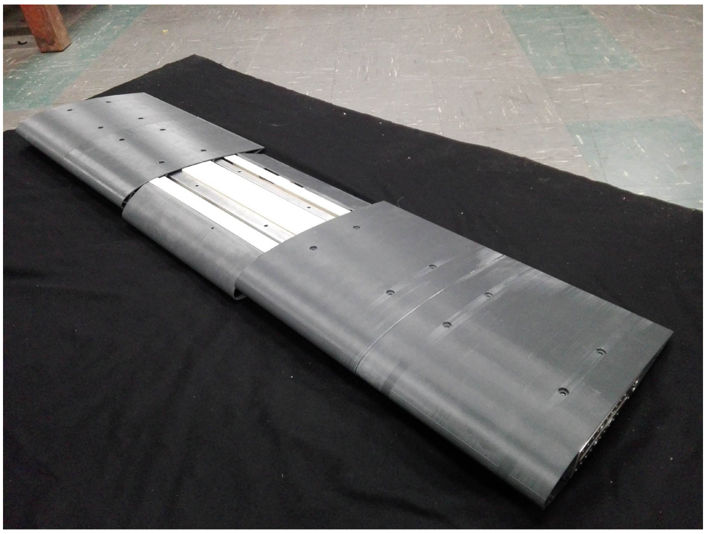

Figure 3.25: Wing model: addition of the central sector from the bottom.

Figure 3.26: Detail about the wires passing inside the model.

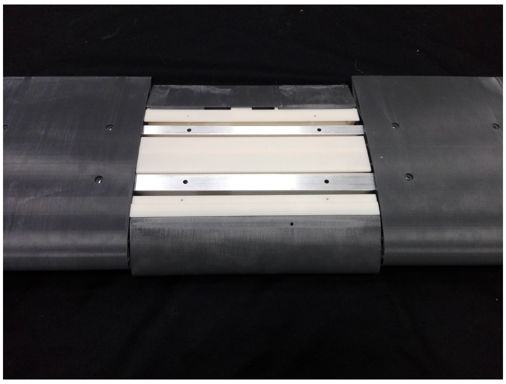

(a) Detail: the central sector can be added from the bottom of the structure.

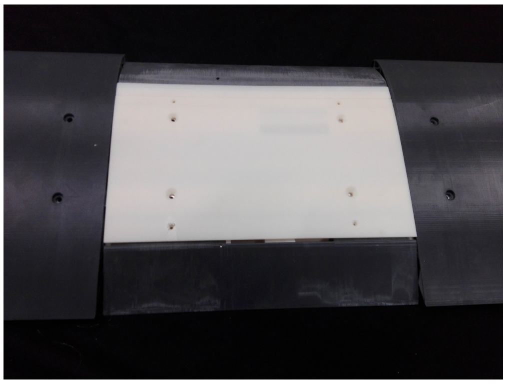

(b) Detail: the central sector is closed by adding the top cover.

Figure 3.27: Central sector details.

Chapter 4

Experimental Setup

A series of tests were performed on the experimental rig to find the correct model setup. All the tests are performed in the wind tunnel of the University of Liverpool which is able to generate a maximum wind-speed of 18 - 20 m/s, therefore a correct setup of the experimental model is mandatory to see the onset of flutter before the maximum wind-speed. The experimental test were performed by using two important tools:

- LMS: an analog-to-digital converter;
- dSPACE: a real time controller.

The LMS was used to compute all the FRFs while the dSPACE is able to make real time computing therefore it was used to apply the control law to the flaps and to read the encoder positions.

4.1 Experimental data

The external structure allows to control the dynamic of the system by changing the stiffness of the springs and the position of the external masses. In this way, it is possible to obtain different flutter-speeds. The results are shown in the Tables 4.1, 4.2 and 4.3 where some different configurations are investigated. Although the stiffnesses were not numerically measured it is possible to understand the trend of the flutter onset by considering that:

- the stiffness of the spring is inversely proportional to the free length of the correspondent plate;
- the moment of inertia of the wing is proportional to the distance between the external masses and the elastic axis which is increased in the direction of the wing tail.

The support structure allows to change the stiffness of the pitch spring and the plunge spring by changing the attaching position of the plates. The Figures 4.1 and 4.2 show the springs in details.

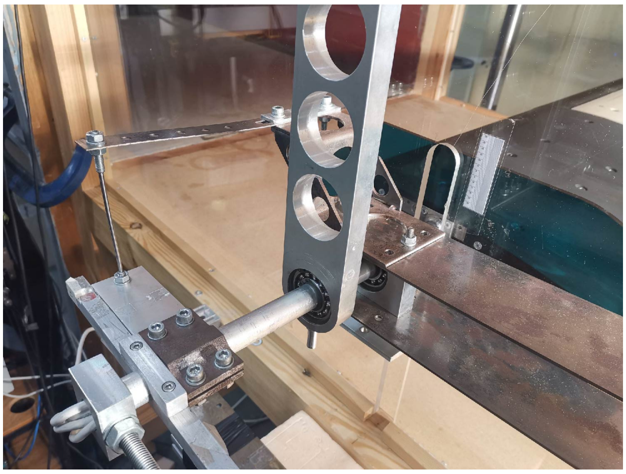

Figure 4.1: Pitch spring: the regulation of the stiffness can be done by changing the position of the stinger.

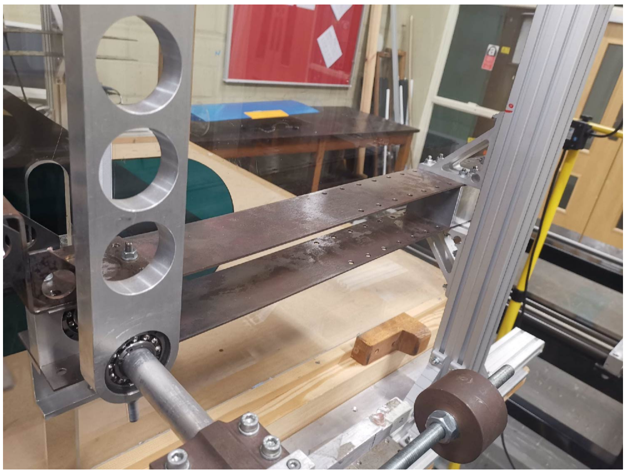

Figure 4.2: Plunge spring, the stiffness can be regulated by changing the position of the perforated plates.

The two natural frequencies of the pitch and plunge mode are described by the following formulae:

$$\omega_h = \sqrt{\frac{k_h}{m_T}} \qquad \omega_\alpha = \sqrt{\frac{k_\alpha}{I_\alpha}} \tag{4.1}$$

From the Tables 4.1 and 4.2 is possible to notice that by increasing the plunge frequency and by decreasing the pitch frequency the required amount of wind to reach the flutter conditions is lowering. This fact comes from the physical definition of flutter and it confirms experimentally the flutter condition as the coalescence of the two structural modes. In the Tables 4.1, 4.2 and 4.3 just a parameter at time is changed in order to see the effects on the structure and, for the sake of simplicity, the three different stiffnesses are tested and they are named: soft, medium and stiff.

Parameter	**test 1**	**test 2**	**test 3**
$Mass\ position$	10 mm	10 mm	10 mm
$Plunge\ stiffness$	soft	soft	soft
$Pitch\ stiffness$	soft	medium	stiff
$Flutter - speed$ [m/s]	9.6	13.2	> 18

Table 4.1: Flutter-speed vs pitch stiffness, the position of the masses indicates the distance between the external masses and the elastic axis in the direction of the tail.

Parameter	**test 1**	**test 2**	**test 3**
$Mass\ position$	6 mm	6 mm	6 mm
$Plunge\ stiffness$	soft	medium	stiff
$Pitch\ stiffness$	medium	medium	medium
$Flutter - speed$ [m/s]	14.5	12.4	9.3

Table 4.2: Flutter-speed vs plunge stiffness, the position of the masses indicates the distance between the external masses and the elastic axis in the direction of the tail.

From the experimental tables is possible to understand that the hypotheses made in theory are true, in fact:

1. By reducing the stiffness in pitch the flutter occurs before;
2. By increasing the stiffness in plunge the flutter takes place before;
3. By increasing the moment of inertia the flutter occurs before.

Parameter	**test 1**	**test 2**	**test 3**	**test 4**	**test 5**
$Mass\ position$	no mass	6 mm	10 mm	15 mm	19.5 mm
$Plunge\ stiffness$	soft	soft	soft	soft	soft
$Pitch\ stiffness$	medium	medium	medium	medium	medium
$Flutter - speed$ [m/s]	16.6	14.5	13.4	11.1	9.5

Table 4.3: Flutter-speed vs external mass position, the position of the masses indicates the distance between the external masses and the elastic axis in the direction of the tail.

The analytical model confirms the trends of the experimental results because by increasing the pitch stiffness there is an increase of flutter-speed while by increasing the plunge stiffness the flutter-speed appears before. With the final configuration, the flutter appears at 15.6 m/s.

4.2 Gains setting for PID control

This section describes the experimental method to find the gains of the PID controller. The PID controller and the control architecture will be discussed in detail in *Chapter 6*. To find the correct gains of the PID controller, the empirical method of Ziegler-Nichols is used. This theory is based on the oscillation period of the unstable system which is possible to get by using only the proportional gain K_p. The proportional gain is increased up to the value for which the system becomes unstable and the oscillation period can be read by the motor's encoder. The K_p gain is directly obtained from the Equation 4.2.

$$K_p = 0.6K_u \tag{4.2}$$

Where K_u represents the unstable proportional gain. The measured period of unstable oscillation allows to get two periods related respectively to K_d and K_i as shown in Equation 4.3.

$$\begin{aligned} T_d &= \frac{T_u}{8} \\ T_i &= \frac{T_u}{2} \end{aligned} \tag{4.3}$$

Finally it is possible to get the integral and derivative gains by using the following relations:

$$K_d = T_d K_p$$
$$K_i = \frac{K_p}{T_i} \tag{4.4}$$

The initial data used to compute the gains are listed in Table 4.4. The method allows to get some preliminary gains, listed in Table 4.5, but actually they are not perfect for the requested application therefore it is necessary to adjust them manually. The gains are modified experimentally in order to find a very quick system response.

Gain	**Trailing-edge**	**Leading-edge**
T_u	0.035	0.024
K_u	2.5	2
T_i	0.0175	0.012
T_d	0.004375	0.003

Table 4.4: Experimental data obtained for Ziegler-Nichols method.

Gain	**Trailing-edge**	**Leading-edge**
K_p	1.5	1.2
K_d	0.0065625	0.0036
K_i	85.7	100

Table 4.5: Preliminary gains obtained from Ziegler-Nichols method.

The final gains are listed in Table 4.6. The values have been change but the difference in terms of magnitude order has been kept the same, in fact the gains must have different order of magnitude to allow the correct functioning of the PID control.

Gain	Trailing-edge	Leading-edge
K_p	3	3
K_d	0.02	0.035
K_i	60	45

Table 4.6: Modified experimental gains.

The manual correction of the gains is performed by taking into account the transitory condition which is obtained by giving a step signal to the flap. In fact, with a step signal is possible to understand how much the PID control is reactive and how much quickly it reaches the final requested condition. The gains are chosen in order to get a very quick response because it is necessary that the controlled surfaces are able to follows a sine signal at high frequency. The requested range of frequency corresponds to the exciting one which is between 1 Hz and 7 Hz. In fact, the pitch and plunge peaks are positioned in that range of frequency. The Figures 4.4 and 4.3 show the experimental response given by the encoders of the flaps when a step signal is applied.

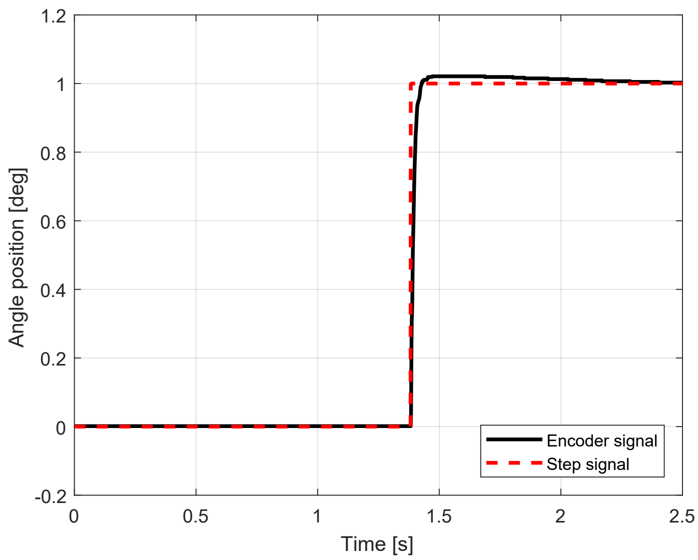

Figure 4.3: Leading-edge flap signal with step input.

It is possible to notice that the response is very quick because the gain K_p is

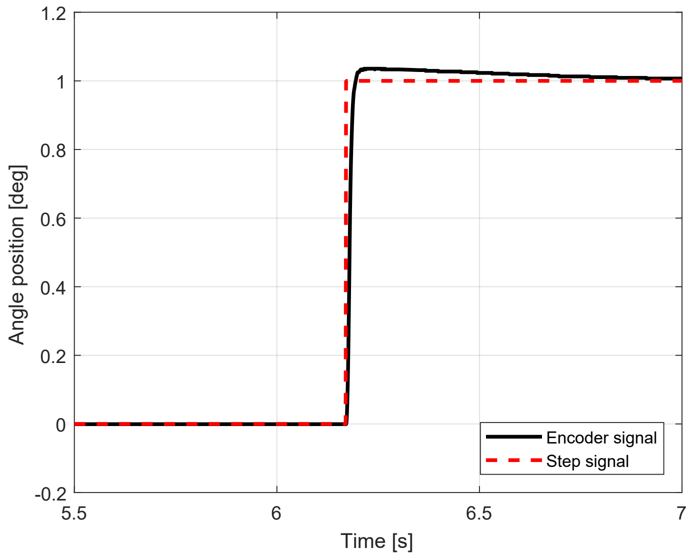

Figure 4.4: Trailing-edge flap signal with step input.

high and there are no oscillations at the end of the step signal because the gain K_d is large enough. The gain K_i intervenes at the end of the signal when the controlled surface has to reach gradually the final value of 1°. The Figures 4.5 and 4.6 show the behaviour of the PID control in steady condition with a sine input signal.

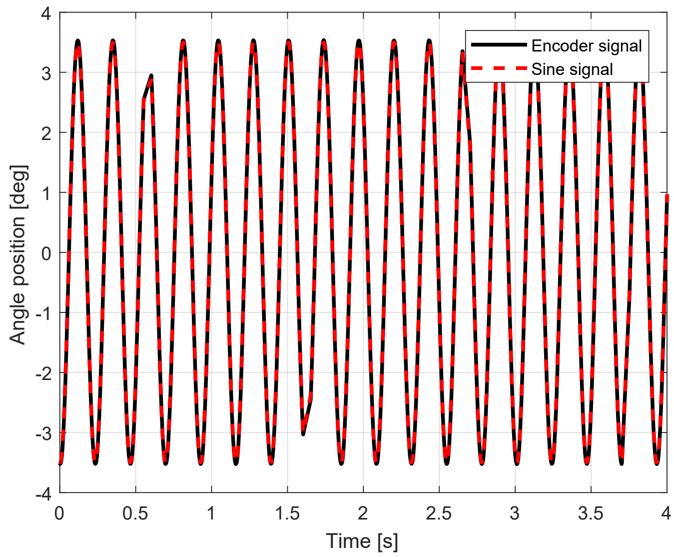

Figure 4.5: Leading-edge flap signal for a sine signal of 4.3 Hz.

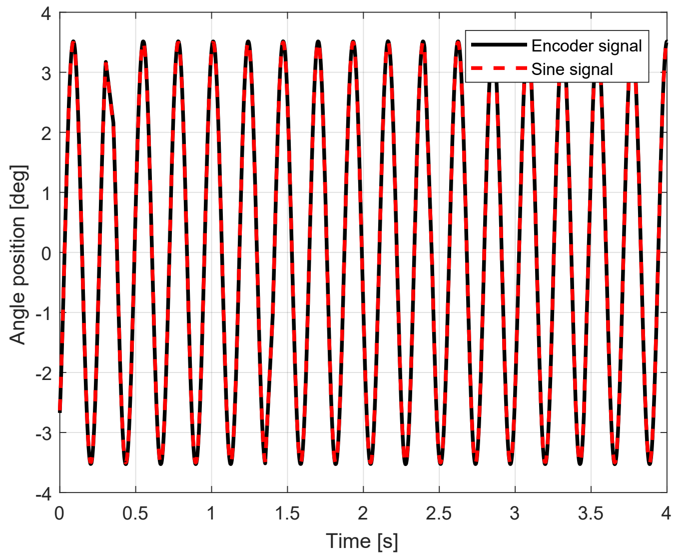

Figure 4.6: Trailing-edge flap signal for a sine signal of 4.3 Hz.

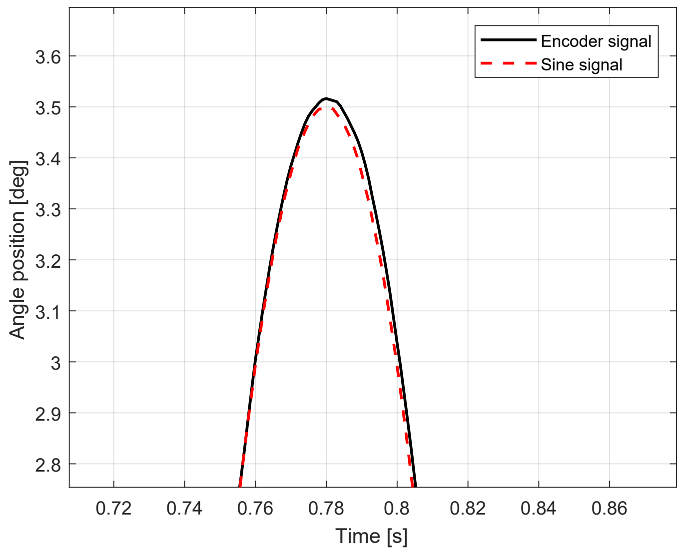

Figure 4.7: Detail of leading-edge flap signal: inversion of signal at 4.3 Hz.

The control is able to follow in very good way the input signal also at large frequencies, therefore the final gains are suitable for the requested application. The Figure 4.7 shows the discrepancy between the input signal and the encoder signal when there is an inversion of direction in the sine input but also in this case the difference between the two signals is very tiny. The gains K_p, K_d and K_i have to work together with the same effort in order to avoid an excessive use of a single gain.

4.3 Frequency response function

The frequency response of the complete system is studied by making a series of experimental tests. The analog to digital converter LMS is used to acquire the FRFs of the system. In particular, the following tests have been performed:

- frequency response function obtained through excitation with impact hammer;
- frequency response function obtained through excitation with shaker;
- frequency response function obtained through excitation with flaps.

The first test is used just to see the position of the first two natural frequencies of the assembled structure, i.e. pitch and plunge modes. The FRFs obtained through the shaker are necessary to properly identify the model's parameter and then to proceed with model updating. The third tests are used to apply the receptance method from an experimental point of view. In latter case, it is necessary to identify the state space matrices $\mathbf{A_{ss}}$, $\mathbf{B_{ss}}$, $\mathbf{C_{ss}}$ and $\mathbf{D_{ss}}$ of the system in order to apply the receptance method and to place the poles in the desired location.

4.3.1 Impact hammer test

An impact test is performed by placing different accelerometers on the wing. This test is just a preliminary test to see where are placed all the peaks in the FRFs. It is important to have a certain distance in terms of frequencies between the first peak and the second peak in order to have a good fitting during the phase of model updating. Therefore, the final system configuration must have a distance at least of 1-2 Hz between the pitch and plunge resonance frequencies and it must show the flutter onset within the maximum wind-speed of the tunnel. The two natural frequencies are:

- $\omega_{plunge} = 3.935$ Hz
- $\omega_{pitch} = 5.727$ Hz

As the results show the final configuration is suitable for the study purposes because the flutter-speed measured experimentally appears at 15.6 m/s - 15.7 m/s and the peaks are sufficiently separated in terms of frequency. In this final configuration, the position of the elastic axis was changed by changing the position on the attaching plate as described in the *Chapter 3*. The final elastic axis position is 132 mm from the leading edge tip by using the CAD dimensions.

4.3.2 Shaker test

The shaker test is performed by positioning the shaker under the wing as shown in the Figure 4.9 and by exciting the wing only in the plunge direction. Since the centre of mass is not positioned along the elastic axis, it is possible to excite the structure also in pitch motion. The shaker tests are performed with and without wind: the first tests are necessary to update the model while the second ones allow to know the internal dynamic of the structure at different wind-speed. All the tests are performed with a frequency increment of 0.05 Hz and with 20 cycles at each frequency step.

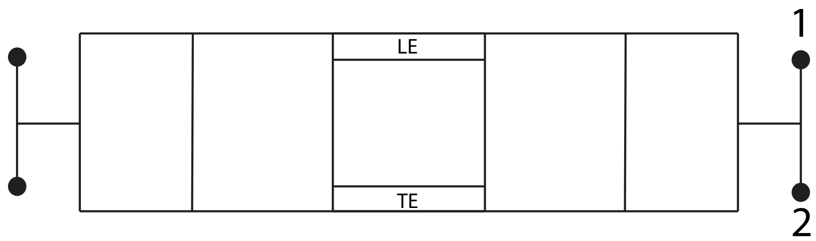

Figure 4.8: Laser reading points on the structure.

Two high precision lasers are used to read the position of the wing in two different point as illustrated by Figure 4.8, they are able to see the displacements of the wing in the point 1 and 2 but not to measure directly the pitch and plunge displacements. The point 1 is the measuring point of front laser while the point 2 is the measuring point of the back laser. The Figure 4.10 shows the lasers and the reading point on the structure.

The FRFs obtained are representative of the outputs given by the two lasers, i.e. front laser and back laser. It is possible to get the pitch and plunge displacements through a linear combination of the outputs given by the two lasers as described by the Equations 4.5. In the same way, it is possible to get the pitch and plunge FRFs from a linear combination of laser FRFs :

$$\begin{aligned} h &= y_2 + (y_1 - y_2)\frac{d_1}{d_1 + d_2} \\ \alpha &= arctan\left(\frac{y_1 - y2}{d_1 + d_2}\right) \end{aligned} \tag{4.5}$$

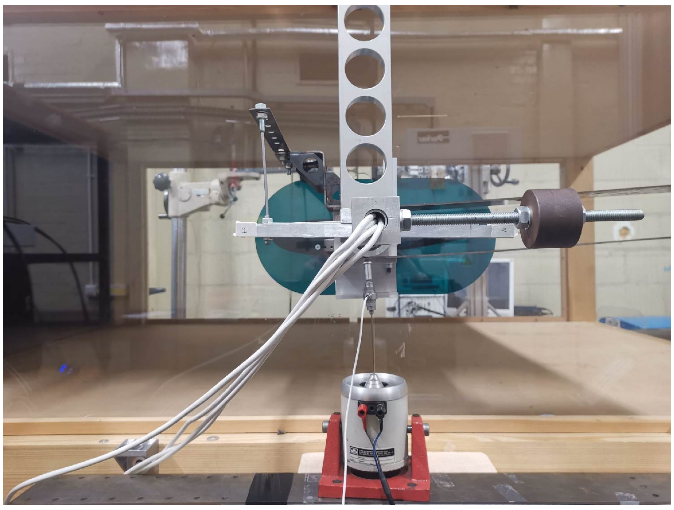

Figure 4.9: Shaker position on the model, the excitation is given along the plunge direction.

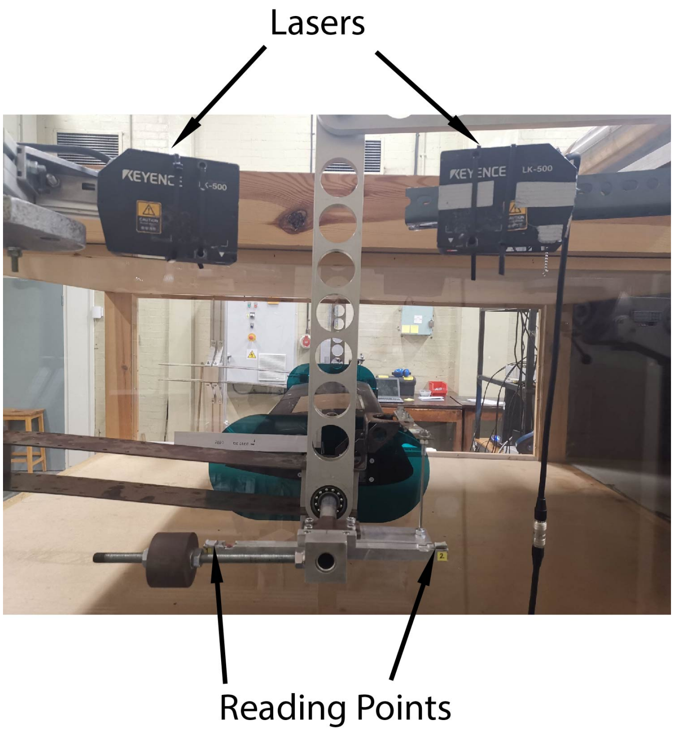

Figure 4.10: High precision lasers, the measuring points are placed on the external structure.

Where:

- y_1 and y_2 are the displacements respectively of laser front and laser back;
- d_1 and d_2 are the distances between the measuring points of the front laser and of the laser back from the elastic axis.

The FRFs referred to pitch and plunge displacements will be used in the *Chapter* 5 to perform the model updating. In order to be aligned with the analytical FRFs given from the mathematical model, it is necessary to transform them into FRFs related to pitch and plunge displacements. The new FRFs are represented in Figures 4.11 and 4.12. The shaker test is repeated again with the wind on in the same manner and different FRFs are computed for different wind-speed, in particular for:

- 3 m/s;
- 6 m/s;
- 9 m/s;
- 12.2 m/s;
- 14 m/s.

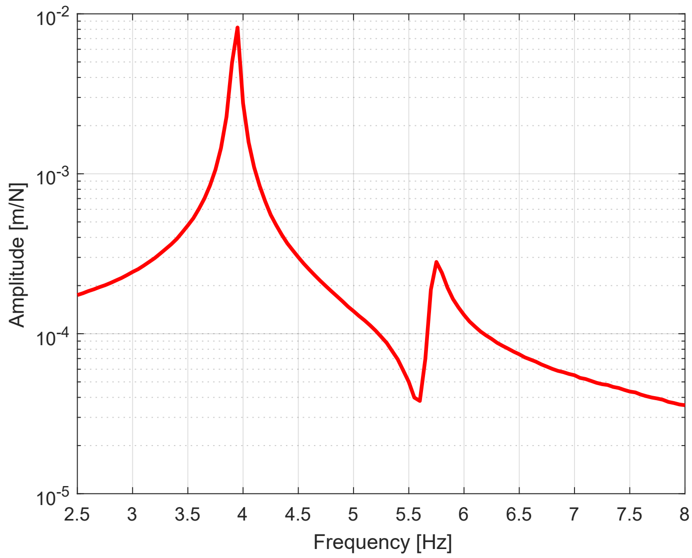

Figure 4.11: FRF with plunge displacement output without wind.

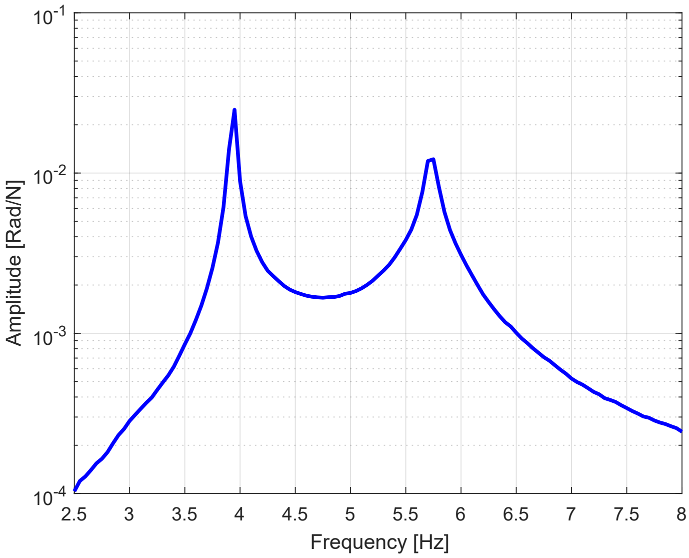

Figure 4.12: FRF with pitch angle output without wind.

The FRFs with wind on of Figures 4.13 and 4.14 show that the peaks tend to becomes as closer as the wind increases. At the end of this process, the two peaks coalesces into a single very large peak that leads to the flutter instability. It is possible to notice that as much the wind-speed increases as much the noise raises. This phenomenon is normal because the aerodynamic conditions make more difficult to have a smooth FRF and the electric motor of the wind tunnel is not perfectly stable at every wind-speed, therefore the wind-speed oscillates around the required speed. It is interesting to see the trend of FRFs on the same plane as a function of wind-speed as shown in Figure 4.13 and 4.14.

The increase in damping for both the modes and the coalescence of modes is evident. It is not possible to compute FRFs beyond 14 m/s because the damping from that point on wards tends to zero very quickly, in fact at 15.6 m/s the flutter occurs. The curves plotted in Figures 4.13 and 4.14 are defined as synthesized, i.e. they are obtained from the post-processing of the data in the analog-to-digital converter program. The poles are obtained from the application of the stabilization diagram which implements the PolyMAX technique, a very common procedure to identify the model parameters from FRFs. Since the poles are known, it is possible to eliminate the noise from the FRFs by fitting the FRFs with a synthesized one. The stabilization diagram used in the computation of poles is represented in the 4.15. By using this technique, it is possible to extract all poles related to the different computed FRFs that will be used in the model updating.

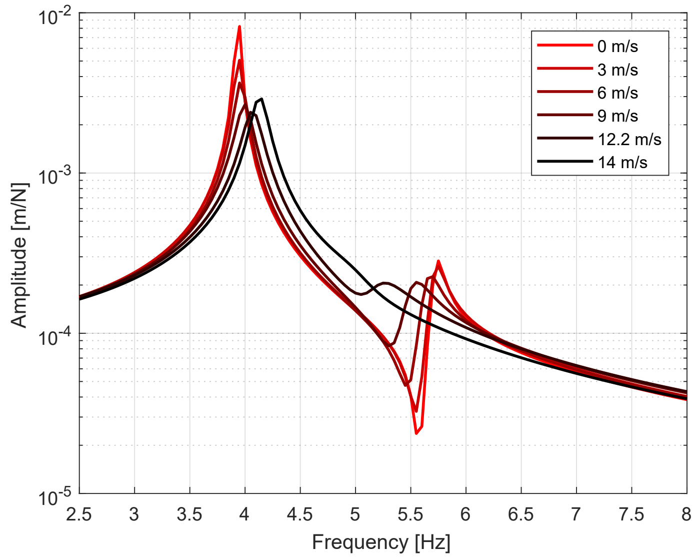

Figure 4.13: Trend of the plunge FRFs, the growth of color towards dark indicates FRF computed at larger wind-speed.

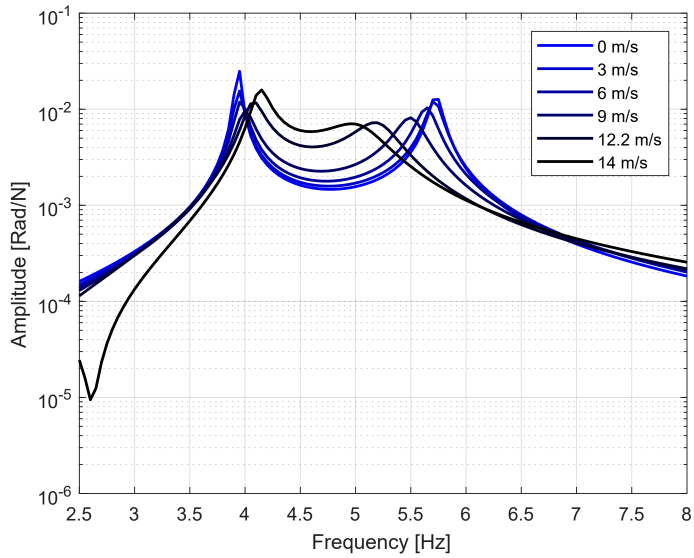

Figure 4.14: Trend of the pitch FRFs, the growth of color towards dark indicates FRF computed at larger wind-speed.

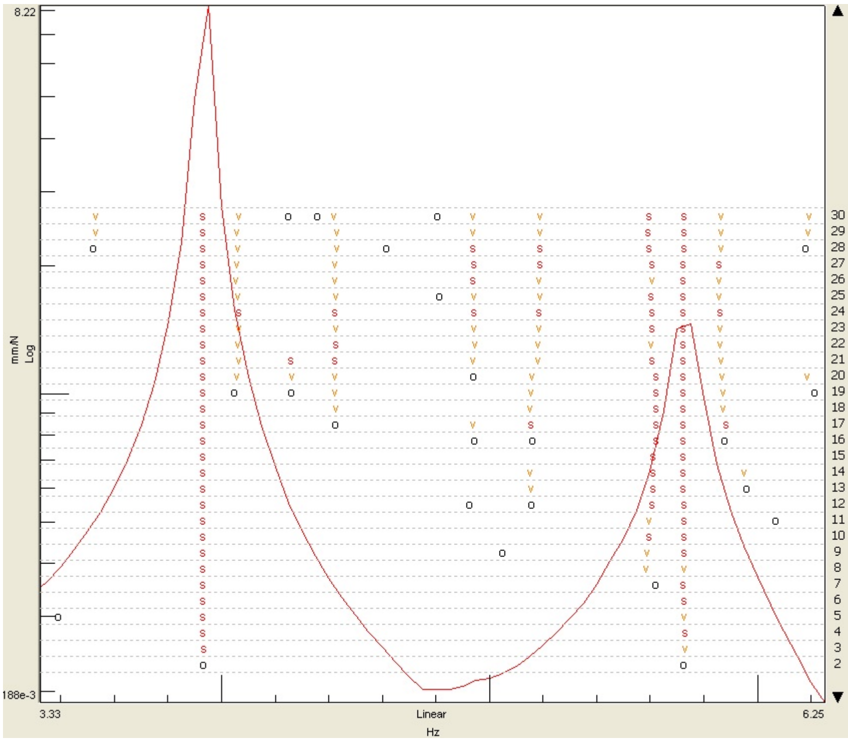

Figure 4.15: Stabilization diagram of LMS program.

4.3.3 Flap excitation test

A series of FRFs are now computed by exciting the structure through the flaps. The flaps are actuated one at time therefore the first FRFs are computed by using just the leading-edge flap while the second ones are obtained by exciting the structure with just the trailing-edge flap. This operation is necessary to obtain a set of four different FRFs which are necessary to create a sort of transfer function matrix used in the identification of a MIMO system. From the set of FRFs, it is possible to identify the corresponding state space system by using a toolbox implemented in MATLAB: SDtools. This software allows to identify the matrices $\mathbf{A_{ss}}$, $\mathbf{B_{ss}}$, $\mathbf{C_{ss}}$ and $\mathbf{D_{ss}}$ which describe the MIMO system for the chosen wind-speed. Since the system is composed by two inputs and two outputs, respectively: the flap angles and the laser displacements, the dynamic matrix $\mathbf{A_{ss}}$ has to belong to $\mathcal{R}^{4\times4}$ and the matrix $\mathbf{D_{ss}}$ has to belong to $\mathcal{R}^{2\times2}$. The direct link matrix has to be a null rectangular matrix because there are no feedback-through. As consequence the corresponding transfer function from the flap angles to the laser displacements belongs to $\mathcal{R}^{2\times2}$. The state space matrices will be used in *Chapter* 6 to control the structure through the application of the receptance method, therefore there is no need to transform them into FRFs of pitch and plunge.

All the FRFs are performed with a frequency increment of 0.02 Hz and with 20 cycles at each frequency step. The curves are obviously more noisy because the structure is excited by the flaps whose effect is related to the wind-speed; in fact, far away from the natural frequencies, the structure does not move a lot and the FRFs become noisier. It is also necessary to avoid excessive wind-speed in order to be not too close to the flutter-speed. The wind-speed adopted is 12.8 m/s because:

- the flaps have a good control authority;
- the wind-speed of the tunnel is particularly stable.

Once the $\mathbf{A_{ss}}$, $\mathbf{B_{ss}}$, $\mathbf{C_{ss}}$ and $\mathbf{D_{ss}}$ are known, it is possible to recreate the transfer function from these matrices and it is possible to see if there is a good fitting. The transfer function is obtained from the state space matrices by using the following equation:

$$\mathbf{R}(\mathbf{s}) = \mathbf{C_{ss}}(\mathbf{I_{ss}}(\mathbf{s}) - \mathbf{A_{ss}})^{-1}\mathbf{B_{ss}} + \mathbf{D_{ss}} \tag{4.6}$$

The Figure 4.16 shows the fitting between the experimental FRFs and the FRFs computed from the matrices :

4.4 Stiffness identification

The last experimental test consists into the stiffnesses identification. This test is carried out in a very basic way by applying some weights on the structure and by reading the pitch and plunge displacements. The test is made by using the laser in high precision mode, therefore the results are quite accurate. By using different measurements it is possible to perform a simple linear regression through which the slope of the fitted line is obtained. The slope corresponds to the stiffness of the spring in point. The Figure 4.17 shows the interpolated data. The application of the loads is obtained by applying some weights directly on the structure in pitch and plunge direction, as described in Figure 4.18.

The stiffnesses obtained from this computation are:

- plunge stiffness: $K_h = 8650 \, \dfrac{N}{m}$
- pitch stiffness: $K_\alpha = 70 \, \dfrac{Nm}{m}$

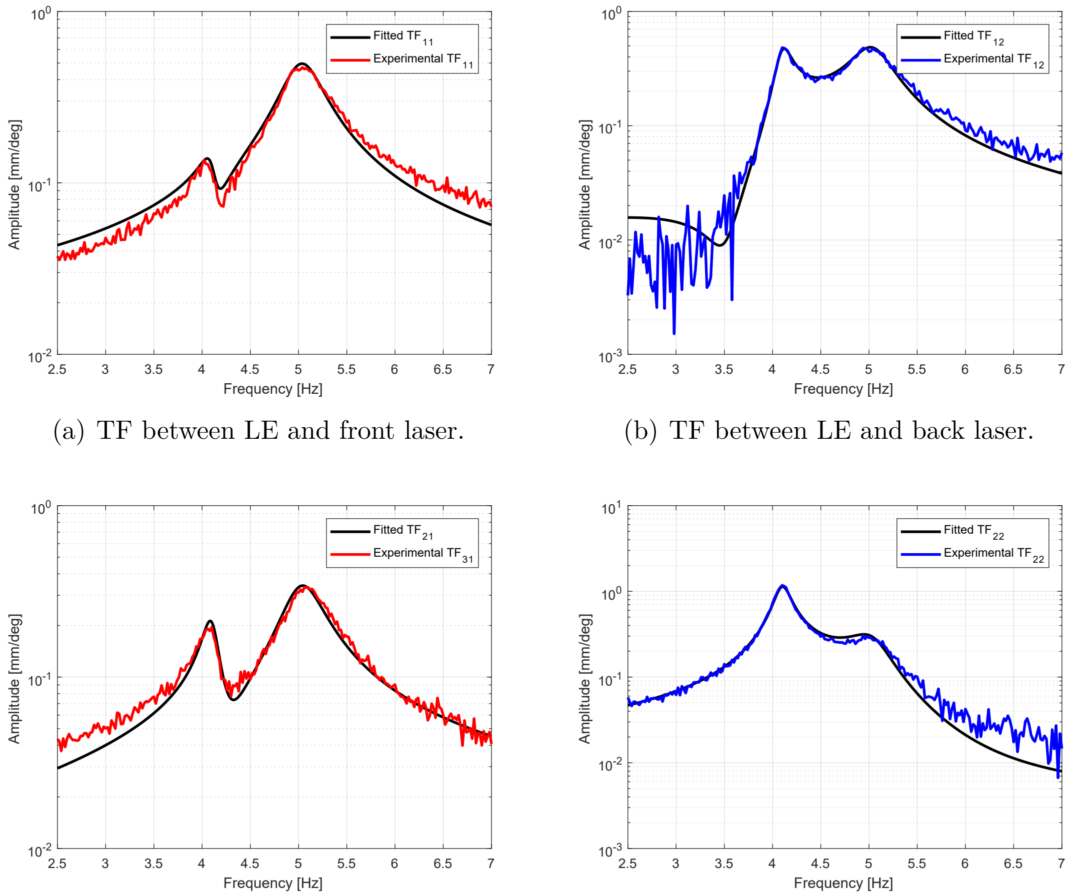

(a) TF between LE and front laser.

(b) TF between LE and back laser.

(c) TF between TE and front laser.

(d) TF between TE and back laser.

Figure 4.16: FRFs fitting at 12.8 m/s: the red and blue FRFs represent the computed transfer functions respectively in front and back lasers output while the black ones represent the fitted FRFs obtained from the four state space matrices. Since the state space matrices were processed through a fitting procedure, there is no noise in the black FRFs.

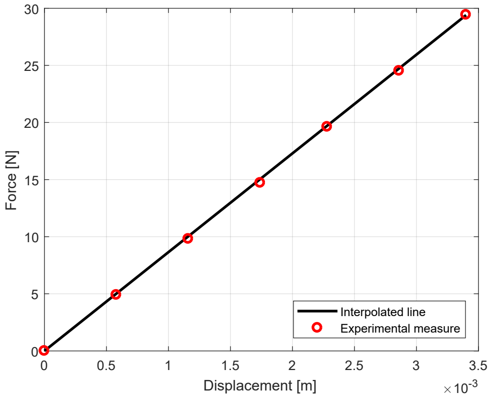

(a) Plunge stiffness identification.

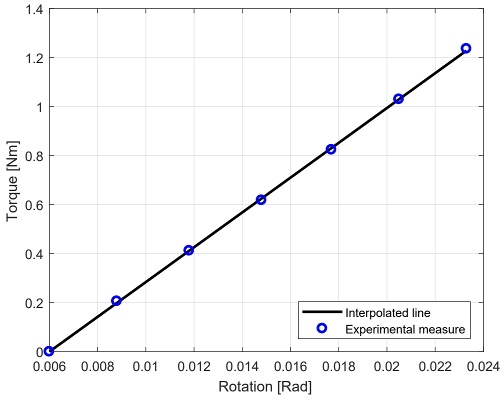

(b) Pitch stiffness identification.

Figure 4.17: Stiffness identification: the figure shows the linear regression adopted and the points represent the experimental results.

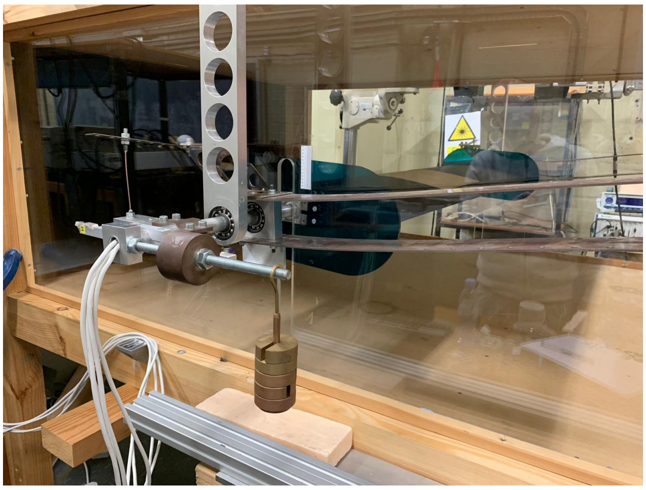

Figure 4.18: Application of the weights for the pitch stiffness computation.

Chapter 5

Model Updating

In this chapter the model updating is taken into account and it is performed by starting from the experimental data described in *Chapter 4*. In particular the FRFs obtained with the shaker are now used to extract the model's parameters. The model updating consists into finding the correct parameters which are able to guarantee a good fitting between the experimental data and the analytical ones. In particular, the experimental FRFs at zero wind-speed is used to perform this step. Theoretically, it could be possible to update manually the structure by changing one parameters at time, but since there are a lot of parameters and a lot of possible combinations, it is better to resort to an optimizer function implemented in MATLAB : LSQNONLIN. This function is able to compare the analytical FRF with respect the experimental one and it tries to minimize the difference between this two function.

5.1 Optimizer

The optimizer function LSQNONLIN is able to solve non-linear least square problem and to apply the data fitting. Basically, the optimizer tries to minimize the provided function which is named *fun*. In fact the MATLAB syntax of LQSNONLIN is:

$$x = lsqnonlin(fun, x_0, l_b, u_b, options) \tag{5.1}$$

Where:

- *fun* is the function which has to be minimized;
- x_0 is the column vector with the function variables which can be modified from the optimizer;
- l_b and u_b are the vectors which represent the upper and lower boundary values for the optimized parameters;

- *options* represents the options used in the computation.

In the case in point, the function *fun* has to be the difference between the analytical FRFs and the experimental FRFs computed with pitch and plunge outputs. This function has to be minimized to find a good fitting between the two set of FRFs. Although this optimizer is very efficient, it is possible that the results are not physically representative for the system because the function can find the solution when there is a local minimum, i.e. when the function *fun* reaches a minimum point. This means that the fitting is probably very good but the found parameters are just numbers and not real physical parameters. In order to avoid this problem it is necessary to have the initial data as close as possible to the real ones and the number of updated parameters has to be reduced as much as possible. It is possible to check if the final results are representative of a local minimum by changing the initial data of a small percentage: if the final results are always the same, the computation is robust and therefore the parameters are not representative of a local minimum. Finally, in LSQNONLIN it is possible to use two different algorithms to solve the problem: the Levenberg-Marquardt algorithm and the Trust-region algorithm. They are very similar but the second one allows to add also the boundary limits which are very important in the case in point because they allow to confine the final results in the chosen limit values.

5.2 Model's parameters

It is necessary to choose which parameters of the model have to be update on the base of the analytical model and the influence that they have on the final results. The most important parameters for the analytical model are just seven:

- K_h, plunge stiffness;
- K_α, pitch stiffness;
- m_T, total mass of the system + mass of the wing;
- S_α, static moment of the system around the elastic axis;
- I_α, moment of inertia of the system around the elastic axis;
- ζ_h, plunge damping ratio;
- ζ_α, pitch damping ratio.

The masses and the inertia moments must be updated because they can not be measured directly with an experimental measure. The confidence on m_T, S_α and I_α

is very low because these parameters come from the CAD data or from the previous measures on a similar aerofoil. On the other hand, there is a good confidence on the measure of the stiffnesses K_h and K_α because they are computed by using the measures of high precision lasers. Finally, the measure of the damping is not very accurate because it is very difficult to identify this parameter in a good way. In general, all the physical distances are considered fixed because there are no large uncertainties on them and because it is easy to measure them.

The initial parameters given from the CAD data, from the previous model and from the experimental measures of *Chapter 4* are listed in Table 5.1:

Data	**Initial parameters**
ζ_h [-]	0.0049
ζ_α [-]	0.0108
m_T [Kg]	12.4518
I_α [Kgm^2]	0.0364
S_α [Kgm]	0.190
K_h [N/m]	8650
K_α [Nm/rad]	70

Table 5.1: Initial parameters obtained from the CAD model, from the previous studies on similar aerofoil and from experimental measures.

5.2.1 Model updating with seven parameters

The first attempt of updating is made with all the seven parameters. The fitting in this way appears perfect but the found parameters are probably not physical because there are too many updated parameters. The Figure 5.1 and 5.2 show the results. The dotted line curve indicates the analytical FRF obtained using very rough starting data while the continuous curve indicates the optimized analytical FRF. The black curve indicates the experimental data obtained at zero wind-speed. The Table 5.2 shows the final optimized parameters. Since the stiffnesses have been measured with high accuracy, there is a too large change of them. In particular the pitch spring change its value a lot and this probably means that the parameters found are not completely physical.

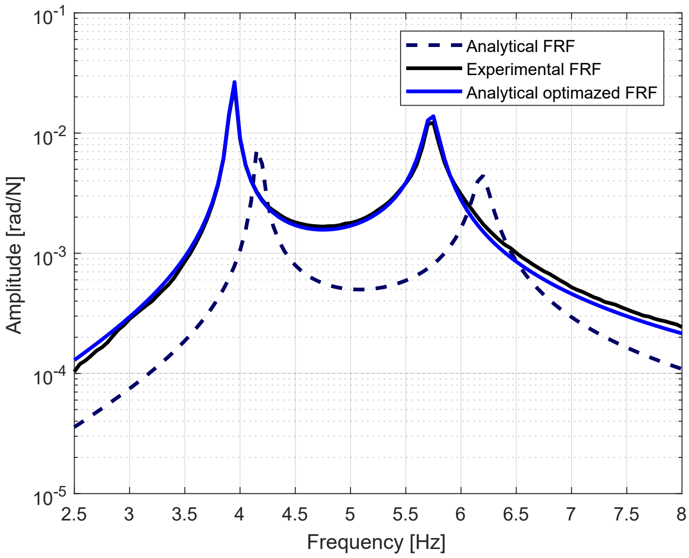

Figure 5.1: Updated pitch FRF with seven parameters.

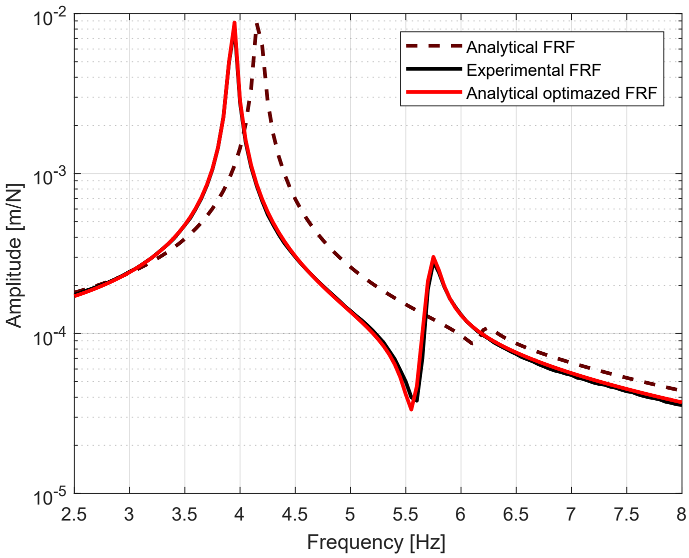

Figure 5.2: Updated plunge FRF with seven parameters.

Data	Initial parameters	Final parameters
ζ_h [-]	0.0049	0.0040
ζ_α [-]	0.0108	0.0100
m_T [Kg]	12.4518	15.3528
I_α [Kgm^2]	0.0364	0.0502
S_α [Kgm]	0.190	0.150
K_h [N/m]	8650	9660
K_α [Nm/rad]	70	61.45

Table 5.2: Optimized parameters: the listed parameters come from the model updating by using seven different parameters in the optimizer function.

5.2.2 Model updating with three parameters

Since in the FRFs has just two peaks, it is possible to update only few parameters in the model updating. Therefore the numbers of updated parameters is now reduced at three. The model's updating is performed in the following way:

- K_h and K_α are not updated but they are measured experimentally as described in *Chapter 4* and they are kept constant;
- m_T, S_α, I_α are updated with the optimizer function;
- ζ_h and ζ_α are updated before with optimizer function and after manually modified;

A very good fitting between the experimental and the numerical data is obtained by applying the described procedure and the Figure 5.3 and 5.4 show the results. Since the optimizer requires the difference between the experimental and the analytical FRFs, it is necessary to find out a way to write analytically the system FRFs. The experimental FRFs have been obtained with just the excitation in plunge direction, therefore the analytical one has to be built in the same way. The Equation 5.2 describes the model used to get the analytical FRF.

$$\begin{bmatrix} m_T & S_\alpha \\ S_\alpha & I_\alpha \end{bmatrix} \begin{Bmatrix} \ddot{h} \\ \ddot{\alpha} \end{Bmatrix} + \begin{bmatrix} c_h & 0 \\ 0 & c_\alpha \end{bmatrix} \begin{Bmatrix} \dot{h} \\ \dot{\alpha} \end{Bmatrix} + \begin{bmatrix} k_h & 0 \\ 0 & k_\alpha \end{bmatrix} \begin{Bmatrix} h \\ \alpha \end{Bmatrix} = \begin{Bmatrix} F \\ 0 \end{Bmatrix} \tag{5.2}$$

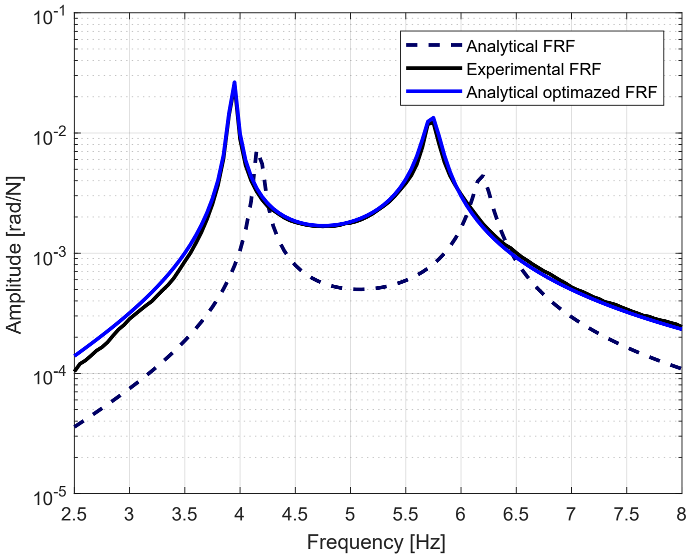

Figure 5.3: Updated pitch FRF with three parameters.

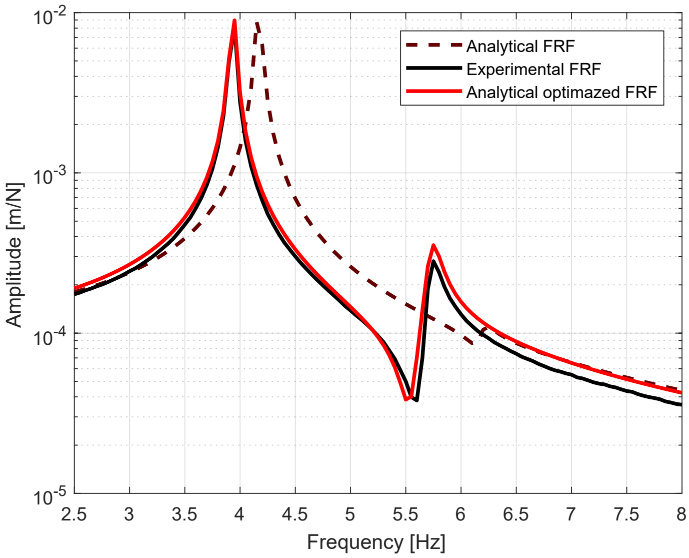

Figure 5.4: Updated plunge FRF with three parameters.

By rewriting the equation in the Laplace domain it is possible to obtain the analytical FRF in the following way:

$$H(s) = \frac{I_\alpha s^2 + c_\alpha s + K_\alpha}{(m_T s^2 + +c_h s + K_h)(I_\alpha s^2 + c_\alpha s + K_\alpha) - S_\alpha^2 s^4} \tag{5.3}$$

$$A(s) = -\frac{S_\alpha s^2}{(m_T s^2 + +c_h s + K_h)(I_\alpha s^2 + c_\alpha s + K_\alpha) - S_\alpha^2 s^4} \tag{5.4}$$

The Equations 5.4 and 5.3 represent the mathematical expression to compute respectively: the plunge FRFs and the pitch FRF. The updated parameters are shown in the following Tables 5.3 and 5.4.

Data	**Initial parameters**	**Final parameters**
ζ_h [-]	0.0049	0.0048
ζ_α [-]	0.0108	0.0113

Table 5.3: Semi-automatically optimized parameters.

Data	**Initial parameters**	**Final parameters**
m_T [kg]	12.4518	13.6598
I_α [kgm^2]	0.0364	0.0578
S_α [kgm]	0.190	0.165

Table 5.4: Automatically optimized parameters.

The large variation of S_α, I_α and m_T is due to the fact that the first starting data are calculated from the CAD model which represents only the wing and not the external structure while the total mass is taken from a model previously developed on the same support structure. Using these updated data, with an elastic axis position of 132 mm from the leading-edge tip, the flutter-speed is about 16.7 m/s and a quite good fitting of the FRFs is obtained. The experimental flutter-speed is about 15.7 m/s therefore the difference between the experimental and the analytical model is not so large. The position of the elastic axis computed with the CAD model is not so accurate. In fact, the physical plays between the connected parts can modify this measure during the assembling process. To improve the flutter-speed prediction, the position of the elastic axis is measured again directly on the physical model and the Table 5.5 shows the measures.

By using the new axis position it is possible to predict a better analytical flutter-speed which changes from 16.7 m/s to 16.2 m/s, therefore there is a difference of just 0.5 m/s between the predicted and the experimental flutter-speed. To confirm

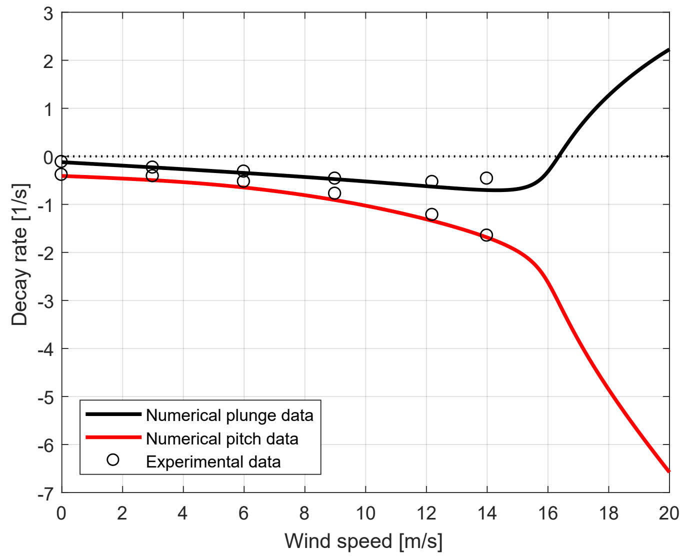

Figure 5.5: Decay rate: compare between the experimental and the numerical results.

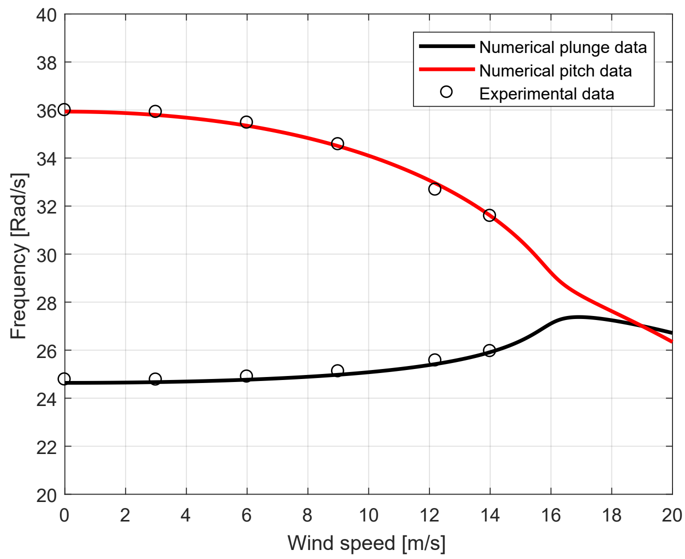

Figure 5.6: Frequencies: compare between the experimental and numerical results.

the goodness of the results, the experimental poles are compared with the numerical predicted ones. The experimental poles are extracted by the FRFs computed with the wind described in *Chapter 4*. The trend of the real parts of the poles is represented in Figure 5.5. For the sake of completeness, the trend of the imaginary parts of the poles has also been plotted in the Figure 5.6. Since there is a very good fitting between the experimental and the analytical data and there is a very good prediction of the flutter-speed, it is possible to consider the model completely updated.

Data	**Initial measure from CAD**	**Experimental measure**
Elastic axis [mm]	132	136

Table 5.5: Elastic axis position from the leading-edge tip.

Chapter 6

Control Strategy and Experimental Implementation

The wing model has to be controlled in order to avoid the flutter onset, therefore a control system is necessary. The controller applies experimentally a control law by using the dSPACE for the closed- and open-loop system. The receptance method [10] is used to apply the control strategy for the closed-loop system and the numerical and experimental results are discussed in this chapter.

6.1 Controller

The controller is composed by an high authority control (HAC) and a low authority control (LAC). The LAC and HAC work together to control the system in open-loop and closed-loop mode. Basically, the LAC is represented by the PID control which is implemented in the dSPACE. It controls the position of flaps with respect the given signal: if the signal given to the PID is a constant position or sinusoidal signal, the system is working as an open-loop system while, if the given signal comes from the HAC, the system is working as a closed-loop system because the signal is related to the position of the aerofoil. The HAC is a PD control which creates the control signal on the base of the displacements and the velocities given by the two lasers. Both the controls are written in SIMULINK and converted in C++ code in order to implement them in the dSPACE controller. A control interface allows to monitor and to set all the parameters written in the SIMULINK code and the dSPACE is able to apply the instruction in real time. The gains K_i, K_d and K_p applied in the LAC have been obtained in *Chapter 4* with the Ziegler - Nichols method in a completely experimental way, while the gains applied on the HAC are obtained through the experimental application of the receptance method.

The Figure 6.1 represents the general scheme of the control architecture where:

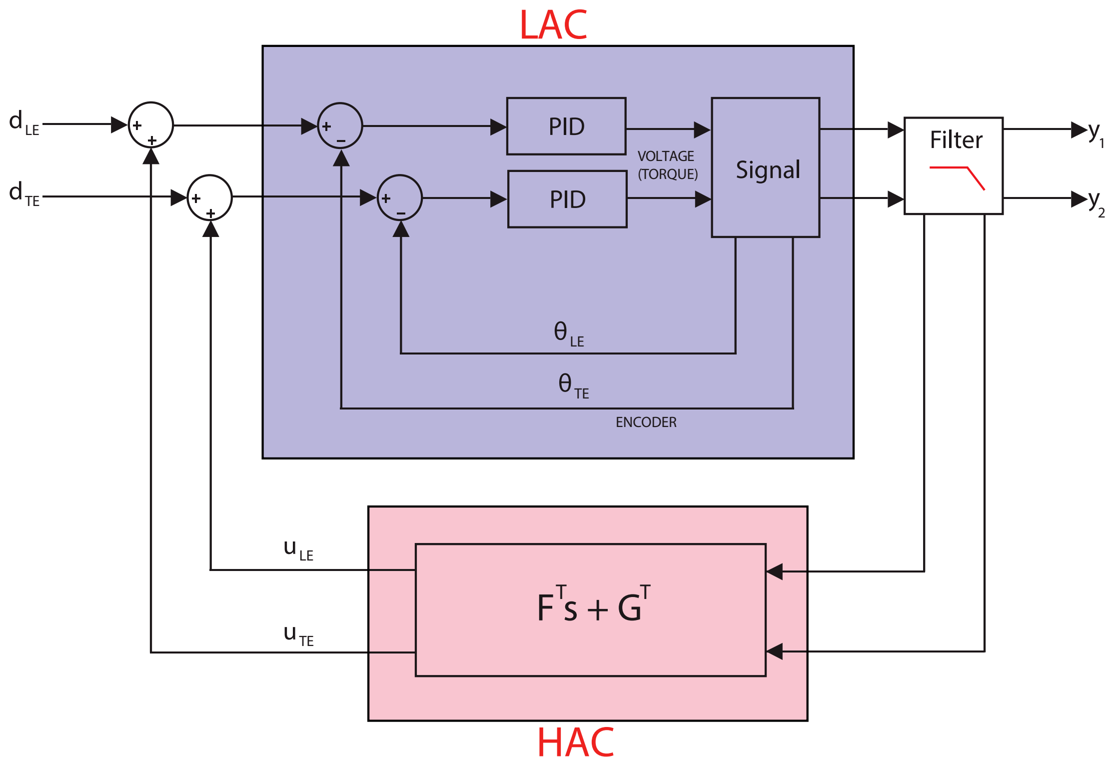

Figure 6.1: Representation of the control scheme with HAC and LAC.

- d_{LE} and d_{TE} represent the disturbance signals given to the control system;
- θ_{LE} and θ_{TE} represent the angular position read by the encoders;
- y_1 and y_2 represent the lasers positions;
- u_{LE} and u_{TE} represent the control law given from the HAC.

It is important to notice that the outputs in the analytical model can be chosen by properly defining the matrix $\mathbf{C_{ss}}$. The experimental MIMO system has two outputs and two inputs, respectively: the two lasers and the two flap angles. In the open-loop configuration, the control system receives the disturbances d_{LE} and d_{TE} which can be a sinusoidal signal or just a constant position. The disturbance signal is compared with the actual position, θ_{LE} and θ_{TE}, of the trailing- and leading-edge flap and a voltage is computed and applied to each motor. In this way, the motors are able to follow exactly the given input signal. In closed-loop configuration, the system outputs y_1 and y_2 are given to HAC which is able to apply different gains: $\mathbf{F}^T$ is the derivative gains matrix while $\mathbf{G}^T$ is the proportional gains matrix. By applying these gains the HAC is able to compute and to pass to the LAC two different signals u_{LE} and u_{TE} which describe the required control law applied on the flaps. In particular the Figure 6.2 represents in detail the PID control implemented in the LAC. The encoder signal is compared with the disturbance signal and the difference of the two signals is multiplied by the gains. The derivative gains is applied on the derivative of the signal while the integrative gains multiplies the integrated signal. The total sum of the outputs signal is converted in voltage in order to apply the required torque on the motor.

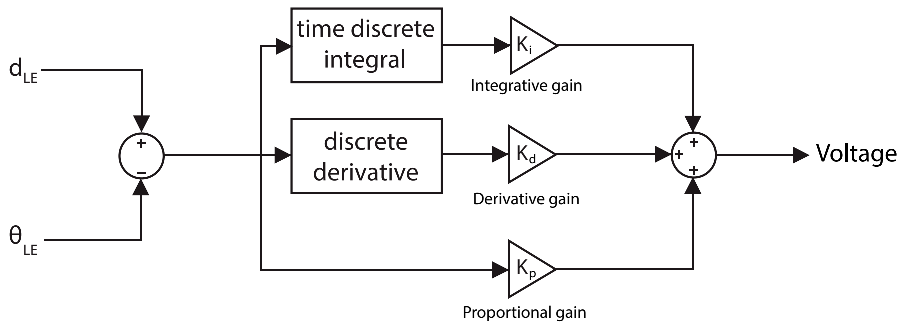

Figure 6.2: Representation of the PID control for the leading-edge flap. The same representation can be applied for the trailing-edge flap.

The HAC is represented in detail by the Figure 6.3. The two laser signals are used to compute the angular position signal u. In this case there are just the proportional and the derivative gains because the HAC is a PD control. In the closed-loop system, the control law u is given to LAC in order to control the flaps in the required way.

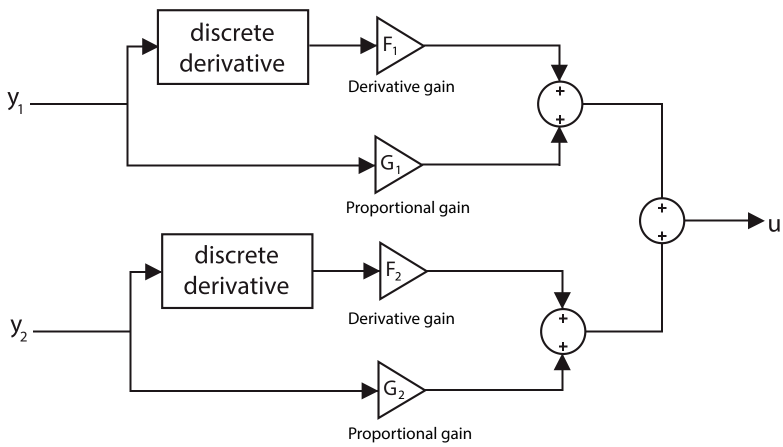

Figure 6.3: Representation of the PD control.

6.2 The receptance method

The receptance method is an experimental method based on the knowledge of the receptance $\mathbf{H(s)}$ where s is the Laplace variable. By using the computed receptance or a transfer function $\mathbf{R(s)}$ which includes the receptance, the method is able to compute the gains matrices $\mathbf{F}^T$ and $\mathbf{G}^T$ which place the poles on the desired location. The method can be applied both numerically and experimentally and it can be used both on SISO system and on MIMO system. In this case just the MIMO version of the receptance method is explained and applied.

6.2.1 Theory of receptance method

A quick explanation of the theory of the receptance method described by Mottershead et al. [10] is given in this section. The original theory described by Ram et al. [12] is based on the Sherman-Morrison formula which allows the application of the method just on SISO systems. A reformulation of the method [10] allows the extension to the MIMO system with which is possible to apply the full pole placement or the partial pole placement.

Let $\mathbf{M}$, $\mathbf{C}$ and $\mathbf{K}$ be $\in \mathrm{R}^{n\times n}$ and respectively the general mass, damping and stiffness matrices of a MIMO system where n is the number of degrees of freedom and m represents the number of inputs. $\mathbf{M}$ is positive defined and symmetric matrix while $\mathbf{C}$ and $\mathbf{K}$ are symmetric and semi-positive defined matrices and $\mathbf{B}$ represents the control matrix. The open-loop eigenvalues and eigenvectors are respectively λ_k and $\mathbf{v_k}$ while the closed-loop eigenvalues and eigenvectors are μ_k and $\mathbf{w_k}$. The matrix $\mathbf{B}$ is composed by the control vector of each input, $\mathbf{B} = [\mathbf{b_1}, ..., \mathbf{b_m}]$. In the same way it is possible to write all the gains feedback matrices, in fact $\mathbf{F} = [\mathbf{f_1}, ..., \mathbf{f_m}]$ and $\mathbf{G} = [\mathbf{g_1}, ..., \mathbf{g_m}]$. The idea is to place the first p poles of the system in the desired location and to maintain the non-placed poles λ_k for $k = p+1, ...,2n$ in same position. The receptance method starts from the definition of the quadratic eigenvalues problem which in open-loop system is:

$$(\lambda_k{}^2\mathbf{M} + \lambda_k\mathbf{C} + \mathbf{K})\mathbf{v_k} = 0 \quad k = 1, ...,2n \tag{6.1}$$

and in closed-loop system is:

$$(\mu_k{}^2\mathbf{M} + \mu_k\mathbf{C} + \mathbf{K})\mathbf{w_k} = \mathbf{B}(\mu_k\mathbf{F}^T + \mathbf{G}^T) \quad k = 1, ...,2n \tag{6.2}$$

By making some mathematical passages it is possible to creates two matrix equations from the definition of the quadratic eigenvalue problems. For the first p placed poles μ_k, the receptance method gives the following equation:

$$
\begin{bmatrix}
\mu_k \mathbf{w_k}^T & 0 & \dots & 0 & \mathbf{w_k}^T & 0 & \dots & 0 \\
0 & \mu_k \mathbf{w_k}^T & \dots & 0 & 0 & \mathbf{w_k}^T & \dots & 0 \\
\vdots & \vdots & \ddots & \vdots & \vdots & \vdots & \ddots & \vdots \\
0 & 0 & \mu_k \mathbf{w_k}^T & \dots & 0 & 0 & \mathbf{w_k}^T & \dots
\end{bmatrix}
\begin{Bmatrix} \mathbf{f_1} \\ \vdots \\ \mathbf{f_m} \\ \mathbf{g_1} \\ \vdots \\ \mathbf{g_m} \end{Bmatrix}
=
\begin{Bmatrix} \alpha_{\mu_k,1} \\ \alpha_{\mu_k,2} \\ \vdots \\ \alpha_{\mu_k,m} \end{Bmatrix}
\tag{6.3}
$$

In a simple compact notation the equation appears as:

$$\mathbf{P}_k \mathbf{y} = \alpha_{\mathbf{k}} \quad k = 1, \dots, p \tag{6.4}$$

Where the closed-loop eigenvectors can be defined with the following equation:

$$\mathbf{w_k} = \alpha_{\mu_k,1} \mathbf{r}_{\mu_k,1} + \dots + \alpha_{\mu_k,m} \mathbf{r}_{\mu_k,m} \quad k = 1, \dots, p \tag{6.5}$$

The coefficients $\alpha_{\mu_k,j}$ are the arbitrary coefficients that come from the definition of the problem and $\mathbf{r}_{\mu_k,j}$ are the column vector of the transfer function matrix $\mathbf{R}(\mu_\mathbf{k}) = \mathbf{H}(\mu_\mathbf{k})\mathbf{B}$ computed with the placed poles μ_k. The arbitrary coefficients $\alpha_{\mu_k,j}$ represent the weight scalar factors with which the closed-loop eigenvectors $\mathbf{w_k}$ are determined.

The method provides a matrix equation also for the non-placed poles λ_k. For $k = p+1, \dots, 2n$ the correspondent matrix equation is:

$$
\begin{bmatrix}
\lambda_k \mathbf{v_k}^T & 0 & \dots & 0 & \mathbf{v_k}^T & 0 & \dots & 0 \\
0 & \lambda_k \mathbf{v_k}^T & \dots & 0 & 0 & \mathbf{v_k}^T & \dots & 0 \\
\vdots & \vdots & \ddots & \vdots & \vdots & \vdots & \ddots & \vdots \\
0 & 0 & \lambda_k \mathbf{v_k}^T & \dots & 0 & 0 & \mathbf{v_k}^T & \dots
\end{bmatrix}
\begin{Bmatrix} \mathbf{f_1} \\ \vdots \\ \mathbf{f_m} \\ \mathbf{g_1} \\ \vdots \\ \mathbf{g_m} \end{Bmatrix}
=
\begin{Bmatrix} 0 \\ 0 \\ \vdots \\ 0 \end{Bmatrix}
\tag{6.6}
$$

In a simple compact notation the equation appears as:

$$\mathbf{Q}_k \mathbf{y} = \mathbf{0} \quad k = p+1, \dots, 2n \tag{6.7}$$

From Equations 6.3 and 6.6, the pole placement for a MIMO system can be actuated by solving the following linear system:

$$
\begin{bmatrix} \mathbf{P_1} \\ \vdots \\ \mathbf{P_p} \\ \mathbf{Q_{p+1}} \\ \vdots \\ \mathbf{Q_{2n}} \end{bmatrix}
\begin{Bmatrix} \mathbf{f_1} \\ \vdots \\ \mathbf{f_m} \\ \mathbf{g_1} \\ \vdots \\ \mathbf{g_m} \end{Bmatrix}
=
\begin{Bmatrix} \alpha_\mathbf{1} \\ \vdots \\ \alpha_\mathbf{1} \\ \mathbf{0} \\ \vdots \\ \mathbf{0} \end{Bmatrix}
\tag{6.8}
$$

The mathematical structure of the method allows to apply it experimentally in a very simple way; in fact, the receptance matrix $\mathbf{H}$ can be measured and implemented in the method. There is no need to identify the matrices $\mathbf{M}$,$\mathbf{C}$ and $\mathbf{K}$ because the receptance is sufficient to apply the method. The main drawback consists in the choice of the arbitrary coefficients in multiple pole placement when the $m > 1$. In fact, the gains $\mathbf{f_j}$ and $\mathbf{g_j}$ are dependent on the choice of such parameters $\alpha_{\mu_k,j}$ from which the closed-loop eigenvectors are imposed. In fact, the receptance method is able to place all the poles and all the eigenvectors of a MIMO system with the same number of sensors and the same number of input.

6.2.2 Mathematical implementation in a state space system

In *Chapter 2*, the presence of aerodynamic loads has brought to have the numerical model represented in the state space form. On the other hand, in *Chapter 4* also the experimental FRFs have been transformed into four state space matrices, therefore the is no possibility to use in the receptance method the matrices $\mathbf{M}$, $\mathbf{C}$, $\mathbf{K}$ and certainly not the matrix $\mathbf{B}$ because they are completely unknown. Anyway, it is possible to get the transfer function between the output $\mathbf{y}$ and the input $\mathbf{u}$, in the following way:

$$\mathbf{R(s)} = \mathbf{C_{ss}}(\mathbf{I_{ss}}s - \mathbf{A_{ss}})^{-1}\mathbf{B_{ss}} + \mathbf{D_{ss}} \tag{6.9}$$

Where s represents the generic Laplace variable. When s is replaced with μ_k, each column of the transfer function $\mathbf{R}(\mu_\mathbf{k})$ represents exactly the vectors $\mathbf{r}_{\mu_k,j}$ used in the receptance method for the definition of the closed-loop eigenvectors $\mathbf{w_k}$. Therefore, the closed-loop eigenvector $\mathbf{w_k}$ and the matrix $\mathbf{P_k}$ can be easily obtained. The problem come from the definition of the open-loop eigenvector $\mathbf{v_k}$ because there is not a simple definition. The simplest solution consists into using directly one column of the transfer function $\mathbf{R}(\lambda_\mathbf{k})$ as open-loop eigenvector $\mathbf{v_k}$, i.e when the Laplace variable s is replaced with the open-loop pole λ_k. Since the transfer function is computed for the open-loop pole, just a column of $\mathbf{R}(\lambda_\mathbf{k})$ is required to apply the method and so it is possible to get easily $\mathbf{v_k}$ and the matrix Q_k. The main drawback of this solution consists in the development of numerical problems which may bring to wrong results, in fact the computation of $\mathbf{R}(\lambda_\mathbf{k})$ leads to inversion of an ill-conditioned matrix. A possible solution of this problem is to apply directly the experimental open-loop eigenvectors into the method in order to avoid the computation of $\mathbf{R}(\lambda_\mathbf{k})$. Obviously, in the numerical application this is not possible and the numerical error can not be avoided.

The application of the receptance method is the same for the numerical and the experimental application. The only difference between the two sets of matrices consists into the definition of the outputs. In fact, the experimental transfer function is obtained by considering the angle of the flaps as inputs and the lasers positions as outputs while the plunge displacement and the pitch angle were used as outputs in the analytical model. Therefore, in the experimental case the outputs do not coincide with the states anymore. It is necessary to figure out a new way to write the closed-loop system in order to compute the new closed-loop poles after the application of the receptance method. The state space matrices allow to write two equations from which it is possible to find the solution to this problem:

$$\dot{\mathbf{x}} = \mathbf{A_{ss}}\mathbf{x} + \mathbf{B_{ss}}\mathbf{u} \tag{6.10}$$

$$\mathbf{y} = \mathbf{C_{ss}}\mathbf{x} + \mathbf{D_{ss}}\mathbf{u} \tag{6.11}$$

By replacing the Equation 2.66 in 6.10:

$$\dot{\mathbf{x}} = \mathbf{A_{ss}}\mathbf{x} + \mathbf{B_{ss}}(\mathbf{F}^T\dot{\mathbf{y}} + \mathbf{G}^T\mathbf{y}) \tag{6.12}$$

Since $\mathbf{D_{ss}}$ is a null matrix, thus it is possible to derive the Equation 6.11 and to get:

$$\dot{\mathbf{x}} = \mathbf{A_{ss}}\mathbf{x} + \mathbf{B_{ss}}(\mathbf{F}^T\mathbf{C_{ss}}\dot{\mathbf{x}} + \mathbf{G}^T\mathbf{C_{ss}}\mathbf{x}) \tag{6.13}$$

By rearranging it is possible to obtain the solution:

$$\dot{\mathbf{x}} = (\mathbf{I_{ss}} - \mathbf{B_{ss}}\mathbf{F}^T\mathbf{C_{ss}})^{-1}(\mathbf{A_{ss}} + \mathbf{B_{ss}}\mathbf{G}^T\mathbf{C_{ss}})\mathbf{x} \tag{6.14}$$

Again, by using the new dynamic matrix, it is possible to solve the associated eigenvalues problem and to obtain thesystem poles.

6.2.3 Numerical results

The receptance method may be applied numerically; in fact, it is necessary to know just the receptance matrix to use the method. Since the MIMO system has two outputs and two inputs, it is possible to place all the eigenvectors and all the eigenvalues but the nature of the instability problem brings to increase the damping and to separate the frequencies in order to avoid the premature onset of the flutter. To have the same representation of the previous experimental FRFs of *Chapter 4*, the numerical inputs are the flap angles and the numerical outputs are the laser displacements. It is possible to change the damping or the frequency of each pole, therefore the pitch mode, the plunge mode and both the modes together can be modified.

For the sake of simplicity, just three numerical tests are performed at the windspeed of 12.8 m/s:

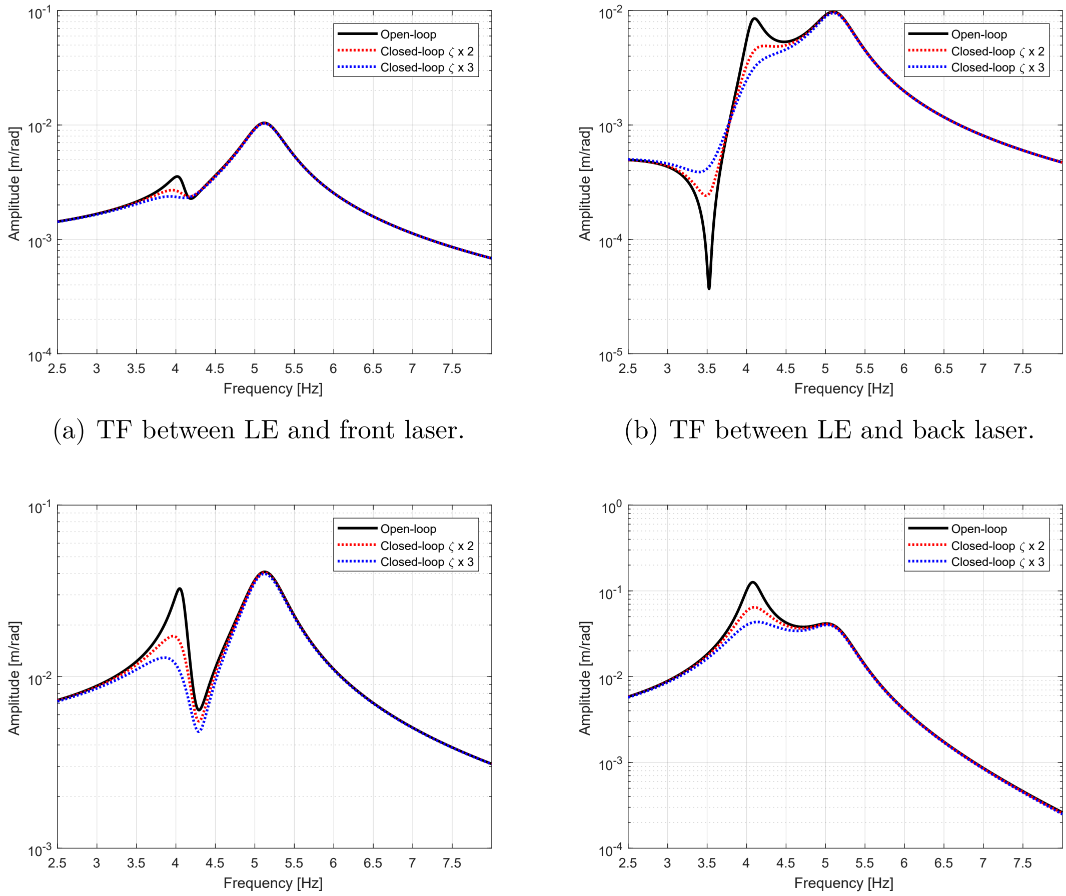

(a) TF between LE and front laser.

(b) TF between LE and back laser.

(c) TF between TE and front laser.

(d) TF between TE and back laser.

Figure 6.4: Test 1, numerical increase of plunge damping at 12.8 m/s.

- *test 1*: increase of plunge damping ;
- *test 2*: increase of plunge and pitch damping together;
- *test 3*: decrease of plunge frequency.

Although the method is able to place just the imaginary part and real part of the poles, it is possible to speak about control of the damping or control of the frequency because the difference between the two quantities is very small. The transfer functions between inputs and outputs of the analytical system are also influenced by the poles placement. In fact, it is possible to check the efficiency of the control by plotting on the same plane the closed-loop and the open-loop FRFs. The *test 1* provides for having the real part of the first pole multiplied by a factor

2 and for a factor 3. The FRFs numerically obtained for the first test are shown in the Figure 6.4. All the figures confirm that the poles placement is done correctly because the peak of the plunge mode decreases. The Figure 6.7(a) shows the pole placement for the first numerical tests and the Table 6.1 shows the obtained poles. Since the method is applied numerically, the pole placement is perfect and there is no difference between the expected poles and the computed ones.

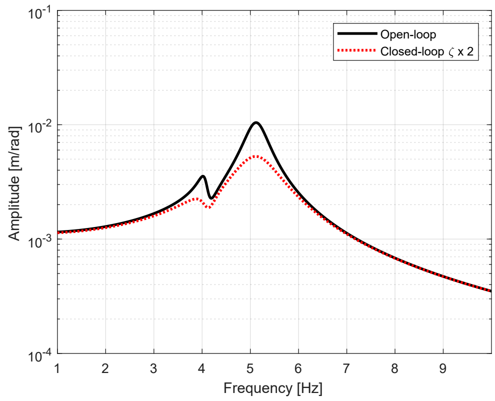

(a) TF between LE and front laser.

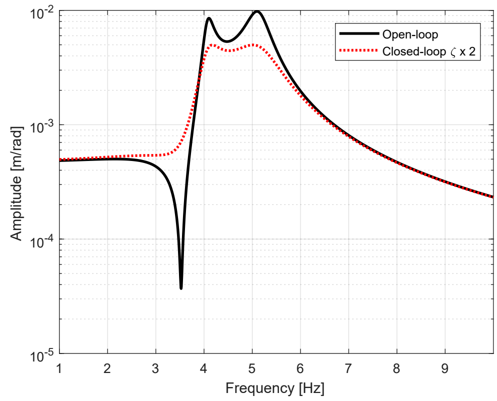

(b) TF between LE and back laser.

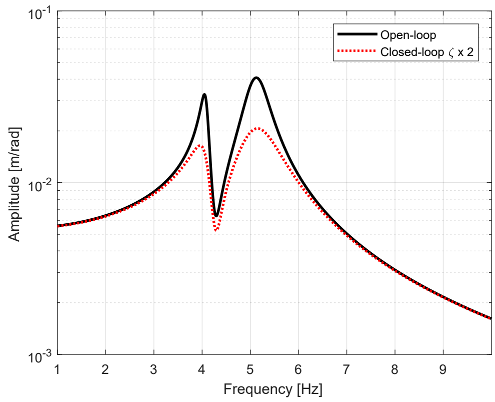

(c) TF between TE and front laser.

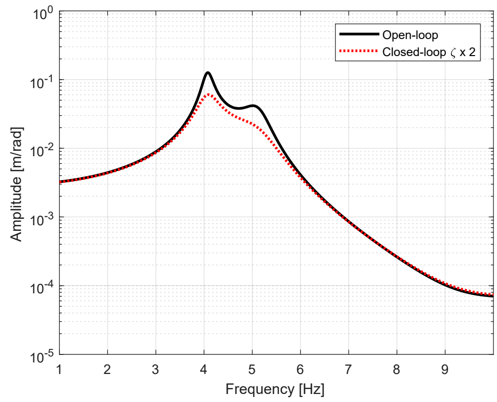

(d) TF between TE and back laser.

Figure 6.5: Test 2, numerical increase of damping for both the modes at 12.8 m/s.

The *test 2* provides for doubling the real parts of the poles of both the modes. The Figure 6.5 shows the transfer function in open- and closed-loop and it is possible to notice that both the peaks reduced their maximum amplitude, therefore the control is made correctly. Also in this case the numerical results have not errors and the pole placement in the complex plane is represented in Figure 6.7(b). It is

Parameter	**Open-loop pole**	**Closed-loop pole, $\zeta \times 2$**	**Closed-loop pole, $\zeta \times 3$**
First pole	-0.64499±25.5811i	-1.2999±25.5811i	-1.9498±25.5811i
Second pole	-1.4720±32.1809i	-1.4720±32.1809i	-1.4720±32.1809i

Table 6.1: Pole placement of the first numerical test.

possible also to control the imaginary part of the poles as requested by *test 3* where the plunge frequency is decreased by the 5 % and the 10 %. In fact, the Figure 6.6 shows the four transfer functions in open-loop and closed-loop system for the last numerical test.

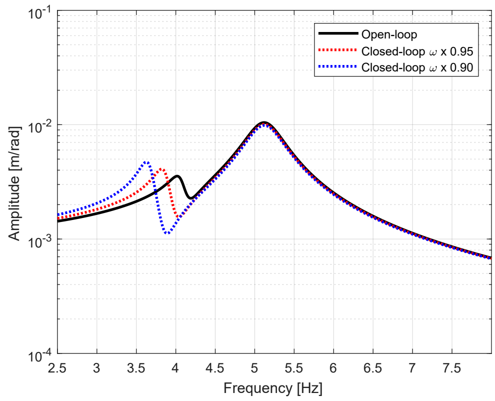

(a) TF between LE and front laser.

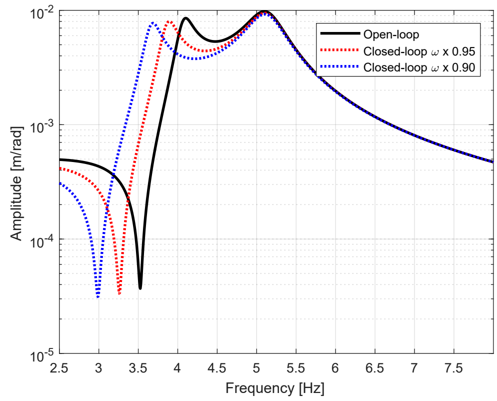

(b) TF between LE and back laser.

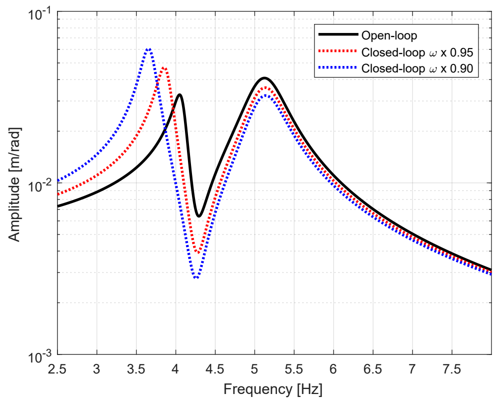

(c) TF between TE and front laser.

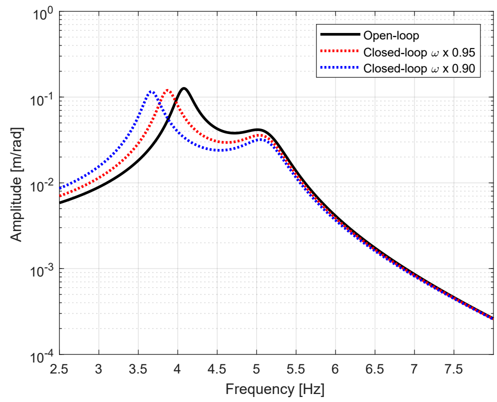

(d) TF between TE and back laser.

Figure 6.6: Test 3, numerical decrease of plunge frequency at 12.8 m/s.

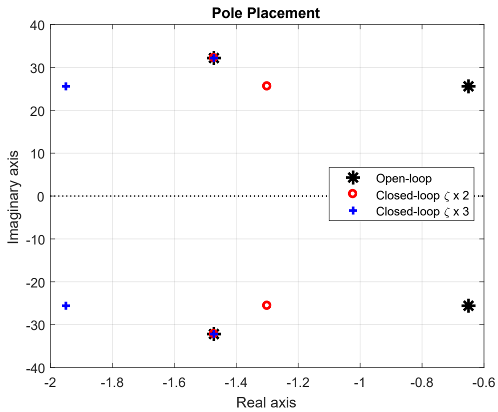

(a) Increase of plunge damping.

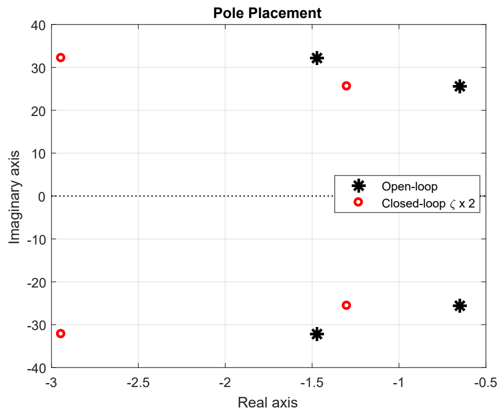

(b) Increase of both the damping's modes.

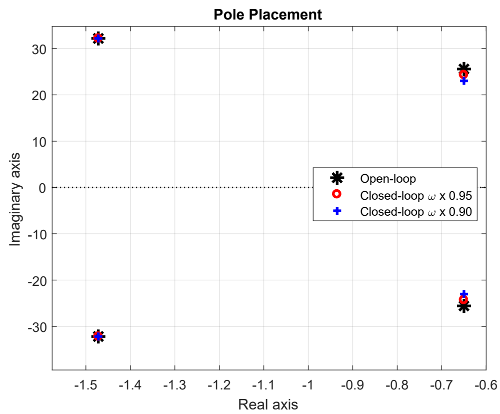

(c) Reduction of plunge frequency.

Figure 6.7: Pole placement for different cases at 12.8 m/s.

Finally, the representation of the poles in the complex plane of Figure 6.7(c) shows the position of the new poles. Also in this case all the FRFs are perfectly modified and all the poles are perfectly placed. The poles are perfectly placed without any errors because the method is applied just numerically. In this case the obtained gains are probably wrong for an experimental application, therefore they are not reported. In fact the receptance method have to be applied experimentally to obtain good results. In the numerical case, the arbitrary coefficients $\alpha_{\mu_k,j}$ are kept equal to 1 and 1 for the plunge mode and they are fixed at the values 1 and -0.5 for the pitch mode in all the cases. These coefficients are able to affect the gains and to divide the control effort between the two flaps: in fact, by choosing $\alpha_{\mu_1,1} = 0$ the leading-edge flaps will not work. Therefore, by choosing properly the α coefficients, it is possible to keep the gains as low as possible. In particular when the closed-loop eigenvectors are kept equal to the open-loop eigenvectors the gains are the lowest possible because the control is moving just the poles. From the numerical point of view this is not particularly interesting because it is not possible to know exactly the control effort.

6.3 Experimental results

The receptance method is now experimentally applied. At this point, the implementation is very simple since in the previous sections the method has been explained and applied. Moreover, in *Chapter 4* it has been explained how to find experimentally the state space matrices, therefore it is necessary just to use the experimental state space matrices in the receptance method to find the solution. In the experimental case, the coefficients $\alpha_{\mu_k,j}$ have a very important role: in fact, they impose the closed-loop modeshapes and so the control effort. If the control effort is too large, the physical system may be not able to apply the computed gains to get the pole placement. Too large gains are very dangerous for the physical model because they can lead to break the moving control surfaces. All the experimental results are obtained by applying the experimental control gains and the FRFs in closed-loop are acquired by exciting the structure with the shaker when the system is controlled in closed-loop mode.

6.3.1 Partial pole placement

In the first experimental tests the a partial pole placement is applied by using the receptance method. The experimental results are obtained by applying the following coefficients: $\alpha_{\mu_1,1} = 1$ $\alpha_{\mu_1,2}$ =1 for the control of the first two poles and $\alpha_{\mu_1,1} = 1$ $\alpha_{\mu_1,2}$ =−0.5 for the control of the second two poles. These coefficients are chosen arbitrarily in order to find low gains and they are optimized experimentally with different tests in order to find the lowest control effort. Four different kind of tests have been carried out in order to see the efficiency of the receptance method:

- *test 1*: increase of plunge damping with $\zeta_1 \times 2$ and $\zeta_1 \times 3$;
- *test 2*: increase of pitch damping with $\zeta_2 \times 2$ and $\zeta_2 \times 3$;
- *test 3*: decrease of plunge frequency with $\omega_1 \times 0.96$ and $\omega_1 \times 0.90$;
- *test 4*: increase of pitch frequency with $\omega_2 \times 1.04$ and $\omega_2 \times 1.10$.

In order to have better results and less control effort, the experimental open-loop poles λ_k and the experimental open-loop mode-shapes $\boldsymbol{v_k}$, are directly inserted into the receptance method's code and they are used to compute the matrix $\mathbf{Q_i}$. They have been computed by using same FRFs used for the computation of the matrices $\mathbf{A_{ss}}$, $\mathbf{B_{ss}}$, $\mathbf{C_{ss}}$ and $\mathbf{D_{ss}}$. A little drawback of this method is that the numerical pole placement is not perfect anymore but there is a very little change also in the fixed poles. This operation is useful in order to avoid numerical errors related to the computation of the open-loop modeshapes directly from the acquired receptance. In fact the computation of $\mathbf{R}(\lambda_\mathbf{k})$ creates a quasi-singular matrix which is very difficult to invert.

Increase of plunge damping

First of all, the increase of plunge damping is tested. In this particular case, the control effort is the lowest possible because the first pole and the real part of the poles are simple to control. The gains for the triple damping case are shown in the Table 6.2.

Gains	**Leading-edge**	**Trailing-edge**
f_1 [deg/mm]	-0.0281	-0.0280
f_2 [deg/mm]	-0.0273	-0.0273
g_1 [deg/mm]	0.6240	0.6240
g_2 [deg/mm]	0.6568	0.6567

Table 6.2: Obtained gains to triple the plunge damping at 12.8 m/s for the two control surfaces.

In this case the arbitrary coefficients $\alpha_{\mu_k,j}$ are both set equal to one in fact the gains for the leading- and trailing-edge flaps are very similar between themselves. The expected poles and the experimental found poles are graphically shown in Figure 6.8.

Even if the experimental pole placement is not perfect it is possible to notice that the poles trend is correct. In fact is clear that the plunge damping is increased a lot while the other poles are almost the same. This effect can be confirmed by the closed-loop FRFs of the front and back laser. The first peak decreases in amplitude because the damping is increasing and the other peak remains the same because the corresponding pole is kept constant. The experimental results are shown in the Figure 6.9.

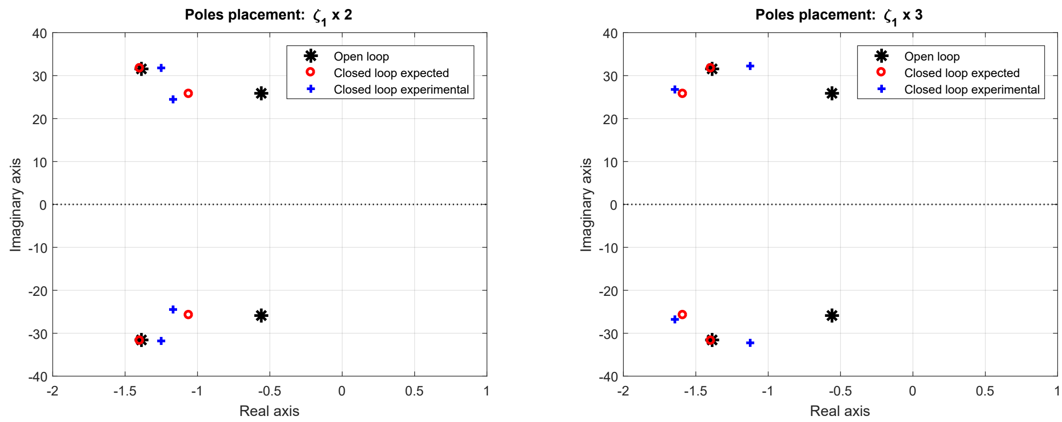

(a) Doubled plunge damping. (b) Tripled plunge damping.

Figure 6.8: Increase of plunge damping at 12.8 m/s by using the experimental natural eigenvectors.

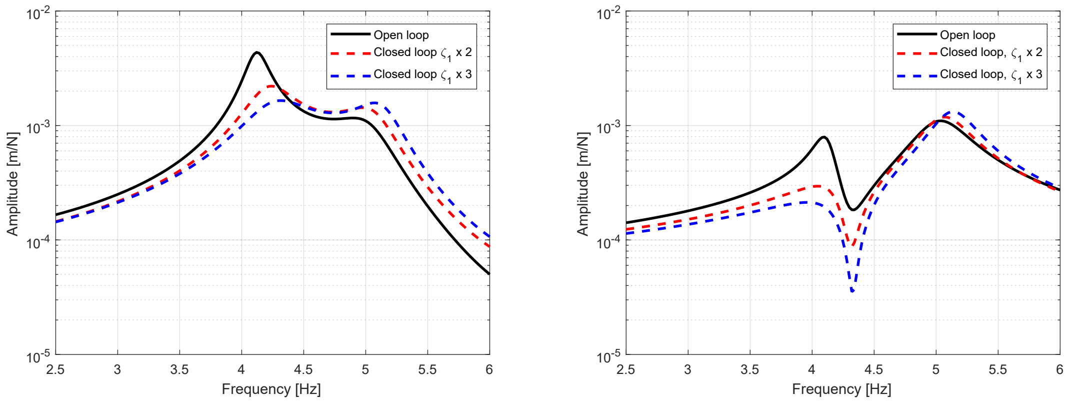

(a) Front laser output. (b) Back laser output.

Figure 6.9: Synthesized FRFs experimentally obtained for the increase of plunge damping at 12.8 m/s by using experimental open-loop eigenvectors.

Increase of pitch damping

With the receptance method is also possible to control the other pole of the system, therefore also the damping of the pitch mode can be increased. As before two tests have been carried out: the first one tries to double the pitch damping and the second one tries to triple the pitch damping. Also in this case the gains are not too large because the increase of damping does not require an excessive control effort. The Table 6.3 shows the gains to triple the damping.

Gains	Leading-edge	Trailing-edge
f_1 [deg/mm]	-0.0580	0.0145
f_2 [deg/mm]	0.0090	-0.0022
g_1 [deg/mm]	2.2186	-0.5547
g_2 [deg/mm]	-0.3423	0.0856

Table 6.3: Obtained gains to triple the pitch damping at 12.8 m/s for the two control surfaces.

In the case $\zeta_2 \times 3$, the real part of the second pole should be larger in the experimental results. In fact, the table 6.6 shows that there is a big difference between the expected and the experimental poles. This discrepancy can explained by taking into account the algorithm used to compute the poles from the FRFs: in fact, a very large damping is not easy to identify and it is very probable that the algorithm is not able to identify it correctly. Despite the identification problem, the complex plane shows the correct trend of the poles which are moving in the correct direction. In fact, the real part of second pole increases and the other pole is kept almost constant. Figure 6.10 shows the experimental and expected results in complex plane for both the cases.

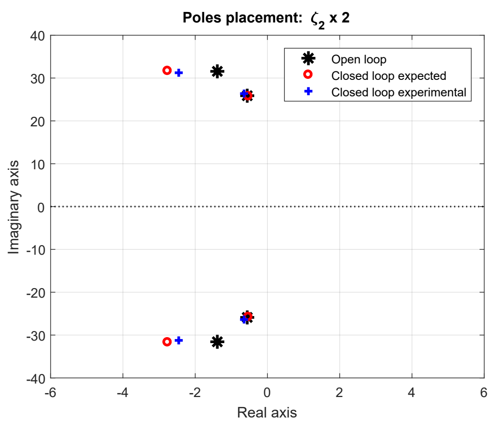

(a) Doubled pitch damping.

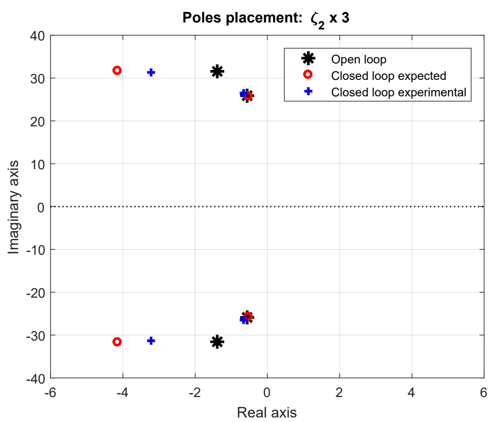

(b) Tripled pitch damping.

Figure 6.10: Increase of pitch damping at 12.8 m/s by using the experimental natural eigenvectors.

Finally the FRFs of the closed-loop and open-loop system are illustrated in Figure 6.11.

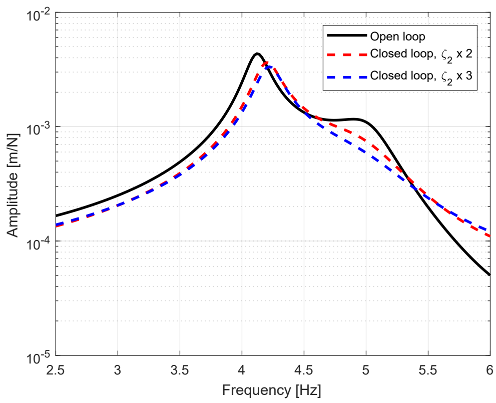

(a) Front laser output.

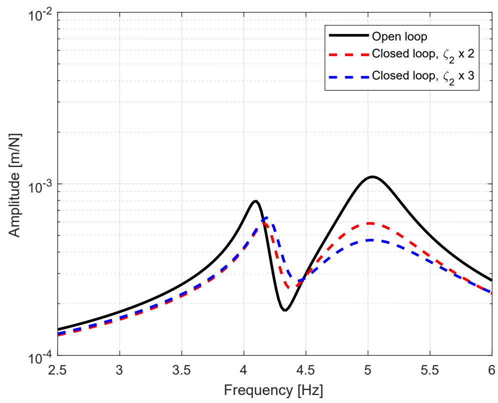

(b) Back laser output.

Figure 6.11: Synthesized FRFs experimentally obtained for the increase of pitch damping at 12.8 m/s by using experimental open-loop eigenvectors.

Decrease of plunge frequency

The imaginary part of the pole can be also controlled by using the receptance method. There is no doubt that in this case the control effort increases because the imaginary part is larger than the real part, as consequence the change of natural frequencies is lower with respect the change of system's damping. Two cases have been performed:

- change of frequency about 4%;
- change of frequency about 10%.

The change of resonance frequency can be performed by changing the imaginary part of the first pole. In this case by changing about 10% the plunge frequency, the gains appears larger with respect the previous cases. The Table 6.4 shows the experimental gains for moving the plunge frequency of 10 %. The representation of poles in the complex plane gives a better idea about the control efficiency. In fact also in this case the poles are placed at least in the correct direction as shown in Figure 6.12.

The closed-loop FRFs for both the studied cases confirm the efficiency of the controller and the correct movement of the experimental poles. The Figure 6.13 shows the FRFs computed for the closed- and open-loop system. It is possible to

Gains	Leading-edge	Trailing-edge
f_1 [deg/mm]	0.0685	0.0682
f_2 [deg/mm]	0.0704	0.0706
g_1 [deg/mm]	1.9026	1.9026
g_2 [deg/mm]	1.8352	1.8351

Table 6.4: Obtained gains to decrease the plunge frequency about 10% at 12.8 m/s for the two control surfaces.

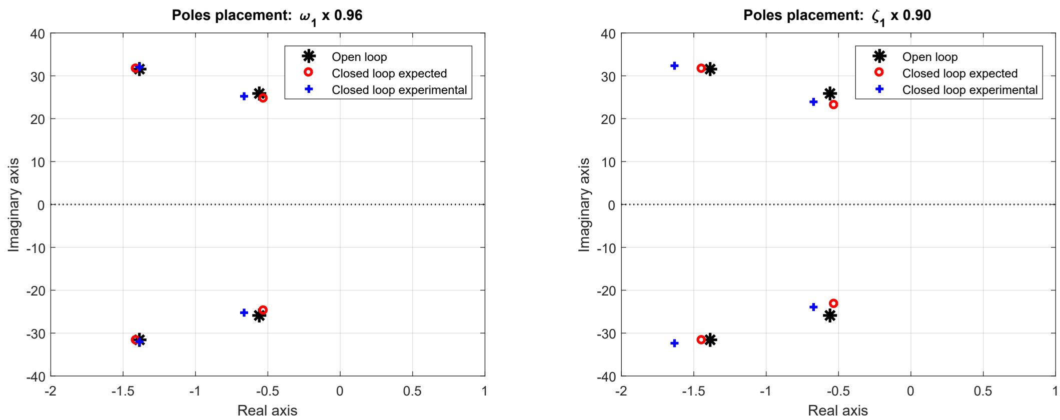

(a) Small decrease of plunge frequency.

(b) Large decrease of plunge frequency.

Figure 6.12: Decrease of frequency at 12.8 m/s by using the experimental natural eigenvectors.

notice that the system's FRFs in closed-loop and in open-loop have a different shape not only in the modified peak. Since the peaks appear to be placed in the correct position, the reason about this difference can be due by the fact that the FRF representation is just a section of 3D complex plane in which there are: amplitude, real and imaginary part of the poles. Therefore, it is possible to have a different shape of the FRF provided that the poles are correctly placed.

Increase of pitch frequency

For the sake of completeness also the imaginary part of the second poles is placed. As before the imaginary part is increased about 4% and about 10%. The Table 6.5

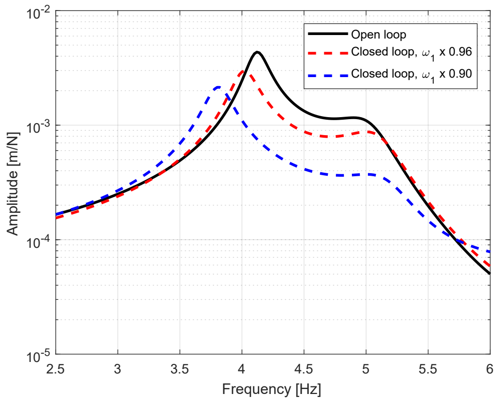

(a) Front laser output.

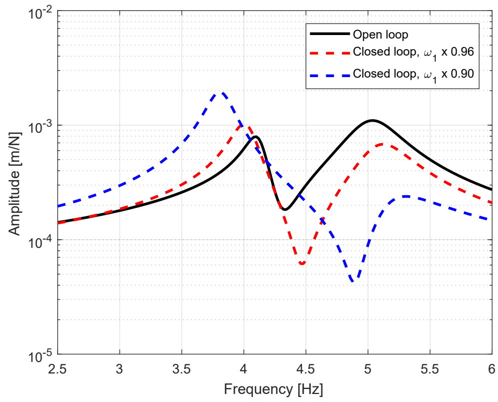

(b) Back laser output.

Figure 6.13: Synthesized FRFs experimentally obtained for the decrease of plunge frequency at 12.8 m/s by using experimental open-loop eigenvectors.

shows the gains used to get an increase about 10% of the pitch frequency.

Gains	**Leading-edge**	**Trailing-edge**
f_1 [deg/mm]	-0.0728	0.0364
f_2 [deg/mm]	0.0112	-0.0056
g_1 [deg/mm]	-1.8329	0.9165
g_2 [deg/mm]	0.2833	-0.1417

Table 6.5: Obtained gains to increase the pitch frequency about 10% at 12.8 m/s for the two control surfaces..

It is possible to see that trailing-edge's gains are the half with respect the leading-edge ones and also the sign is the opposite. This is due by the arbitrary coefficients which are respectively equal to 1 and -0.5. Also in this case the representation of poles placement in the complex plane shows the correct trend of the moved poles as shown in Figure 6.14. Finally the last FRFs of closed-loop and open-loop system are illustrated in Figures 6.15.

The Table 6.6 shows the pole placement obtained for the *test 1*, *test 2*, *test 3* and *test 4* and the flutter-speed obtained for each set of gains. It is seen that the experimental poles appear to be stable in the percentage errors and the maximum

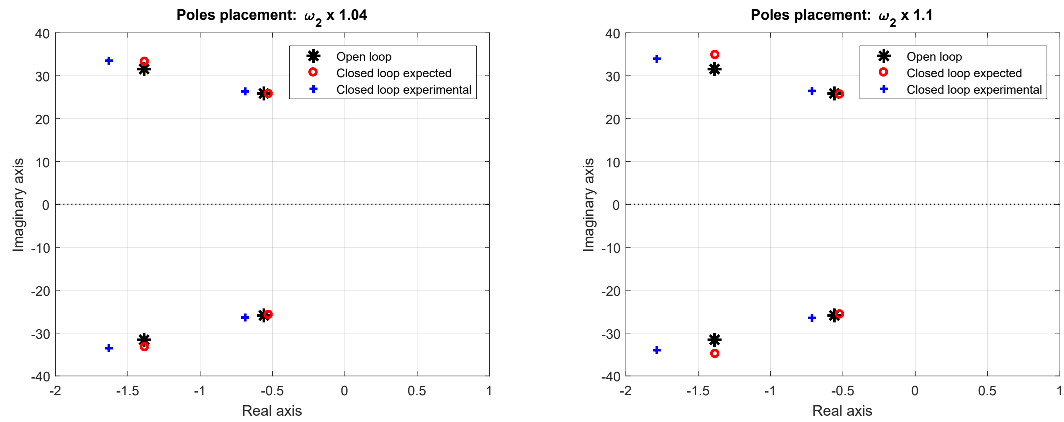

(a) Small increase of pitch frequency. (b) Large increase of pitch frequency.

Figure 6.14: Decrease of frequency at 12.8 m/s by using the experimental natural eigenvectors.

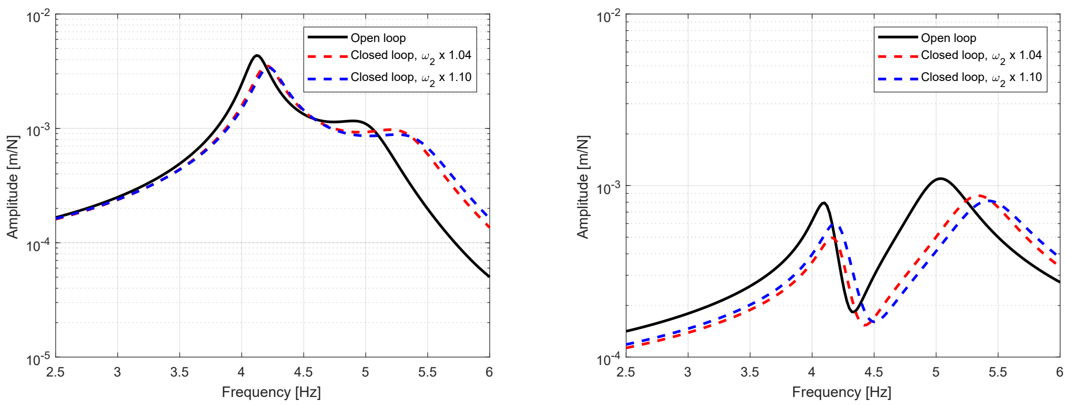

(a) Front laser output. (b) Back laser output.

Figure 6.15: Synthesized FRFs experimentally obtained for the increase of pitch frequency at 12.8 m/s by using experimental open-loop eigenvectors.

error registered is about 37% . It is necessary to consider that the maximum error comes from the lowest value of the pole, i.e. the real part of the first pole, therefore the correlated absolute difference is very tiny. In addition, the displacement of the pole is very large, therefore it is expected a large error. The flutter-speed increases when the frequencies are separated and it remains basically the same when the damping is increased. This fact is connected to definition of flutter: in fact, the flutter appears when the two peaks are very close therefore, by pushing away the

	1^{st} **mode** **Real**[1/s]	1^{st} **mode** **Imag.**[rad/s]	2^{st} **mode** **Real**[1/s]	2^{st} **mode** **Imag.**[rad/s]	**Flutter**[m/s]
$Open-loop$	-0.5591	±25.8804	-1.3871	±31.5667	15.6
$Test1\ \zeta_1 \times 3$	-1.6446(3.5%)	±26.7789(4.0%)	-1.1242(-19.5%)	±32.2390(1.6%)	15.7
$Test2\ \zeta_2 \times 3$	-0.6567(25.3%)	±26.4836(2.8%)	-3.2195(-22.4%)	±31.3217(1.1%)	15.9
$Test3\ \omega_1 \times 0.9$	-0.6726(26.6%)	±23.9264(3.2%)	-1.6320(12.9%)	±32.3521(2.2%)	>18
$Test4\ \omega_2 \times 1.1$	-0.7137(37.1%)	±26.4648(3.2%)	-1.7861(29.2%)	±33.9732(-2.5%)	16.5

Table 6.6: Pole placement of the four experimental tests at 12.8 m/s. For the sake of simplicity, just the poles with the larger displacements are reported and the percentage error between the absolute values of expected poles and experimental poles it is indicated in brackets. The last column indicates the flutter-speed for each case.

peaks, the flutter appears at larger wind-speed. Experimentally, it is seen that when the damping of a mode is increased the flutter appears with the mode of the non-modified pole, i.e. if the plunge damping is increased the flutter appears at about the same wind-speed in the pitch mode and viceversa. In conclusion it is possible to state that the use of the experimental open-loop eigenvectors in partial poles placement allows to have a good application of the receptance method and it allows to reduce the control efforts even if the $\alpha_{\mu_k,j}$ coefficients are not the optimized ones.

Total pole placement

It is possible to apply also the total poles placement. In this case there are no numerical errors because all the poles are moved. Just two different tests were performed, and other optimized arbitrary coefficients were used: $\alpha_{\mu_1,1}$=2.5, $\alpha_{\mu_1,2}$=0.5, $\alpha_{\mu_2,1}$=2.5 and $\alpha_{\mu_2,2}$=-1. In particular, were tested:

- *Test 5*: separation of frequencies with $\omega_1 \times 0.96$ $\omega_2 \times 1.04$;
- *Test 6*: increase of damping with $\zeta_1 \times 1.5$ $\zeta_2 \times 1.5$.

The control effort increases because both the poles are controlled at the same time, therefore is not possible to modify the poles as before. In fact, the real part of poles is multiplied for just a factor about 1.5 and the imaginary parts are moved for just the 4%. Also in this case the both the FRFs of closed- and open-loop are reported as shown in Figures 6.16 and 6.17 and pole placement is illustrated in complex plane in Figures 6.18.

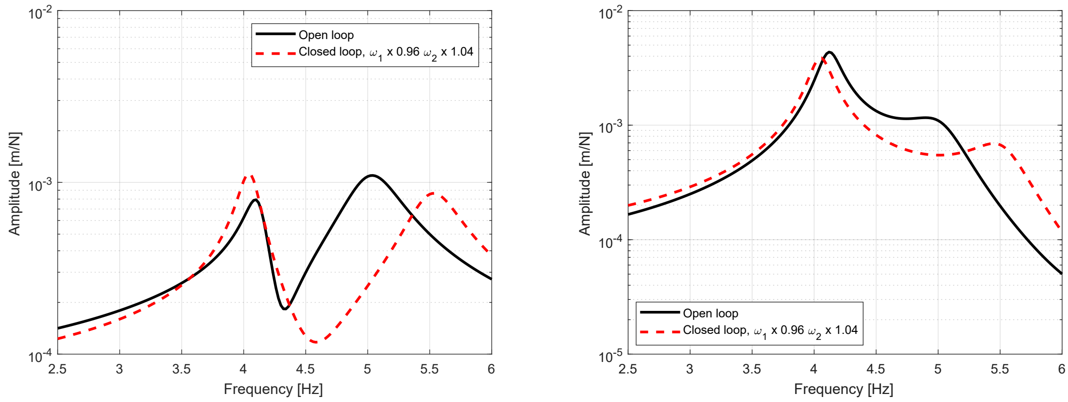

(a) Front laser output.

(b) Back laser output.

Figure 6.16: Separation of frequencies at 12.8 m/s, synthesized FRFs.

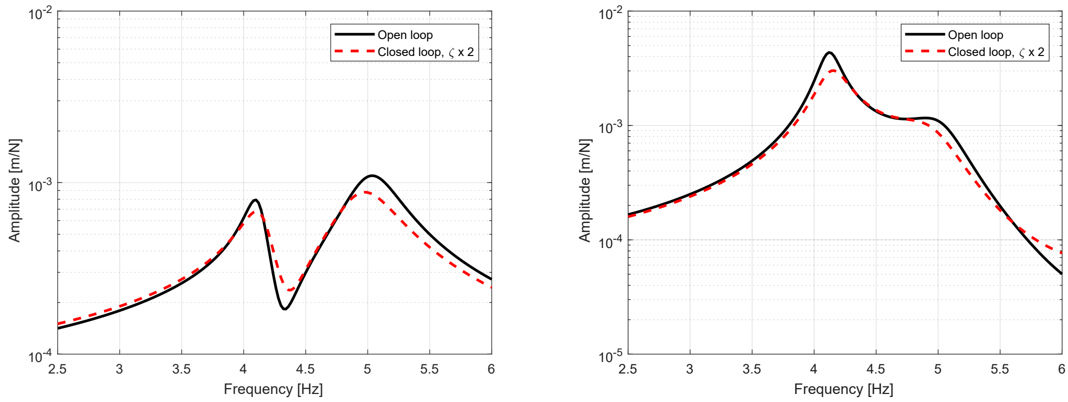

(a) Front laser output.

(b) Back laser output.

Figure 6.17: Increase of damping at 12.8 m/s, synthesized FRFs.

The FRFs show that the application of the receptance method works experimentally also in the total poles placement and the poles tend to be placed in the correct location.

The results of Table 6.7 show that the experimental pole placement is good also in this case even if the arbitrary coefficients are not the optimal one. The separation of frequencies allows to get a very high increase of flutter-speed even if the frequencies are moved for just the 4%. This fact denotes an high control effort when the frequencies are controlled: in fact, the real parts of the poles have a lower absolute value with respect the imaginary ones and this fact leads to get a larger

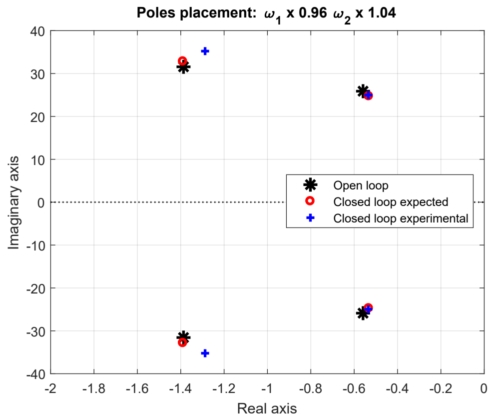

(a) Separation of frequencies.

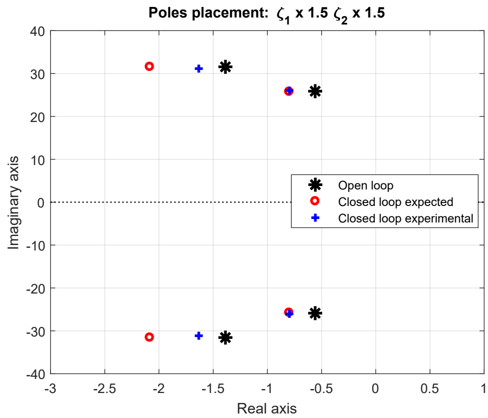

(b) Increase of damping.

Figure 6.18: Pole placement for different cases at 12.8 m/s.

	1^{st} **mode Real**[1/s]	1^{st} **mode Imag.**[rad/s]	2^{st} **mode Real**[1/s]	2^{st} **mode Imag.**[rad/s]	**Flutter[m/s]**
Open – loop	-0.5591	±25.8804	-1.3871	±31.5667	15.6
$Test5$	-0.5346(0.4%)	±24.9757(1.0%)	-1.2876(-7.34%)	±35.2236(7.9%)	>18
$Test6$	-0.7971(0.2%)	±26.0375(1.1%)	-1.633(-20.2%)	±31.1457(−1.3%)	15.7

Table 6.7: Pole placement of the first two experimental tests at 12.8 m/s to control both the poles. All the poles and the flutter-speed are reported in the columns and the percentage error between the absolute values of the expected poles and the experimental poles is indicated in brackets.

control effort when the frequency is controlled. As before, when the damping is increased the flutter appears at the same wind speed.

The gains used in *test 5* and *test 6* are now reported in Table 6.8.

Gains	**Test 5 Leading-edge**	**Test 5 Trailing-edge**	**Test 6 Leading-edge**	**Test 6 Trailing-edge**
f_1 [deg/mm]	-0.0187	0.0157	-0.0413	-0.0132
f_2 [deg/mm]	0.0057	-0.0181	0.0196	0.0477
g_1 [deg/mm]	0.6616	-0.2567	-1.2836	-0.9547
g_2 [deg/mm]	-0.2536	0.3746	0.6112	1.6189

Table 6.8: Obtained gains from *test 5* and *test 6* for the two control surfaces.

Chapter 7

Conclusion and Further works

The two DOFs model was designed, validated and experimentally controlled with the receptance method but there are many other possible applications of this system, both in the linear and non-linear field. From the linear point of view, it is possible to investigate other methods to control the structure or to better the application of the previously applied method. In particular the receptance method can place both the mode-shapes and the poles of the system but the minimum control effort is obtained when the closed-loop modeshapes are very similar to the open-loop one. In this particular condition, just the poles are placed without changing the modeshapes. It is possible to impose this condition by properly choosing the arbitrary coefficients $\alpha_{\mu_k,j}$. Mokrani et al. [14] have developed a theory to find the minimum control effort when the receptance method is applied. The theory provides for imposing the closed-loop modeshapes by using the least-square solution to find the arbitary coefficients and an experimental test could confirm this theory. Another interesting application is the gains scheduling which provides for applying the receptance method at different wind-speed on the same structure. In this way the gains are not constant anymore but they are changing on the base of the wind-speed. Through the application of the gains scheduling, it could be possible to control the system in very good way and it should be possible to impose experimentally the flutter-speed. An experimental verification could lead to good results in the flutter control. There are also many other application in non-linear field. In fact, it is possible to study the LCO when a non-linearity is applied on the linear model. In this two-DOFs model, the non-linear spring could be applied on the plunge direction and in this way should be possible to choose properly the characteristic of the spring. In general, the pole placement and the study of the non-linear structure could be actuated numerically and experimentally with the implementation of the feedback linearisation technique.

In conclusion, the main object of this thesis is tho development, the validation and the control of experimental a two-DOFs pitch and plunge model for the flutter prediction. Often, there are no clear links between the internal dynamic of the structure and the flutter onset, especially in the experimental case, therefore a simple model was necessary to experimentally replicate the flutter phenomenon. The physical model has demonstrated to be very well designed for investigation purposes: in fact by using the support structure, the flutter-speed has been experimentally set at the required wind-speed and the frequency response study led to find just two main modes as requested by the design constrains. The control surfaces demonstrated to be very efficient even if they are very small with respect the entire wing span, in fact by choosing properly the gains for the high authority control it was possible to increase the flutter-speed in closed-loop mode behind the speed limit of the wind tunnel of 18 - 20 m/s. The analytical model demonstrated that the unsteady loads assumption is appropriate to simulate the aeroelastic conditions of the two-DOFs wing model. In fact, it led to very good results in the flutter prediction and in the prediction of the poles trend. Finally, the application of the receptance method has shown very good results in the pole placement even some arbitrary coefficients were used. The experimental control gains found at 12.8 m/s with the receptance method were used to find the new flutter-speed in closed-loop mode. The frequencies separation led to increase the flutter-speed of the closed-loop system demonstrating that the correspondent gains can be used to make the wing more stable while the increase of damping did not change a lot the flutter-speed of the closed-loop system but just the flutter mode. The model has been validated, experimentally tested and used in different situations and application giving always good results.

Appendix A

Additional matrices

$$[A_a] = \begin{bmatrix} -\pi b^2 s_p & \pi b^3 s_p a \\ \pi b^3 s_p a & -b^4 s_p \pi (\frac{1}{8} + a^2) \end{bmatrix} \tag{A.1}$$

$$[B] = \begin{bmatrix} -\pi b s_p & -b^2 s_p \pi - \pi s_p b^2 (0.5 - a) \\ \pi s_p b^2 (0.5 + a) & -b^3 s_p \pi [(0.5 - a) - (0.5 - a)^2] \end{bmatrix} \tag{A.2}$$

$$[C] = \begin{bmatrix} 0 & -b s_p \pi \\ 0 & s_p \pi b^2 (0.5 + a) \end{bmatrix} \tag{A.3}$$

$$[N] = 2\pi \rho U s_p b \begin{bmatrix} -a_0 & -a_1 \\ a_0 b(0.5 + a) & a_1 b(0.5 + a) \end{bmatrix} \tag{A.4}$$

Bibliography

[1] D.H. Hodges and G.A. Pierce, *Introduction to Structural Dynamics and Aeroelasticity: Second Edition*, Cambridge University Press, 2011.

[2] J.R. Wright , J.E. Cooper, *Introduction to Aircraft Aeroelasticity and Loads*, John Wiley Sons, Ltd, 2007.

[3] G. Genta, *Vibration Dynamics and Control*, Springer, 2009.

[4] E.L. Houghton, P.W. Carpenter, *Aeroelasticity for Engineering Students*, Butterworth-Heinemann, fifth edition, 2003.

[5] T. Theodorsen, *General theory of aerodynamic instability and the mechanism of flutter*, National Advisory Committee for Aeronautics, report No. 496.,1935

[6] N. Bhoir and S.N. Singh, *Output feedback nonlinear control of an aeroelastic system with unsteady aerodynamics*, Aerospace science and technology, Vol.8, No. 3, 195-205, 2004.

[7] G. Platanitis and T.W. Strganac, *Control of a Nonlinear Wing Section Using Leading- and Trailing-Edge Surfaces*, Journal of Guidance, Control and Dynamic, Vol. 27, No.1, 52-58, 2004.

[8] S. Jiffri, S. Fichera, J.E. Mottershead and A. Da Ronch, *Experimental Nonlinear Control for Flutter Suppression in a Nonlinear Aeroelastic System*, Journal of Guidance, Control, and Dynamics, Vol. 40, No. 8, 1925-1938, 2017.

[9] I. Isnardi, P. Paoletti, D. Miranda, G. Innocenti, and S. Fichera,*Nonlinear Aeroservoelastic Control Design and Validation*, 2018 AIAA Guidance, Navigation, and Control Conference, AIAA SciTech Forum, Kissimmee, Florida 2018.

[10] Y.M. Ram and J.E. Mottershead,*Multiple-input active vibration control by partial pole placement using the method of receptances*, Mechanical Systems and Signal Processing, Vol.40, No. 2, 727-735, 2013.

[11] B. Mokrani, F. Palazzo, J.E. Mottershead and S. Fichera *Multiple Input Multiple Output experimental aeroelastic control using receptance-based method.* International Conference on Noise and Vibration Engineering, At Leuven, Belgium, 2018.

[12] Y.M. Ram, J.E. Mottershead *Receptance Method in Active Vibration Control*, AIAA journal, Vol.45, No. 3, 562-567, 2007.

[13] M.G. Tehrani, R.N.R. Elliott, J.E. Mottershead *Partial pole placement in structures by the method of receptances: Theory and experiments*, Journal of Sound and Vibration, Vol.329, No. 24, 5017-5035, 2010.

[14] B. Mokrani, A. Batou, S. Fichera, L. Adamson, D. Alaluf, J.E. Mottershead *The minimum norm multi-input multi-output receptance method for partial pole placement*, conference paper, 2019.

[15] I. Isnardi, *Nonlinear Dynamics and Control of an Aeroservoelastic System*, Polito webthesis, Politecnico di Torino, 2018.

[16] F. Palazzo, *Multiple-input active aeroelastic control using the receptance method on a flexible wing*, Polito webthesis, Politecnico di Torino, 2018.